OULU 2020
C 755

ACTA UNIVERSITATIS OULUENSIS

Satish Kolli

SENSITIZATION IN AUSTENITIC STAINLESS STEELS

QUANTITATIVE PREDICTION CONSIDERING MULTICOMPONENT THERMODYNAMIC AND MASS BALANCE EFFECTS

UNIVERSITY OF OULU GRADUATE SCHOOL;
UNIVERSITY OF OULU,
FACULTY OF TECHNOLOGY

ACTA UNIVERSITATIS OULUENSIS
C Technica 755

SATISH KOLLI

SENSITIZATION IN AUSTENITIC STAINLESS STEELS

Quantitative prediction considering multicomponent thermodynamic and mass balance effects

Academic dissertation to be presented with the assent of the Doctoral Training Committee of Technology and Natural Sciences of the University of Oulu for public defence in the OP auditorium (L10), Linnanmaa, on 28 July 2020, at 12 noon

UNIVERSITY OF OULU, OULU 2020

Copyright © 2020
Acta Univ. Oul. C 755, 2020

Supervised by
Professor David Porter

Reviewed by
Professor Paulo J. Ferreira
Doctor Paul Rosemann

Opponents
Professor Minnamari Vippola
Professor Paulo J. Ferreira

ISBN 978-952-62-2660-6 (Paperback)
ISBN 978-952-62-2661-3 (PDF)

ISSN 0355-3213 (Printed)
ISSN 1796-2226 (Online)

Cover Design
Raimo Ahonen

PUNAMUSTA
TAMPERE 2020

Kolli, Satish, Sensitization in austenitic stainless steels. Quantitative prediction considering multicomponent thermodynamic and mass balance effects

University of Oulu Graduate School; University of Oulu, Faculty of Technology
Acta Univ. Oul. C 755, 2020
University of Oulu, P.O. Box 8000, FI-90014 University of Oulu, Finland

Abstract

Austenitic stainless steels have wide range of different applications, but their corrosion resistance is compromised due to sensitization phenomenon. If these steels are subjected to heat treatments in the temperature regimes of 500–900 °C, chromium carbides are formed along the grain boundaries leading to chromium depletion in the vicinity of these carbides. This is called sensitization and makes the microstructure sensitive to intergranular corrosion. The sensitization behavior is greatly influenced by several metallurgical factors such as aging temperature, time, grain size and chemical composition. In order to study the effect of above-mentioned individual factors, a modeling prediction is needed, because of the cost and limitations involved with the lab experiments.

The CALPHAD modeling capability has evolved and is utilized in this thesis in estimating the sensitization by predicting the chromium concentration profiles across the grain boundary $M_{23}C_6$ carbide – austenite matrix interface by considering multicomponent effects. Thermo-Calc has been utilized in estimating the equilibrium calculations, TC-Prisma for the nucleation kinetics and DICTRA for solving the moving phase boundary problem. These are validated with diverse experimentally measured sensitization databases. Commercial stainless steel heats EN 1.4310, 1.4301, 1.4303, 1.4307 and 1.4318 have been subjected to heat treatments at various temperatures to induce varying levels of sensitization and the degree of sensitization was measured using the double loop electrochemical potentiokinetic reactivation test (DL-EPR) to develop the necessary quantitative database. Based on the chromium depletion profiles calculated and the experimentally determined DOS, a depletion parameter has been established that can quantitatively predict the sensitization and self-healing phenomenon in austenitic stainless steels. Models are proposed based on depletion parameter that accounts for the effects of thermal aging, grain size and chemical compositions.

Keywords: CALPHAD, chemical composition, diffusion, grain size, precipitation, self-healing, sensitization, stainless steels

Kolli, Satish, Herkistyminen austeniittisissa ruostumattomissa teräksissä. Kvantitatiivinen mallintaminen ottaen huomioon monikomponenttiset, termodynaamiset ja massataseen vaikutukset.

Oulun yliopiston tutkijakoulu; Oulun yliopisto, Teknillinen tiedekunta
Acta Univ. Oul. C 755, 2020
Oulun yliopisto, PL 8000, 90014 Oulun yliopisto

Tiivistelmä

Austeniittiset ruostumattomat teräkset soveltuvat monenlaisiin käyttökohteisiin, mutta niiden korroosionkestävyyttä on kompromisoitu herkistymisilmiön seurauksena. Mikäli näitä teräksiä kuumennetaan 500–900 °C lämpötiloissa, kromikarbideja alkaa muodostua raerajoille, mikä johtaa kromista köyhtymiseen karbidien läheisyydessä. Tätä kutsutaan herkistymiseksi, ja se altistaa mikrorakenteen raerajakorroosiolle. Herkistymiseen vaikuttavat olennaisesti mm. lämpötila, raekoko ja kemiallinen koostumus. Jotta näiden tekijöiden yksilöllisiä vaikutuksia voidaan tutkia, tarvitaan siihen tehokkaita mallinnusmenetelmiä.

Tämä väitöskirja hyödyntää CALPHAD mallinnusta herkistymisen arvioimisessa ennustamalla kromin konsentraatioprofiileja raerajalla olevan $M_{23}C_6$-karbidin ja austeniittimatriisin rajapinnan ylitse huomioiden multikomponenttiefektit. Thermo-Calc -ohjelmistoa käytetään tasapaino-olosuhteiden arvioimiseen, TC-Prismaa ydintymiskinetiikkaan ja DICTRA:a liikkuvan faasirajapinnan haasteen ratkaisemiseksi. Nämä tulokset validoidaan erilaisia kokeellisia tietokantoja hyödyntäen. Tutkimuksessa lämpökäsiteltiin kaupallisia austeniittisia ruostumattomia teräksiä EN 1.4310, 1.4301, 1.4303, 1.4307 ja 1.4318 eri herkistymisasteiden saavuttamiseksi, ja niiden herkistyminen mitattiin elektrokemiallisella potentiokineettisella uudelleenaktivointitestillä (DL-EPR) vaadittavan kvantitatiivisen tietokannan luomiseksi. Kromipitoisuusprofiilien perusteella laskettujen ja kokeellisesti määritettyjen herkistymisasteiden perusteella luotiin köyhtymisparametrit, jotka mahdollistavat herkistymisen ja toipumisen kvantitatiivisen ennustamisen austeniittisille ruostumattomille teräksille. Näihin köyhtymisparametreihin pohjautuvien mallien avulla voidaan arvioida lämpövanhenemisen, raekoon ja kemiallisen koostumuksen vaikutuksia.

Asiasanat: CALPHAD, diffuusio, erkautuminen, herkistyminen, kemiallinen koostumus, raekoko, ruostumaton teräs, toipuminen

To my beloved parents, Bala Sundara Rao and Padmavathi with deepest love.

Acknowledgements

The research for this thesis was done at the Materials and Mechanical Engineering unit at University of Oulu and Tornio Research Centre, Outokumpu. This Ph.D. project is one of the eight workpackages in the MIMESIS project that was funded by European Commission under grant number 675715 - MIMESIS - H2020 - MSCA - ITN - 2015, which is a part of Marie Sklodowska-Curie Innovative Training Networks European Industrial Doctoral programme. I would like to thank Tauno Tönningin Säätiö for awarding the personal grant. Although the dissertation has only one author, it is a result of co-operation with a number of people around me. Herewith, I would like to express my sincere gratitude to the following people for their valuable help and advice during this work from 2016 to 2020.

I will forever be thankful to my principal supervisor Professor David Porter, for offering me the opportunity to work on a Ph.D. in the Materials and Mechanical Engineering, within Center for Advanced Steels Research. He is and remains one of my best role model for a scientist, mentor and teacher. I am greatly indebted to him for his continuing confidence in me, for giving me constant support throughout these years and for teaching me how to navigate the research world.

I also thank my industrial supervisor Dr. Thomas Ohligschläger, for his continuous support and valuable guidance during my industrial secondment at Tornio Research Centre, Outokumpu. I am grateful to senior engineer Mr. Suresh Kodukula, Mr. Timo Manninen and Dr. Severi Anttila from the same company for making my stay in Tornio so enjoyable.

I also wish to thank Professor Dietmar Hoemberg, Dr. Thomas Petzold and Dr. Robert Lasarzik, for the wealth of knowledge that they shared during my secondment at Weierstrass Institute for Applied Analysis and Stochastics (WIAS), Berlin, Germany. Our discussions helped me to better understand the modelling part of my project as well as the application of mathematics in engineering projects.

I would also like to thank senior engineer Bjørnar Grande, senior engineer John Inge Asperheim and Dr. Dmitry Ivanov for all their help and arrangements during my industrial secondment in EFD Induction, Skien, Norway as well as for being open to discuss my questions.

Special thanks to Professor Jukka Kömi, to dear Seppo Järvenpää and to Dr. Mahesh Somani for the endless help and support they gave from the very beginning to the end of this project. Respective thanks to Mr. Juha Uusitalo, Mr. Tun Tun Nyo and Mr. Ilpo Alasaarela for their practical help in the laboratory work. Furthermore, I thank my colleagues at Materials and Mechanical Engineering research unit, Dr.

Vahid Javaheri, Dr. Antti Kaijalainen, Dr. Aarne Pohjonen, Dr. Sakari Pallaspuro, Mr. Mohammed Ali Saleh Fahim, Mr. Oskari Haiko, Mr. Sami Koskenniska, Mr. Sampo Uusikallio, Mr. Henri Tervo: thank you for all your help, fruitful collaborations, all the constructive discussions and also for creating friendly and productive atmosphere at work.

My thanks to pre-examiners of this dissertation, Professor Paulo Ferreira from The University of Texas at Austin and Dr. Paul Rosemann from Otto-von-Guericke Universität Magdeburg for their valuable comments and recommendations.

Getting through my Ph.D. trajectory would not have been possible without the support and the encouragement of my dearest friends. I would like to thank my beloved friends Naveen Yalla, Dr. Viswanadh Gowtham and Dr. Revathi for providing me all the moral and emotional support in my life. I would like to thank my brother Eshwar, Vahid, Suresh, Ganapathi Ram, Prem and all the students of MIMESIS for all the love and affection. Special thanks to my buddies of Finditaly, Avishek, Siva, Praneeth, Snehal, Megha, Priyanka, Virginia for making Oulu, my second home with all the love and encouragement.

Finally I thank my dearest Amma and Nanna (Mon and Dad), Padmavathi and Balasundara Rao for their unconditional love and support. I do not have enough words to describe what you mean to me. I would also like to thank my sister Laxmi Prasanna and brother-in-law Sandeep for their love and support.

Oulu, Finland, May 2020 Satish Kolli

Abbreviations and symbols

AOD	argon oxygen decarburization
BWR	boiling water reactor
CALPHAD	calculation of phase diagrams
CCS	continuous cooling sensitization
CEF	compound energy formalism
CNT	classical nucletion theory
DL-EPR	double loop electrochemical potentiokinetic reactivation test
DOS	degree of sensitization
DP	depletion parameter
EBSD	electron back scattered diffraction
EDS	energy dispersive x-ray spectroscopy
EPR	electrochemical potentiokinetic reactivation test
ESR	electroslag remelting
FESEM	filed emission scanning electron microscopy
FIB	focused ion beam
GDOES	glow discharge optical emission spectroscopy
i.e.	id est
IGC	intergranular corrosion
IGSCC	intergranular stress corrosion cracking
NDOS	normalised degree of sensitization
$NDOS_{measured}$	experimentally measured normalized degree of sensitization
$NDOS_{predicted}$	predicted normalized degree of sensitization
PT	peak temperature (°C)
PWR	pressurised water reactor
SAD	selected area diffraction
SCC	stress corrosion cracking
SCE	saturated calomel electrode
SGTE	scientific group thermodata europe
SL-EPR	single loop electrochemical potentiokinetic reactivation test
ST	solution treated
STEM	scanning transmission electron microscopy
TEM	transmission electron microscopy
TTS	time - temperature - sensitization
VOD	vaccum oxygen decarburization

a	lattice parameter
a_c	activity of carbon in the austenite matrix
a_i's	coefficients that express temperature dependence of the end members
b_i	stochiometric coefficient
c_k^{β}	concentration of element k in carbide at the carbide - austenite interface
c_k^{γ}	concentration of element k in austenite at the carbide - austenite interface
$c_{Cr}^{\gamma\beta}$	chromium concentration in austenite in equilibrium with the carbide
$\overline{c}_{Cr}^{\gamma}$	far-field concentration of chromium
$c_{Cr\ min}^{\gamma\beta}$	minimum chromium concentration at the γ/β interphase
Cr_{int}	interfacial chromium concentration in austenite
Cr_{crit}	critical chromium concentration
$\mathrm{Cr}^{\mathrm{eff}}$	effective chromium content
d_a	width of austenite from which carbon can be withdrawn
d_p	half-thickness of $M_{23}C_6$ carbide film
D_i	diffusion coefficient of element i in the matrix
D^{γ}	bulk diffusivity
E_{corr}	corrosion potential
E_{pp}	primary passivation potential
E_p	passivation potential
G_m	gibbs energy of phase m
G_m^{srf}	gibbs energy of an unreacted mixture of constituents of phase m ans srf stands for surface of reference
G_m^{phy}	physical models' contribution to the Gibbs energy
G_m^{E}	excess gibbs energy
G_i^{0}	gibbs energy of pure element i
$G_m^{E,bin}$	binary excess energy term
$G_m^{E,ter}$	ternary excess energy term
$G_m^{E,hig}$	higher order excess energy term
ΔG^{*}	gibbs energy of formation of the critical nucleus
$\Delta G_m^{\alpha\rightarrow\beta}$	chemical driving force for the nucleation
H_i^{SER}	enthalpy of the element i in the reference state
i_p	passivation current
i_{cp}	peak anodic current

I_a	activation peak current
I_r	reactivation peak current
J_k^{β}	flux of component k in the carbide at the carbide - austenite interface
J_k^{γ}	flux of component k in the austenite at the carbide - austenite interface
$J(t)$	time dependent nucleation rate
k	number of components
K_{eq}	equilibrium constant
L_{ij}	binary interaction parameter
L_{ijk}	ternary interaction parameter
N_A	Avogadro number
Pi	pi phase
r^*	critical radius of the nucleus
S_m^{cnf}	configurational entropy of phase m
t_s	time taken for the start of sensitization development
t_d	time after which desensitization begins
T	temperature
$v^{\beta/\gamma}$	interfacial velocity
V_m^{β}	molar volume of the β precipitate phase
W_{crit}	width of chromium concentration profile at critical chromium
wt.%	weight in percent
X_{Cr}^{i}	chromium concentration in the austenite at the carbide - austenite interface
X_{Cr}^{crit}	critical chromium concentration
x_i	molefraction of the constituent i
x_j	molefraction of the constituent j
x_k	molefraction of the constituent k
$X_i^{\beta/\alpha}$	molefraction of element i at the interface in the precipitate
$X_i^{\alpha/\beta}$	molefraction of element i at the interface in the matrix
z	position of the interphase
Z	zeldovich factor
β^*	rate at which atoms or molecules are attached to the critical nucleus
γ_{Cr}	activity coefficient of chromium
σ	sigma phase
τ	nucleation time for precipitation

$\Phi_r^{i,j}$	interaction parameter between elements *i* and *j*

List of original publications

This thesis is based on the following publications, which are referred to throughout the text by their Roman numerals:

I Kolli, S., Ohligschläger, T., & Porter, D. (2017). Continuous cooling sensitization and its evaluation in austenitic stainless steels EN 1.4310. In *Proceedings of 9th European Stainless Steel Conference - Science & Market and the 5th European Duplex Stainless Steel Conference & Exhibition.* Bergamo, Italy: Associazione Italiana di Metallurgia.

II Kolli, S., Ohligschläger, T., & Porter, D. (2019). Quantitative prediction of sensitization in austenitic stainless steel accounting for multicomponent thermodynamic and mass balance effects. *ISIJ International,* 59*(*7), 1330-1336.

III Kolli, S., Ohligschläger, T., Kömi, J., & Porter, D. (2019). Sensitization and self-healing in austenitic stainless steel: Quantitative prediction considering carbide nucleation and growth. *ISIJ International, 59(11),* 2090-2097.

IV Kolli, S., Javaheri, V., Kömi, J., & Porter, D. (2019). On the role of grain size and carbon content on the sensitization and desensitization behavior of 301 austenitic stainless steel. *Metals, 9*(11), 1193.

V Kolli, S., Javaheri, V., Ohligschläger, T., Kömi, J., & Porter, D. (2020). The importance of steel chemistry and thermal history on the sensitization behavior in austenitic stainless steels: Experimental and modeling assessment. *Materials Today Communications*, *24*, 101088.

The author has been the main and corresponding author in all the listed publications. He prepared the research plan, conducted the literature survey performed the experiments and also performed the numerical simulations. He also analyzed the data and interpreted the results together with Professor David Porter for all the articles. The role of other co-authors beside the reviewing and commenting on the above manuscripts was as follows.

Dr. Thomas Ohligschläger provided the feedback with regards to corrosion testing and analysis for the Papers I–III and Paper V, Dr. Vahid Javaheri provided the necessary help with EBSD measurements and the use of MTEX toolbox for Matlab in post-processing the EBSD data in Paper IV and feedback in writing the Paper V, Professor Jukka Kömi provided the necessary funding for conducting the experiments and simulation work for Papers IV–V.

Briefly about the publications: Paper I is an attempt to use DICTRA to predict sensitization during non-isothermal heat treatments in 1.4310 austenitic stainless steels. The paper provides a continuous cooling sensitization diagram based on the average chromium content in the first 25 nm of the chromium depletion across the $M_{23}C_6$ carbide - austenite matrix interface.

Paper II successfully employs a one-dimensional model for simulating the grain boundary carbide growth and predicting the early stages of sensitization in 1.4310 austenitic stainless steel for isothermal heat treatments. A depletion parameter was established from correlations between experimentally measured sensitization values and chromium depletion calculated using DICTRA.

Paper III extends the one-dimensional model proposed in Paper II to predict the sensitization and self-healing behavior in 1.4310 austenitic stainless steels for isothermal heat treatments. The depletion parameter was modified and used in sensitization estimations.

Paper IV successfully employs the 1-D model in Paper III for estimating the sensitization and self-healing in 1.4310 alloy with various grain sizes for isothermal heat treatments. The role of grain size and carbon content on the development of sensitization was addressed.

Paper V proposed a comprehensive 1-D model for sensitization and self-healing estimations based on alloy composition, thermal history and grain size in austenitic stainless steels. The model allows the study of the effects of individual elements on sensitization, and the importance of steel chemistry was discussed in the paper.

Contents

Abstract
Tiivistelmä
Acknowledgements **9**
Abbreviations and symbols **11**
List of original publications **15**
Contents **17**
1 Introduction **19**
1.1 Background ... 19
1.2 Aims of the research ... 20
2 Theoretical foundation **23**
2.1 Types of stainless steels ... 23
2.2 Corrosion mechanisms in stainless steels ... 27
2.3 Sensitization and mechanisms of sensitization ... 30
2.4 Factors affecting sensitization ... 33
2.4.1 Alloy composition ... 33
2.4.2 Influence of grain size ... 34
2.5 Experimental determination of degree of sensitization ... 35
2.6 Modeling ... 37
2.7 CALPHAD technique ... 43
3 Experiments and Modeling **47**
3.1 Materials ... 47
3.2 Experimental methods ... 47
3.3 Modeling methods ... 51
3.3.1 Thermo-Calc ... 51
3.3.2 DICTRA ... 52
3.3.3 TC - Prisma ... 55
4 Results **57**
4.1 Degree of sensitization ... 57
4.2 Precipitation and chromium depletion ... 63
4.3 Nucleation kinetics ... 69
4.4 Grain boundary precipitate growth and Cr depletion ... 72
5 Discussion **79**
5.1 Relationship between Cr depletion profile and degree of sensitization ... 79
5.2 The separate effects of grain size and composition ... 88

5.3 Importance of multicomponent effects 92
5.4 Importance of interfacial energies 94
6 Summary and conclusions **97**
7 Novel features **99**
8 Recommendations for further research **101**
List of references **103**
Original publications **111**

1 Introduction

1.1 Background

Stainless steels are an important class of metallic alloys. Owing to their omnipresence in our daily lives, it is difficult to list the applications of stainless steels. Their use ranges from low-end cooking utensils to hi-tech space vehicles [1]. The use of the term ‘stainless’ implies no staining or corroding in the conditions that cause normal steels to corrode.

It was first discovered by Riley in 1889 that the addition of nickel to mild steel significantly enhanced its tensile strength. Later in 1905, Portvin found that steel with a chromium content of more than 9 wt.% was resistant to chemical attack. During the period 1910–1915, stainless steel was made for practical applications [2]. Stainless steel with the composition 12.8 wt.% chromium and 0.24 wt.% carbon was first melted in August 1913 in Sheffield, England according to a proposal by Harry Brearley. It was used in the manufacturing of barrels for heavy artillery. Later, first austenitic stainless grades were developed by Strauss and Meurer from Germany [3]. Dannitzen in the USA developed ferritic stainless steel grades by tweaking Brearley’s composition towards lower carbon contents. At the same time, Becket from the USA developed heat resistant steel by increasing chromium to at least 18 wt.% giving oxidation resistance at higher temperatures. In spite of these early discoveries, the Fe/Cr and Fe/Cr/Ni systems were only understood by around 1940 and stainless steels were standardized in 1950. New steelmaking techniques were widely adopted in the 1970’s thereby expanding the ranges of stainless steel compositions that could be commercially produced. The steelmaking technologies like vacuum oxygen decarburization (VOD) and Argon-oxygen decarburization (AOD) helped to achieve better composition control and and lower carbon contents. Homogeneous microstructures containing fewer inclusions were realized with electroslag remelting (ESR). The steel grade 904L (N08904) was the first alloy that took the advantages of the new technologies and was developed by the company that is now Outokumpu stainless steel.

The mechanical, fabrication and corrosion resistance properties of stainless steels make them suitable for construction applications. However, when exposed to temperatures in the range 450–850 °C, stainless steels are prone to what is known as sensitization, which is associated with the precipitation of chromium rich carbides along grain boundaries and the concomitant depletion of chromium in the

regions adjacent to the grain boundaries [4]. When the steel is sensitized, it becomes susceptible to intergranular corrosion (IGC) and intergranular stress corrosion cracking (IGSCC) resulting in premature failure of fabricated components. Stainless steel sensitization is one of the most studied cases of environmental degradation of engineering materials [5].

The sensitization phenomenon in austenitic stainless steels has been widely studied and a large database of sensitization in different alloys is available in the literature. There were also several works dedicated to developing models for the quantitative determination of sensitization and they will be discussed in detail in later sections. However, some of the models proposed did not consider the multicomponent effects during the nucleation and growth of $M_{23}C_6$ carbides and some did not correlate the modeling observations to that of experiments to quantitatively evaluate the sensitization. This work thus aims to fill these gaps, firstly to predict the precipitation of $M_{23}C_6$ considering multicomponent effects using CALPHAD (CALculation of PHAse Diagrams) modeling, and then establishing parameters that could represent sensitization and self-healing based on grain size, composition and thermal history. These parameters are established by correlating the sensitization predicted by models with experimentally determined sensitization values. The thesis attempts to predict not only $M_{23}C_6$ carbide precipitation but also the resultant degree of sensitization (DOS). The dissertation thus advances scientific knowledge related to sensitization behavior by better enabling the quantitative predictions of not only precipitation but also the DOS. The work will help in estimating the life of austenitic stainless steels with respect to intergranular corrosion and also in designing alloys for a specific temperature application in terms of minimizing the risk of intergranular corrosion.

1.2 Aims of the research

The influence of grain size, chemical composition, temperature and time on sensitization are understood qualitatively. Also, some quantitative modelling has been done as exemplified by the models available in the literature. The aim of the current work is to develop a tool or method to quantitatively predict the presence or absence of sensitization and the ranges of sensitization in austenitic stainless steels that are isothermally or non-isothermally heat treated. This thesis thus forms the basis for the prediction of potential corrosion problems. The objectives of the current research are as follows:

- Experimental determination of sensitization and desensitization in the austenitic stainless steels that vary in grain size and composition and subjected to different heat treatments.
- To predict the chromium depleted regions around the grain boundary $M_{23}C_6$ carbide - austenite matrix numerically by taking into consideration, the multicomponent thermodynamic and mass-balance effects.
- To develop a model that could quantitatively determine the degree of sensitization in austenitic stainless steels in combination with experimental data accounting for grain size, chemical composition and thermal history
- Quantitative prediction of isothermal sensitization and self-healing to identify the temperatures and heat treatment times required to avoid potential sensitization regimes and to identify the routes to achieve self-healing.
- To investigate and predict the importance and influence of steel chemistry and grain size on the sensitization behavior of austenitic stainless steels, and thereby provide a tool to estimate potential corrosion problems and aid the design of alloy compositions suitable for specific applications.

2 Theoretical foundation

2.1 Types of stainless steels

The three main microstructural constituents found in stainless steels are ferrite, austenite and martensite. They are found in the various classes of stainless steel, i.e. (a) ferritic stainless steels, (b) austenitic stainless steels, (c) martensitic stainless steels, (d) duplex stainless steels, and (e) precipitation hardening stainless steels. The ferritic grades contain around 11–30% chromium by wt., less than 0.1% carbon, trace amounts of nickel and alloying elements like molybdenum, titanium or aluminium. These steels possess better deep drawability, resistance to stress corrosion cracking (SCC), poor resistance to localised corrosion. They are magnetic, not heat treatable and can be strengthened by cold working [6]. The austenitic stainless steels are the most corrosion resistant of the stainless group due to high chromium and nickel contents. These are either single phase austenite or duplex austenite and delta ferrite phase structures. These steels are non-magnetic, and can be hardened by cold rolling [4]. The different types of austenitic stainless steels can be seen from Table 1 and Fig. 1. Type EN 1.4301, which is also recognised as 18-8 or grade 304, has very good corrosion resistance in atmospheric conditions. The pitting and crevice corrosion resistance can be improved with the addition of 2–3% molybdenum to get type 1.4401 (grade 316) and are utilized in similar applications to type 1.4301 in more aggressive environments. Relatively expensive nickel can be partly replaced with cheaper manganese or nitrogen to produce lower-cost and lower-performance chromium - manganese - low nickel grades such as 1.4372 (grade 201). The 200 and 300 series of austenitic stainless steel are weldable. These steels are, however, prone to sensitization on exposure to high temperatures during welding. For such applications, low carbon types (<0.03%) like 1.4307 (304L), 1.4404 (316L), 1.4541 (321), 1.4550 (347) can be used [7].

Table 1. Classification and composition of austenitic stainless steels (Reprinted by permission from [7] © 2016 Elsevier).

EN	BS	AISI	EN	DIN	SS	Typical composition (%)				
						C	Cr	Ni	Mo	Other
1.4301	304S31	304	58E	X5CrNi 18-10	2333	0.07	18	8		
1.4303	305S19	305		X5CrNi 18-12		0.06	18	11		
1.4305	303S31	303	58M	X10CrN iS18-9	2346	0.10	18	8		0.35 × S
1.4306		304 L		X2CrNi 19-11	2352	0.03	18	10		
1.4307	304S11	304 L			2352	0.03	18	8		
1.4310	301S21	301		X12CrN i17-7	2331	0.05 – 0.15	17	6		
1 4311	304S61	304LN		X2CrNi N18-10	2371	0.03	18	9		0.22 × N
1.4372		201				0.15	17	4.5		6.5 × Mn
1.4401	316S31	316	58J	X5CrNi Mo17-12-2	2347	0.07	17	11	2	
1.4404	316S11	316 L		X2CrNi Mo17-13-2	2348	0.03	17	11	2	
1.4406	316S61	316 LN		X2CrNi MoN17-12-2		0.03	17	11	2	0.22 × N
1.4432	316S13	316 L			2353	0.03	17	11	2.5	
1.4435	316S13	316 L		XCrNiM o18-14-3	2353	0.03	17	13	2.5	
1.4436	316S33	316	58J	X5CrNi Mo17-13-3	2343	0.05	17	11	2.5	
1.4438	317S12	317 L			2367	0.03	18	13	3	
1.4439				X2CrNi MoN17-13-5		0.03	17	13	4	0.22 × N
1.4541	321S31	321	58B	X6CrNi Ti18-10	2337	0.08	18	9		0.5 Ti

EN	BS	AISI	EN	DIN	SS	Typical composition (%)				
						C	Cr	Ni	Mo	Other
1.4550	347S31	347	58F	X6CrNiNb18-10	2338	0.08	18	9		0.5 Nb
1.4567	394S17	304Cu				0.04	18	9		4 × Cu
1.4571	320S31	(316Ti)		X6CrNoMoTi17-12-2	2350	0.08	17	11	2	0.5 × Ti
1.4539	904S13			X1CrNiMoCuN25-20-5	2562	0.02	19	24	4	2 × Cu
1.4547					2378	0.02	20	18	6	1 × Cu
1.4529				X1CrNiMoCuN25-20-6		0.02	19	24	6	1.5 × Cu

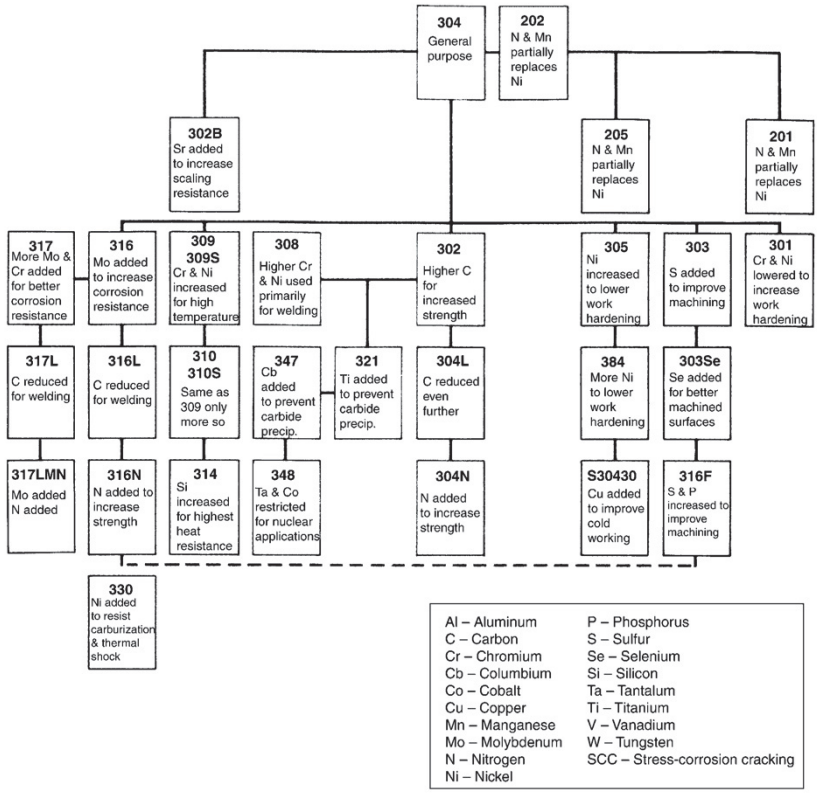

Fig. 1. The austenitic stainless family (Reprinted by permission from [8] © 2011 Nickel Institute / AISI).

Martensitic stainless steels contain chromium in the range 12–18 wt.% but have higher carbon content up to 1% by wt. They can be hardened and tempered like carbon and low-alloy steels [9]. These are magnetic and have lower weldability and formability. Duplex stainless steels contain austenite and ferrite in equal proportions, which is achieved by adjusting the amounts of chromium (18–26 wt.%), nickel (5–6 wt.%), molybdenum (1.5–4 wt.%) and nitrogen. They are characterised by excellent toughness and corrosion resistance compared to ferritic stainless steels. They are magnetic, weldable and moderately formable. “Lean duplex” steels have comparable corrosion resistance to austenitic grades while “Super duplex” steels have enhanced resistance to all forms of corrosion when compared to standard austenitic stainless steels. Precipitation hardened steels can

develop very high strengths when suitably aged due to the formation of fine precipitates in the matrix of the steel. These steels offer a good combination of corrosion resistance, acceptance of heat treatment, strength and fabricability [10].

2.2 Corrosion mechanisms in stainless steels

In general, stainless steels are corrosion resistant in most environments due to the presence of a thin surface layer of chromium oxide that self-repairs naturally when breached. However, corrosion can occur if the damage is too extensive. When that occurs depends on the grade of steel, as each of them have a different response in different corrosive environments. The most common types of corrosion are pitting, crevice, uniform and galvanic corrosion. The less common types of corrosion include SCC and intergranular attack [4].

Pitting corrosion is a localised form of attack that occur in environments containing chlorides or sulphides. The speed of metal dissolution does not allow the re-passivation of the local break in the passive layer caused by the chloride or sulphide containing environments [11]. The presence of oxygen is responsible for the formation of the passive layer on the surface of stainless steel. In crevices, oxygen access to the steel surface is hindered thereby making crevices vulnerable to crevice corrosion. In uniform corrosion, the passive layer is attacked uniformly and metal loss is distributed over the entire surface of the steel leading to uniform or general corrosion. When two dissimilar metals are in contact with each other in an electrolyte, a galvanic cell is set up that accelerates the corrosion of the less noble metal causing galvanic corrosion. The simultaneous presence of tensile stresses and environmental factors lead to the development of SCC. In SCC, the cracks are formed after a long incubation time period. However, they propagate relatively rapidly, either along grain boundaries or through the matrix, resulting in failure. In the temperature region 450–900 °C, when the carbon content of the steel is high, it combines with chromium to form chromium carbides along the grain boundaries. This causes the formation of chromium depleted regions along the grain boundaries, which is referred as “sensitization” and makes the steel susceptible to IGC. The stress corrosion cracking that occurs due to intergranular attack is termed as intergranular stress corrosion cracking (IGSCC) [4].

The corrosion behaviour of any alloy depends on many factors other than material microstructural condition and can be seen in Fig. 2. One of the important factors that controls corrosion performance is the severity of the environment. Materials resistance to corrosion attack also depends on its stress state. In some

aqueous conditions, the chromium-depleted grain boundary can facilitate IGC or SCC [12]. The susceptibility of a sensitized microstructure to intergranular corrosion can be measured in terms of the degree of sensitization (DOS).

Good corrosion resistance, weldability, formability of austenitic stainless steels makes them one of the important construction materials in nuclear power plants. Stainless steels are used for piping, reactor-vessel cladding, for structures inside the pressure vessel including the core shroud in boiling water reactors (BWR). Similar kinds of material are chosen for the pressurized water reactors (PWR). In the design codes of boiling water reactors and pressurized water reactors (BWRs and PWRs), SCC is considered. IGSCC is by far the largest damage mechanism in oxidising BWR [13], [14]. The cracking in BWRs was observed more than 50 years ago [15]. The SCC problems encountered in (BWR) exemplify the engineering importance of the sensitization phenomenon. However, it has not been considered as a probable failure mode in PWRs in operating conditions.

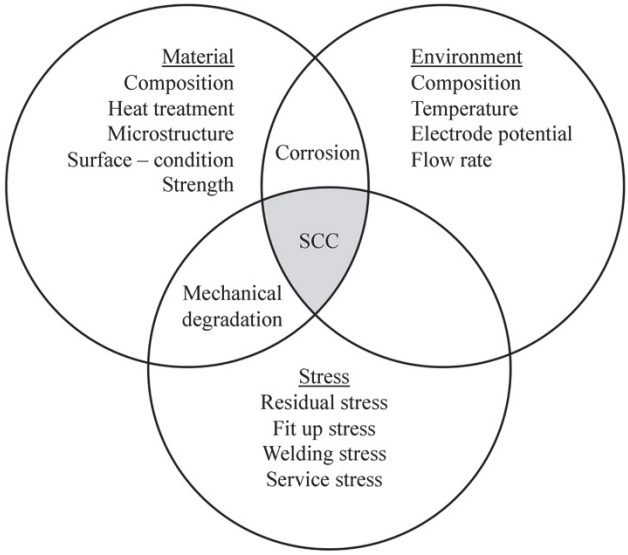

Fig. 2. Factors that contribute to SCC in austenitic stainless steels (Redrawn from [16]).

The most common way to prevent sensitization is to avoid any fabrication or annealing treatments that exposes the stainless steel to the sensitization temperature regime. However, this is not possible in the case of stress relieving heat treatments and welding operations. The other common methods to control sensitization are (a)

prevention of chromium carbide precipitates by lowering the carbon content (b) stabilizing the stainless steel by adding titanium or niobium (c) dissolving the chromium rich carbides with the solution heat treatment followed by rapid cooling through the sensitization temperature range (d) the use of grain boundary engineering [17]–[23].

The corrosion resistance in austenitic stainless steels is provided by a continuous passive film, which is a chromium-rich oxide (Cr_2O_3) layer formed at ambient temperatures [24]. When the film is broken, chromium reforms the Cr_2O_3 layer by combining with the oxygen from the air. Even though the Cr_2O_3 layer is very thin, in the range of 1 to 15 nm, it is chemically stable and adheres firmly to the surface of the alloy. In contact with water, an insoluble passive film is formed that consists of an inner barrier layer comprising oxides of iron and chromium and an outer layer of chromium hydroxides. It has been reported that the chromium enrichment in the passive film might not be homogeneous at the nanometre scale and heterogeneities in the film thickness are responsible for the breakdown of the passive film leading to loss of corrosion resistance [25]. The alloys that contain molybdenum and nickel forms passive films with no thickness fluctuations, thus providing better localised corrosion resistance [26]–[28]. It has been observed that after the initiation of localized corrosion, the presence of molybdenum either mitigates the breakdown of the passive film or repairs the passive film after breakdown [29]. The behaviour of the passive film and its relative stability can be estimated in the laboratory using electrochemical potentiodynamic testing by anodically polarizing the sample, as can be seen in Fig. 3 [30]. With an increase in potential from the corrosion potential (E_{corr}), the current increases due to dissolution up to a critical current density i_{cp}. This defines the starting point of stability for the passive films that occurs at potentials higher than the primary passivation potential (E_{pp}). Above this potential, the current falls several orders of magnitude to the passivation current i_p above the passivation potential E_p. When the potential is increased further into the transpassive region, the breakdown of the passive film will occur leading to localised corrosion. Different characteristic regions are identified that help in comparison of the corrosion behaviour of different alloys considering the relative positions and extensions of current densities and potentials [31], [32]. In the cyclic polarization test, a variant of the potentiokinetic test, the sample surface is activated and reactivated in two loops to measure intergranular corrosion.

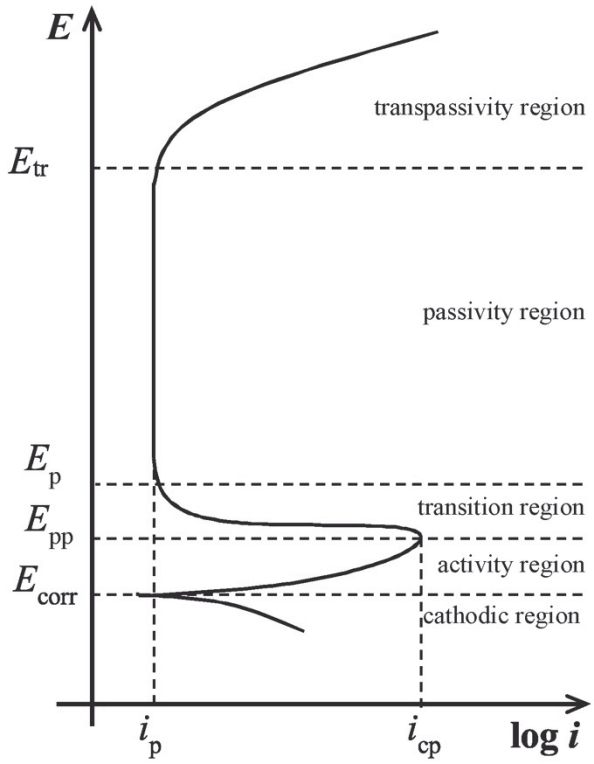

Fig. 3. Schematic representation of an anodic polarization curve (Reprinted by permission from [30] © 2017 Elsevier).

2.3 Sensitization and mechanisms of sensitization

Sensitization in austenitic stainless steels is due to the formation of a chromium depleted region adjacent to the grain boundaries in the austenitic matrix. The chromium depletion results from the nucleation and growth of chromium carbides on the grain boundaries and the differences in the diffusivities of carbon and chromium in the austenite matrix [33]. Thus, the phenomenon of sensitization is controlled by the thermodynamics and kinetics of chromium carbide nucleation and growth. It occurs in the temperature and heat treatment conditions where the chromium carbides are thermodynamically stable and the diffusivity of chromium

is sufficient for the nucleation and growth of the chromium carbide [34]. Therefore, sensitization identifies a microstructural condition and not corrosive behavior directly.

There have been three major theories to explain the phenomenon of sensitization and thereby IGC in stainless steels: (1) the segregation theory, (2) the noble carbide theory, and (3) the chromium depletion theory.

The segregation theory proposed by Aust et al.[35]–[37] proposes that soluble segregates and secondary phases are formed continuously along the grain boundary path and are attacked in highly oxidising media like HNO_3 - Cr_2O_7 solutions. The immunity to IGC in stabilised microstructures was explained in terms of preferential segregation of solute at the carbide-austenite matrix interface or by the redistribution of deleterious solute by preferential solute in the carbide. Intergranular corrosion is observed in 316 stainless steel with extensive grain boundary sigma (σ) phase precipitation in less oxidising media. The segregation theory could not explain this observation of IGC in less oxidising media. The main drawback of the theory is that it does not consider the importance of the oxidising power of the corroding environment. Microhardness measurements in the grain boundary area are the only supporting evidence of the solute segregation theory other than intergranular attack [38]. General and intergranular corrosion takes place in highly oxidising solutions and the attempts to extend the theory to carbide sensitised steels have been unconvincing.

Stickler and Vinckier [39] proposed an electrochemical theory, known as the noble carbide theory, for intergranular corrosion of sensitized austenitic stainless steel. According to the theory, it is assumed that corrosion is a galvanic reaction between noble carbide particles and the adjacent less noble matrix and that the corrosion proceeds rapidly along grain boundaries when there is a path of continuous chromium carbides [37]. The presence of a chromium depleted zone is not considered in this theory. The theory failed at explaining the immunity of stabilised stainless steel with continuous grain boundary precipitates to the intergranular attack. It also failed in explaining the desensitization phenomenon in the presence of intergranular carbides.

Bain et al. [40] were the first to propose that the chromium depleted zone adjacent to intergranular chromium carbide was responsible for the susceptibility of the material to intergranular corrosion. It was speculated that the chromium concentration profile across two adjacent grains was like that shown in Fig. 4. The model is based on the following assumptions. (a) A minimum of 12% chromium by wt. is required to have a protective passive film in stainless steels. (b) The

chromium carbide contains about 95% chromium by wt. and the bulk up to 18% and thus the chromium depletion occurs in the matrix adjacent to the carbide. (c) During the sensitization heat treatment, the diffusion of chromium in the matrix is too slow to permit the instantaneous replenishment of chromium in the depleted regions. (d) When the chromium content goes below 12%, the material corrodes preferentially at the interface.

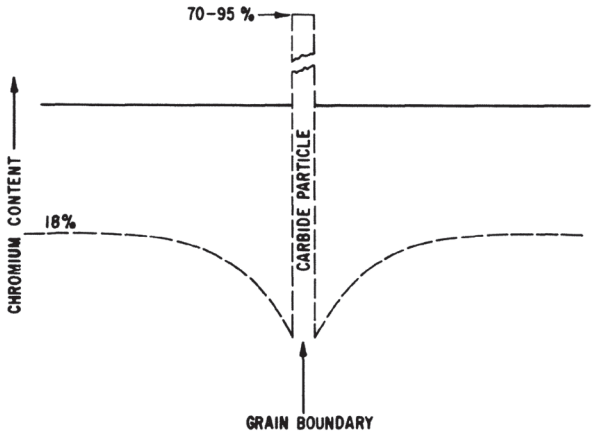

Fig. 4. Chromium depletion at grain boundary containing chromium carbide (Reprinted by permission from [37] © 1973 Plenum Press).

This chromium depletion theory successfully explained the influence of an oxidising environment, heat treatment variables and the effect of different elements. It was argued that during self-healing, back diffusion of chromium should not occur when the chromium carbide particles are still growing [41]. However, it was shown theoretically that self-healing can occur simultaneously with the precipitation of carbides by Stawström and Hillert [42]. It was also shown that the lattice diffusion of chromium is the rate limiting step for sensitization, thereby supporting the chromium depletion theory [34], [43], [44]. The theory was further confirmed by the direct observation of chromium depleted zone of widths ranging 25–200 nm in scanning transmission electron microscopy (STEM) near the interface between grain boundary carbides and the matrix [45]–[50].

2.4 Factors affecting sensitization

2.4.1 Alloy composition

Carbon and chromium are the major compositional variables that affect the sensitization and self-healing phenomenon, although the presence of other alloying elements like nickel, manganese, titanium, niobium, molybdenum also affect the precipitation of chromium rich carbides. The best way to demonstrate the effect of alloy composition is using Time - Temperature - Sensitization (TTS) diagrams. These diagrams provide information about the time required for isothermal sensitization at various temperatures and can be used in choosing the conditions of annealing that do not result in sensitization. It is well established that TTS curves are displaced towards longer times with decreasing carbon content. This can be attributed to the lower availability of carbon to form the chromium rich carbides. The maximum carbon content that is not susceptible to sensitization is related to the presence and effect of other alloying elements in the material like chromium, nickel, silicon, molybdenum, nitrogen, manganese and also niobium and titanium in stabilized stainless steels. Chromium also has a profound effect on the sensitization characteristics. Stainless steel with higher chromium content is more resistant to sensitization and also longer heat treatment times are required in these alloys to achieve chromium depletion below the critical level.

Nickel is an austenitic stabilizer but its presence increases the diffusivity of carbon particularly when the Ni content is more than 20% by wt. [51]. To avoid intergranular corrosion in 25 Cr - 20 Ni stainless steels, it is recommended that carbon content should be less than 0.02% by wt. To avoid sensitization, Cihal [52] proposed a balance between carbon, chromium and nickel concentrations by proposing an effective chromium content (Cr^{eff}) for 304 stainless steels.

The influence of molybdenum is similar to that of chromium, as Mo in solution contributes to the passivation of the stainless steel. Mo gets incorporated into the carbides and thus molybdenum depletion is observed along with chromium depletion. It was reported that the solubility of carbon in austenite reduces with increase in Mo content and thus accelerates the precipitation of carbides [53].

The addition of manganese reduces the activity of carbon in austenite and thereby increases its solubility. This slows down the precipitation rate of carbide [34], [53]. Contrary to that, some reports claimed alloys with higher manganese content are more susceptible to intergranular corrosion than that of lower manganese alloys [4], [54], [55]. It was also established that the addition of stable

carbide forming elements to the Fe-Mn-Cr steels do not have considerable impact on the sensitization behaviour. The combined effect of manganese and nitrogen was studied by many researchers who observed that their presence accelerated the formation of intragranular precipitation and intermetallic phases [56]. In the case of commercial and high purity stainless steels, silicon promotes sensitization. In highly oxidising solutions, silicon is segregated to the grain boundaries and increases the susceptibility to sensitization. Silicon simultaneously affects the activities of carbon and nitrogen resulting in the formation of 'Pi' phase (carbonitride) with increasing silicon contents [57], [58]. The effect of nitrogen was extensively studied and its addition below 0.16% by wt. reduced the sensitization kinetics. An increase in nitrogen up to 0.25% has been shown to increase sensitization kinetics due to the precipitation of Cr_2N [48], [58].

2.4.2 Influence of grain size

Grain size of the stainless steel have significant effect on the sensitization and self-healing behaviour. Grain size has major influence on the intergranular corrosion behaviour as carbide precipitation and grain boundary chromium depletion are dependent on the grain size. It was reported by Beltran et al. [59] that decreasing the grain size from 150 to 15 μm decreased the effect of deformation. He reported increased sensitization and desensitization kinetics with a decrease in grain size from 150 to 15 μm and attributed it to the smaller diffusion distances required for the mid-grained chromium atoms to reach the grain boundary in the case of small grained material [59], [60]. Pascali et al. [61] reported a delay in the sensitization and desensitization at lower temperatures when the grain size is increased from 17 to 68 μm. Yu et al. [62] concluded that the degree of sensitization (DOS) from electrochemical potentiodynamic reactivation tests decreased with solution treatment temperature and time. Li et al. [63] showed that the kinetics of chromium carbide precipitation are slower in large grained samples. The ccombined effects of carbon content, grain size and strain rate on the time to sensitization in 304 stainless steels was reported by Trillo et al. [47] and can be seen in Fig. 5 where D is the average grain size.

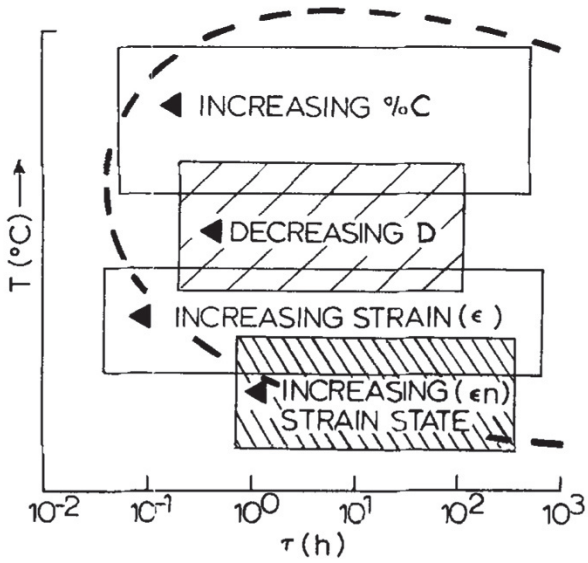

Fig. 5. Schematic diagram showing the combined effect of carbon content, strain rate and grain size on the time to sensitization (Reprinted by permission from [47] © 1995 Elsevier).

2.5 Experimental determination of degree of sensitization

There are ASTM A262 standardised tests to determine the susceptibility of stainless steels to sensitization [64]. These include Practices A, B, C, E, F and G-108 and are commonly used as qualification tests that can only determine the material's acceptability. Electrochemical techniques are used for the quantitative determination of sensitization.

In ASTM practise A, which is a screening test, only grain boundary chromium carbides are preferentially dissolved resulting in an etched microstructure showing step, dual and ditch features. When 'ditch' features are observed in the etched microstructure, there is a possibility of intergranular corrosion, which is further tested using immersion tests ASTM A-262 B to F. Practise B detects intergranular corrosion related to the precipitation chromium carbides and corresponding chromium depletion. In some molybdenum bearing steels, the σ phase is attacked in this practise. Practise C, also known as the Huey test, is used only when the alloy is intended to be used in nitric acid environments. Practice E, also known as Strauss

test recommends a bend test after exposing the material to Cu-CuSO4-H_2SO_4 medium. Tensile properties and electrical resistance of the material are affected by intergranular corrosion and are used in Practise E to quantify the DOS after exposure to Strauss test solution. In molybdenum bearing stainless steels, the IGC exclusively from grain boundary chromium depletion can be obtained using the test described in Practise F. Also, the susceptibility of low-carbon grades to IGC can be evaluated using this practise. The tests are intended for screening heavily sensitized austenitic stainless steels, when they are exposed to highly corrosive environments that may cause severe IGC attack [65].

The chromium depletion along the grain boundaries is related to the width and depth of the chromium depleted zone, and the length of grain boundary covered by chromium depleted zones. The electrochemical techniques and the derived electrochemical parameters are sensitive to all these parameters and can be correlated to DOS. In the potentiodynamic anodic polarization technique, the specimen is anodically polarized with a scan rate of 50 mV/min in deaerated 1 N $HClO_4$ + 0.2 N NaCl [66]. The presence of chromium depleted zones is indicated by the occurrence of a secondary anodic peak, and the corrosion current density corresponding to that peak can be related to DOS [67]. The test fails to detect mild sensitization and some reports claim that the DOS does not influence the critical and passive current densities [68], [69]. The potentiostatic etching test measures the passivation potential during polarization to estimate the chromium content along the grain boundaries. The test, when conducted at various potentials for 24 h, determines the potential above which IGC does not occur and thus estimates the grain boundary chromium content [70]–[72]. The electrochemical potentiokinetic reactivation (EPR) test is a non-destructive method to quantitatively determine DOS. Cihal et al. [73] originally proposed the single loop EPR (SL-EPR) method. It was later developed by other researchers and has been standardised as ASTM G 108. This is one of the two types of EPR methods. In the SL-EPR method the specimen is initially passivated in 0.5 M H_2SO_4 + 0.01 M KSCN at +200 mV (SCE) and then reverted to a corrosion potential at a constant scan rate. Larger corrosion currents are observed in the samples that are sensitized as a protective oxide film is not formed in the regions with chromium content less than 12–13% [74]. In this method, the reactivation of the chromium-depleted, sensitized region is revealed as an anodic peak in the plot of current against potential. The electric charge is a measure of DOS and is proportional to the area under the reactivation peak. To accommodate the effects of grain size and temperature, the DOS has been correlated to the measured EPR parameters. The SL-EPR experiments that start

from the transpassive potential region were adopted by Charbonnier et al. [75], where the scan is extended through the active potential that produces an anodic peak. The dissolution of carbides occurs in the transpassive region during the potential scan, thereby detaching these carbides from the grain boundaries. Thus, during reactivation, only chromium depleted regions dissolve and contribute to the measured current. However, the reactivation behaviour is surface sensitive and also the SL-EPR method requires the measurement of specimen grain size. This led to the development of the Double Loop - EPR (DL-EPR) test method. In this method, the sample is subjected to two scans, activation and reactivation scans. The sample is anodically polarised from the corrosion potential to the passive potential, that is followed by a reactivation scan to open circuit potential. In this method, the ratio of peak reactivation current density (I_r) to the peak activation current density (I_a) is used as a measure to determine the DOS according to the standard EN ISO 12732:2008 [76]. During the forward scan, the surface irregularities are dissolved actively and the passive film is established after reaching the passive potential. Now the reactivation scan attacks the passive layer by primarily dissolving the chromium depleted regions that are corrosion susceptible due to sensitization. The magnitude of peak reactivation current density increases with an increase in chromium depletion. To compare the DOS from steels with different grain sizes, the reactivation charge from the reactivation scan is normalised by either grain boundary length or grain boundary area. A new approach to improve the measurement of DOS from DL-EPR data was proposed by Rahimi et al. [77] using a cluster compactness parameter that measures the breakup of the corrosion susceptible grain boundary network.

2.6 Modeling

There is a long history of phenomenological and mechanistic modelling of sensitization. Cihal [52] phenomenologically modelled sensitization by normalizing the effects of bulk composition on IGC and IGSCC susceptibility, but the predictions were limited to qualitative estimations. After the proposal of grain boundary chromium depletion theory, mechanistic modelling of the sensitization phenomenon began. The proposed models for chromium depletion can be classified into two types: reaction theories and kinetic theories. The chromium content and the size of the chromium depleted region adjacent to the $M_{23}C_6$ precipitate continue to change during the nucleation and growth of $M_{23}C_6$ carbide. In reaction theory, it is assumed that the chromium depleted zone is formed instantaneously after the

nucleation of chromium carbide, thus both the chromium content and width of chromium depleted zone are then at a minimum. On the other hand, in the kinetic theory, after the formation of carbides, there is a time lag in reaching the minimum chromium concentration. This is in line with experimental observations apparently due to the low chromium diffusivity relative to that of carbon. According to the reaction theory, the description of the chromium depletion phenomenon is based on the precipitation reaction of the carbides. The initial models developed for estimating sensitization by Stawström and Hillert, Was and Kruger, and Bruemmer have used this theory for estimating the chromium depletion profiles.

In 1969, Stawström and Hillert developed a model for the predicting grain boundary precipitation and sensitization in 18Cr-8Ni stainless steel [42]. It was assumed that local equilibrium exits at the interface between $M_{23}C_6$ carbide and the austenite matrix. Iso-activity of carbon was also assumed. It is also assumed that chromium diffusivity inside the $M_{23}C_6$ carbide film is high enough to keep the chromium content there at a constant level. At any time, the situation at the $M_{23}C_6$ carbide - austenite matrix interface is given by a tie-line in the phase diagram. The iso-activity tie-line where the chemical potential of carbon is the same in the austenite matrix and at the interface was identified by calculating the initial carbon activity. The chromium concentration at the interface can thus be determined from the phase diagram. The basic rate equation was obtained using Fick's second law, and the flux of chromium at the interface was obtained using mass balance theory as in Zener's model [78]. By solving the above two equations, chromium concentration profiles across the carbide - austenite matrix were predicted. However, in this model by Stawström and Hillert, the multicomponent effects are not taken into consideration in either the thermodynamic or kinetic modelling. In the thermodynamic modelling, the interaction effect of chromium and nickel is neglected and in the kinetic modelling, the diffusion fluxes of only iron and chromium are considered.

A simple thermodynamic model was proposed by Hall and Briant [79] to estimate the interfacial chromium concentration in the austenite matrix at the carbide-matrix interface which is based on the equilibrium reaction

$$6\,\mathrm{C} + 23\,\mathrm{Cr} \rightleftharpoons \mathrm{Cr}_{23}\mathrm{C}_6. \tag{1}$$

The equilibrium constant K_{eq} of Eq. (1) is

$$K_{eq} = \frac{1}{\left(\gamma_{Cr} C_{Cr}^{\gamma\beta}\right)^{23} a_C^6}, \tag{2}$$

where γ_{Cr} is the activity coefficient of chromium, $c_{Cr}^{\gamma\beta}$ is the chromium concentration in equilibrium with the carbide, a_c is the activity of carbon in the austenitic matrix. The activity of carbon was obtained using the formulation of Natesan and Kassner [80], which considers the effect of carbon, chromium, manganese and molybdenum on the activity of carbon. The equilibrium constant was obtained from the literature thereby giving the interfacial chromium concentrations. The modelling of the chromium concentration profiles perpendicular to the grain boundary was done using an approach for the diffusion controlled growth of precipitates originally proposed by Zener [81] and later expanded by other researchers [82], [83]. In this model, multicomponent effects were not considered in the thermodynamic calculations.

Was and Kruger [84] proposed a model to describe the development of chromium depleted zones in Ni-Cr-Fe-C alloys and assumed that only M_7C_3 carbides are precipitated along the grain boundary. According to Kohler [85], free energy expressions for the Ni-Cr-Fe-C system can be described using binary interaction parameters. However, these are not sufficient to model the thermodynamics of carbide precipitation. Therefore, Was and Kruger introduced a ternary interaction parameter by approximating the quaternary system as a ternary system of Cr+(Ni+Fe)+C. The interfacial chromium concentration in the austenite matrix was determined using the equilibrium constant for Cr_7C_3 precipitation used in the Hall and Briant model. The chromium depleted region was quantitatively estimated as a function of time, temperature, alloy composition and grain size. Fick's 2nd law was discretized and solved numerically. However, only the diffusion of chromium was considered in predicting the chromium concentration profiles and thus neglecting the multicomponent effects.

Bruemmer [5] assumed the carbides to be $Cr_{23}C_6$ and performed thermodynamic calculations similar to those of Hall and Briant. In 316 stainless steels, molybdenum might be present in the $M_{23}C_6$ carbides and be depleted during their growth. To deal with this, Hall and Briant used the effective chromium concentration developed by Fullman [86], which combines the effects of both molybdenum and chromium. An empirical relation was established to determine the activity coefficient of chromium thereby giving the interfacial chromium concentrations. The kinetics of precipitation were modelled in a similar way to that used by Stawström and Hillert. Although the model could quantitatively predict sensitization, multicomponent effects were not considered in modelling the thermodynamics (although molybdenum is considered) and kinetics of

precipitation. Mayo [87] developed a semi-empirical model for the prediction of grain boundary chromium depletion in the alloy 16 Ni - 9 Cr - Fe. Empirical equations were used in estimating the chromium concentration in the matrix in equilibrium with the chromium carbide. Mayo defined holding time to reach the minimum chromium concentration (t_c) at the carbide-matrix interface, arguing the assumption that it reaches the minimum chromium concentration instantaneously is incorrect. According to his model, the Cr concentration profile is given by

$$c(z,t) = c_{Cr}^{\gamma\beta} + (\bar{c}_{Cr}^{\gamma} - c_{Cr}^{\gamma\beta}) erf(\frac{z}{2\sqrt{D^{\gamma}t}}), \quad (3)$$

where $\bar{c}_{Cr}^{\gamma}$ is the far-field concentration of chromium, D^{γ} is the bulk diffusivity, and t is the time, z is the position of the interphase.

An error function is used to express the chromium concentration profile as a function of diffusion time. Like in the previous models, multicomponent effects were neglected in the thermodynamic and kinetic calculations.

Similar to Mayo, Sahlaoui et al [88] also argued the instantaneous nucleation of carbide and instantaneous attainment of the thermodynamic equilibrium concentration of chromium at the interface between carbide and austenite. In his work, the evolution of chromium concentrations at the carbide-matrix interface and the chromium concentration profiles were predicted by a two-stage diffusional model, i.e. dechromization and rechromization. τ is the time required for nulceation and growth of carbides, t_s is time to reach critical chromium concentration at the interface, t_c is the time to reach minimum chromium concentration, t_d is the time taken for self-healing. During dechromization, the chromium concentration in the matrix adjacent to carbide continues to decrease until a minimum value $c_{Cr\,min}^{\gamma\beta}$ is reached. It can be calculated using

$$c_{Cr}^{\gamma\beta} = \bar{c}_{Cr}^{\gamma} exp\left(-k_1 \frac{t}{t_c}\right), \quad (4)$$

where k_1 is a constant. The value $c_{Cr}^{\gamma\beta}$ can then be used to evaluate the chromium concentration profile in the depleted zone using Fick's second law

$$c(z,t) = c_{Cr}^{\gamma\beta} + (\bar{c}_{Cr}^{\gamma} - c_{Cr}^{\gamma\beta}) erf(\frac{z}{2\sqrt{D^{\gamma}t}}), \quad (5)$$

where z is the position of the interface.

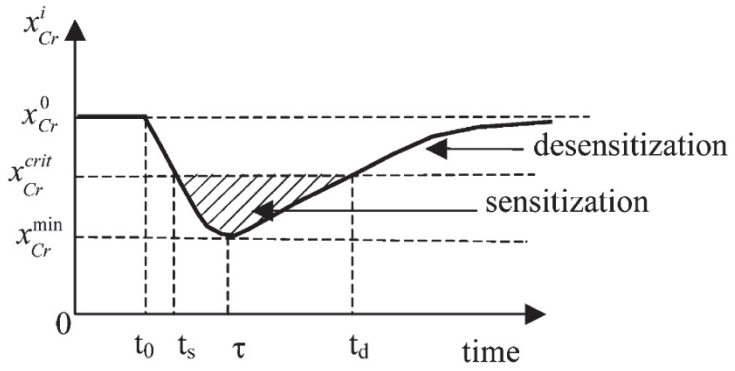

Fig. 6. Sensitization and desensitization based on the chromium concentration at the carbide-matrix interface (Reprinted by permission from [88] © 2002 Acta Materialia Inc.).

According to Sahlaoui [88], the nucleation and growth of chromium carbides start at time t_0 after which dechromization starts and the chromium concentration at the interface (X_{Cr}^{i}) starts decreasing as shown in Fig. 6. Sensitization begins after time t_s when X_{Cr}^{i} goes below a critical value X_{Cr}^{crit}. A partial thermodynamic equilibrium is reached between carbide and matrix when X_{Cr}^{i} reaches minimum value of chromium X_{Cr}^{min} after time τ. Carbon concentration decreases uniformly with time and leads to an increase in the local chromium activity that provides the driving force for chromium diffusion to the depleted regions from the bulk, i.e. rechromization. Desensitization begins after time t_d when X_{Cr}^{i} goes above the critical chromium value. The chromium concentration profile was calculated based on the inter-diffusion through a plane that divides the depleted zone into two equal areas in which the transport of the chromium atoms across the two areas takes place without accumulation, and is given as

$$c(z,t) = \frac{1}{2}\left(c_{Cr}^{\gamma\beta} - \bar{c}_{Cr}^{\gamma}\right) erf\left(\frac{z}{2\sqrt{D^{\gamma}t}}\right) + \bar{c}_{Cr}^{\gamma}. \quad (6)$$

Sahlaoui does not describe how the thermodynamic calculations are made nor how interfacial chromium concentrations are obtained. The assumption that self-healing occurs only after the completion of carbide growth may cause thermodynamic instability at the carbide-austenite matrix interface.

To solve the diffusion equations for multicomponent systems maintaining local equilibrium at the interface, Coates [89], [90] developed the flux-balance method. The diffusivity of carbon is much higher than that of the other alloying elements and it was assumed by Stawstrom and Hillert [42] that the activity of carbon is

always constant throughout the material. This isoactivity of carbon is used to attain the conditions required for the assumed local equilibrium conditions at the interface between $M_{23}C_6$ and the austenite matrix. In general, the tie line provides the compositions at the interface. The operative tie line that governs the compositions at interface is obtained from the iso-activity line for carbon that passes through the composition of the austenite. The same is shown in the schematic Fe-Cr-C ternary in Fig. 7. As the growth of the carbide proceeds, the carbon activity decreases and the interfacial chromium concentration in the austenite increases along the curve from z_i to z_n. However more advanced DICTRA calculations do not require the assumption of constant carbon activity.

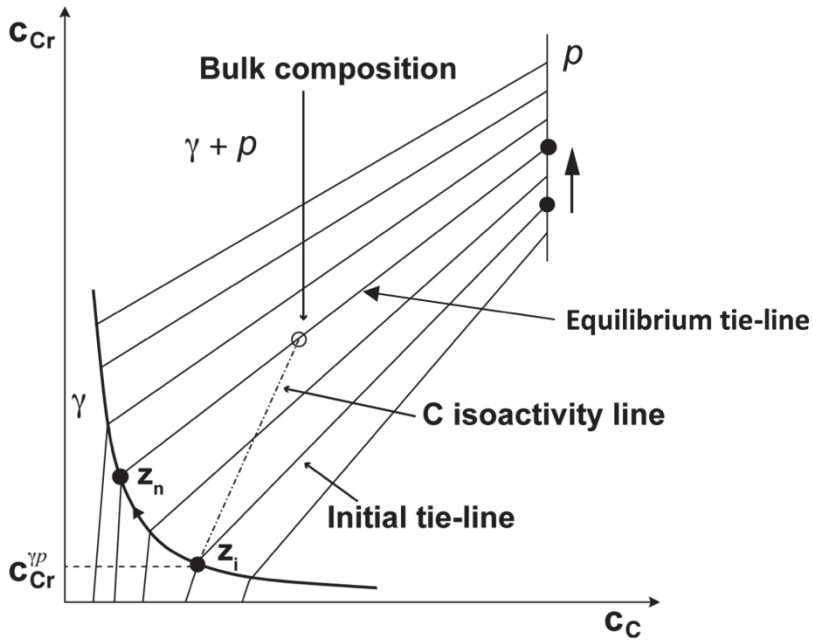

Fig. 7. Schematic Fe-Cr-C ternary diagram showing the change of equilibrium during precipitation (Reprinted by permission from Paper II © 2019 ISIJ).

Sourmail et al. [91] modelled the grain boundary precipitation of $M_{23}C_6$ carbides with the use of MTDATA simulation software for thermodynamic data. A program in FORTRAN was used to interface with MTDATA and obtain the flux balance line with a unique interface velocity for all the elements. The diffusion equations were

then solved using finite difference method to obtain chromium concentration profiles. The carbide-matrix interface should remain in equillibrium during the diffusion controlled growth. Two stage model described by Sahlaoui violates this assumption. Concentrations at interface are obtained by flux balance tie-line instead of mass balance tie-line. Mass balance tie line gives different interface velocities for different elements. The fluxes are expressed as

$$J_i^L = -c_i M_i \nabla \mu_i, \tag{7}$$

where J_i^L flux of element i in the lattice fixed frame of reference, c_i concentration, M_i mobility, μ_i chemical potential of element i, and the evolution of concentration with time is given by

$$\frac{\partial x_i}{\partial t} = \nabla \sum (\delta_{ik} - x_i \frac{V_k}{V_m}) x_k M_k \nabla \mu_k, \tag{8}$$

where x_i is the mole-fraction of the component i, V_k is the molar volume of the component i, V_m is the molar volume of austenite. However, no correlations between the calculated concentration profiles and DOS were made.

2.7 CALPHAD technique

The term CALPHAD means **Cal**culation of **Pha**se **D**iagrams from thermodynamic models that are adjusted to the available experimental data. The method uses the available theoretical and experimental data to assess the parameters that define Gibbs energy models [92], [93]. The calculation of phase diagrams was first done from the Gibbs energy models proposed by van Laar in 1908 [94]. However, Kaufman et al. [95] were the first to give a description of the CALPHAD technique in 1970. They developed the concept of "lattice stability" which is essential for the development of a multicomponent thermodynamic database. The development of thermodynamic models based on experimental data and theoretical models for the description of different phases is still being done.

The Gibbs energy of all the phases as a function of temperature, pressure and composition are needed. Interaction parameters are used to describe the deviations from ideal behaviour and are optimized to fit the experimental data. The thermodynamic descriptions of all the systems are combined and stored in databases. These databases are used for the calculation of phase diagrams by means of software that minimizes the Gibbs energy. They can be extended to obtain thermochemical properties at temperatures and compositions where experimental data is not available. The CALPHAD technique can be used in applications that

need a thermodynamic description of a system. The Gibbs energy state function can be used to derive thermodynamic quantities like heat capacity, chemical potentials, and thermal expansion.

The model of a particular phase depends on its physical and chemical properties like crystallography, order-disorder transitions, magnetic properties and the type of bonding. The crystal structure of the phase is considered by dividing it into sublattices that are characterized by different crystallographic symmetries and numbers of nearest neighbours.

The Gibbs energy of a phase can be given by

$$G_m = G_m^{srf} + G_m^{phy} - T \cdot S_m^{cnf} + G_m^E, \tag{9}$$

where G_m^{srf} is the Gibbs energy of an unreacted mixture of constituents of the phase m and srf stands for "surface of reference", G_m^{phy} is the physical models' contribution to Gibbs free energy such as magnetic transitions, T is the temperature, S_m^{cnf} is the configurational entropy of the phase that includes possible arrangements of the constituents in the phase along with the random arrangements on the various sublattices. G_m^E is the excess Gibbs energy, which for a solution phase can be represented with Redlich-Kister polynomials is as follows

$$G_m^E = \sum_i \sum_{j<i} x_i x_j \left(\sum_{r=0}^{m} \Phi_r^{i,j} \left(x_i - x_j \right)^r \right), \tag{10}$$

where $\Phi_r^{i,j}$ are the interaction parameters that are stored in the thermodynamic databases, where x_i, x_j are the mole fractions of the constituents i and j respectively.

The molar Gibbs energy, G_m of a phase with a fixed composition, that can be an element or stoichiometric compound, depends on the temperature according to

$$G_m - \sum_i b_i H_i^{SER} = a_0 + a_1 T + a_2 T ln(T) + a_3 T^2 + a_4 T^{-1} + a_5 T^3 + \cdots, \tag{11}$$

where b_i is the stoichiometric coefficient, H_i^{SER} is the enthalpy of the element i in the reference state, that is at 1 bar and 298.15 K. The a_i's are the coefficients that express the temperature dependence of the end members (formed when each sublattice is occupied by only one kind of species) and are taken from the SGTE (Scientific Group Thermodata Europe) thermodynamic database [96]. Similar power series in temperature can be used to describe the metastable structure of the end members. Lattice stability is this difference between the Gibbs energy of the phase in its stable structure and in its metastable state [97]. In the case of solution phases with all constituents mixing on one sublattice, the Gibbs energy is given by

$$G_m = \sum_{i=1}^{n} x_i G_i^0 + RT \sum_{i=1}^{n} x_i \ln(x_i) + G_m^E. \quad (12)$$

The first term is the surface of reference where x_i is the mole fraction of the element i, G_i^0 is the standard Gibbs energy of the pure element i. The second term represents the enthalpy of mixing and the third term represents the excess energy due to deviation from the ideal solution behaviour which can be given by

$$G_m^E = G_m^{E,bin} + G_m^{E,ter} + G_m^{E,hig}, \quad (13)$$

where $G_m^{E,bin}$, $G_m^{E,ter}$ and $G_m^{E,hig}$ are the binary, ternary and higher-order excess energy terms respectively. The binary and ternary excess energies are given by

$$G_m^{E,bin} = \sum_{i=1}^{n-1} \sum_{j=i+1}^{n} x_i x_j L_{ij} \quad (14)$$

and

$$G_m^{E,bin} = \sum_{i=1}^{n-2} \sum_{j=i+1}^{n-1} x_i x_j x_k L_{ijk}, \quad (15)$$

where x_i, x_j and x_k are the mole fractions of the constituents i, j, k respectively. L_{ij} is the binary interaction parameter and L_{ijk} is the ternary interaction parameter and are related to the bond energies between similar and dissimilar atoms in a solution.

For a stoichiometric phase, there is only one constituent on each sub lattice. The phases that have more than one sublattice and with compositional variations are treated as solution phases and can be modelled using the Compound Energy Formalism (CEF) [98]. Fig. 8 shows the workflow of CALPHAD and Thermo-Calc. The thermodynamic optimization section refers to the CALPHAD technique of creating thermodynamic functions and storing them in databases.

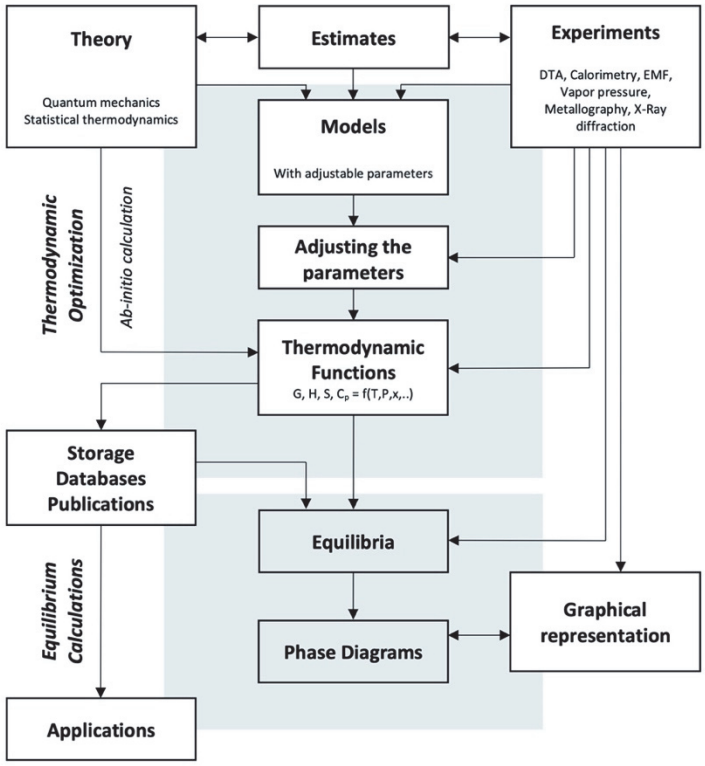

Fig. 8. CAPLHAD and Thermo-Calc methodology (Redrawn from [99]).

3 Experiments and Modeling

3.1 Materials

In this work, five different grades of 301 austenitic stainless steels are used for the sensitization studies. All the grades are provided in the form of 3 mm thick sheets by Outokumpu Stainless Oy Tornio, Finland. The grades and compositions are listed in Table 2. Cr^{eff} , the effective chromium content of alloys, was calculated according to an equation proposed by Parvathavarthini [99], on the basis of which a larger Cr^{eff} implies higher sensitization resistance . As can be seen from Table 2, these Cr^{eff} values vary from 6.72 to 15.89 thereby representing low to high sensitization resistance.

Table 2. Compositions of all the stainless steel grades used in the thesis [Papers I–V].

Steel grade / % by wt.	C	Cr	Ni	Si	N	Mn	Mo	Cu	Cr^{eff}
1.4310	0.10	16.80	6.36	0.95	0.06	1.20	0.06	0.31	6.72
1.4301	0.04	18.10	9.07	0.44	0.02	1.09	0.30	0.39	12.35
1.4303	0.04	18.14	12.39	0.45	0.02	1.17	0.20	0.25	12.35
1.4307	0.02	18.12	8.08	0.37	0.04	1.54	0.26	0.42	15.40
1.4318	0.02	17.58	6.67	0.43	0.15	1.18	0.06	0.16	15.89

For Papers I–IV, EN 1.4310 grade was used and for the Paper V, all the five compositions were used for the sensitization study.

Paper I investigates the sensitization behaviour in EN 1.4310 alloy for non-isothermal conditions while Papers II–V are focussed on studying the isothermal sensitization behaviour. In all of the papers, the material is initially solution treated and homogenized at 1100 °C for 2 h followed by water quenching. This brings precipitated carbides as well as other intermetallic phases into the solution [101]. Then different heat treatments are employed to induce various levels of sensitization and desensitization in the alloy which are discussed in the next section.

3.2 Experimental methods

Heat treatments have been done using a Gleeble 3800® thermomechanical simulator and also in the furnace. In Paper I, non-isothermal heat treatments were carried out from room temperature to different peak temperatures (PT) 700, 800, 900 and 1000 °C at a heating rate of 50 °C/s, held there for 2 s before cooling down

to room temperatures with cooling rates of 0.125, 2 and 32 °C/s using the Gleeble thermomechanical simulator (Table 3). Also, in Paper II, isothermal heat treatments are carried out at 700, 760, 820 °C with a heating rate of 50 °C/s, held there for time periods ranging 1 to 80 mins before rapidly cooling to room temperatures using the Gleeble thermomechanical simulator. For Papers II–V, the heat treatments are done in a furnace as longer treatment periods are required to study the self-healing phenomenon in the material (Tables 4–7). The heat treatments employed in Paper IV for producing material with various grain sizes resulted in decarburization as shown in Table 6. Bulk chemical composition analysis was done using glow discharge optical emission spectroscopy (GDOES), GDA 750 Spectruma Analytik GMBH.

Oxalic acid etching according to ASTM A262 Practise A [64] has been used for the classification of etch structures in sensitized, desensitized and unsensitized samples. This test tells whether a specimen is free of susceptibility to intergranular corrosion, rather than a quantitative degree of sensitization and, therefore, it should be used in conjunction with other evaluation tests, in this work, with the DL-EPR test.

Table 3. Non-isothermal heat treatments employed in Paper I (Reprinted by permission from Paper I © 2017 Associazione Italiana di Metallurgia).

Heating rate (°C/s)	Peak temperature (°C)	Holding time at peak temperature (s)	Cooling rates (°C/s)
50	700, 800, 900, 1000	2	0.125, 2, 32

Table 4. Heat treatment parameters used to produce sensitized samples in Paper II (Reprinted by permission from Paper II © 2019 ISIJ).

Heating rate to peak temperature (°C/s)	Peak temperature (°C)	Holding times (min)
50	700	1, 10, 20, 30, 40, 80
50	760	1, 5, 10, 20, 30, 40
50	820	1, 5, 10, 20, 30, 40

Table 5. Heat treatment parameters used to produce sensitized samples in Paper III (Reprinted by permission from Paper III © 2019 ISIJ).

Holding temperatures (°C)	Holding time (h)
600	3, 6, 10, 24, 48

Holding temperatures (°C)	Holding time (h)
650	3, 6, 10, 24, 48
700	3, 6, 10, 24, 48, 120, 168
760	3, 6, 10, 24, 48
820	3, 6, 10, 24, 48, 120, 240, 480

Table 6. Heat treatment parameters used to produce sensitized samples in Paper IV (Reprinted [adapted] under CC BY license from Paper IV © 2019 Authors).

Heat treatment	Average ECD (μm)	C content (wt.%)	Holding time at 820 °C (h)
1100 °C/2 h (ST)	72 ± 5	0.105	3 to 480
ST + 1200 °C/2 h	90 ± 4	0.085	3 to 480
ST + 1200 °C/4 h	120 ± 3	0.082	3 to 480
ST + 1200 °C/8 h	190 ± 4	0.073	3 to 480

Table 7. Heat treatment parameters used to produce sensitized samples in Paper V (Under CC BY-NC-ND from Paper V © 2020 Authors).

Steel grade	Heat treatment temperature (°C)	Holding times (h)
1.4310	600, 650, 700, 760, 820	3, 6, 10, 24, 48, 120, 168
1.4301	600, 700, 820	3, 10, 24, 48, 120, 168, 240
1.4303	600, 700, 820	3, 10, 24, 48, 120, 168, 240, 480
1.4307	550, 600, 700, 820	3, 10, 24, 48, 120, 168, 240, 480
1.4318	550, 600, 700, 820	3, 10, 24, 48, 120, 168, 240, 480

A VersaStat 3 potentiostat (AMETEK Princeton Applied Research) was used to carry out the double loop potentiokinetic reactivation test (DL-EPR) according to the standard EN ISO 12732 [75]. The tests were conducted using an electrochemical cell with three electrodes: a saturated calomel electrode (SCE) as the reference electrode, platinum as the counter electrode and the sample as the working electrode. The test is not sensitive to the surface finish of the samples and so they were polished to a 600-grit finish before the test. A solution comprising 0.5 M H_2SO_4 + 0.01 M KSCN was used as electrolyte and the tests were run at ambient temperatures with a scan rate of 1.67 mV/s from a potential range of 0 to +400 mV (SCE). Before the start of the test, all the samples are maintained in the

solution for 10 s to 30 min to reach a steady state open-circuit potential. These dwell times at open circuit potential varied among the different alloys. The test consists of two scans, an anodic scan from the open circuit potential into the passive region, which is followed by a reactivation scan from the passive potential to the open circuit potential, as shown in Fig. 9. During the anodic polarization, all the surface irregularities and contours arising due to polishing actively dissolve in the acidic solution causing the activation current peak (I_a). The passive film that is established after reaching the passive potential is attacked during the polarization in the reverse direction causing dissolution primarily at chromium depleted regions that are susceptible to corrosion. This selective dissolution of grain boundaries with chromium contents lower than 12% by wt. results in the reactivation current peak (I_r) [102]. The magnitude of I_r depends on the degree of chromium depletion at the grain boundaries and the total length of grain boundary sampled. The ratio (I_r/I_a)×100 gives the degree of sensitization as a percentage. In Papers IV and V, where materials with different grain sizes are studied, the DOS was normalized with respect to the smallest grain size studied and it was called the normalized degree of sensitization (NDOS). This normalization was done to compensate the effect of grain size on I_r through the total length of grain boundary sampled.

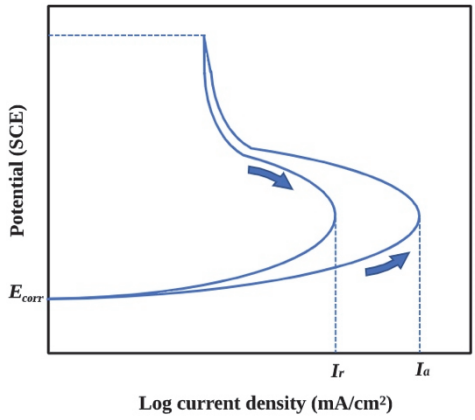

Fig. 9. Double Loop - Electrochemical Potentiokinetic Reactivation test method (Redrawn from [67]).

Field emission scanning electron microscopy (FESEM) (Zeiss Sigma, Carl Zeiss AG) was used for metallographic investigation. Electron back scattered diffraction

(EBSD) analysis was primarily used for grain size measurements in Paper IV. An accelerating voltage of 15 kV with a working distance of 15 mm, tilt angle of 70° and step size of 0.65 μm was using for the EBSD mappings. The MTEX toolbox [104] in conjunction with MATLAB was used in post-processing the EBSD data. EBSD was used for the grain size measurements in Paper IV to accurately measure the variation in grain sizes. The equivalent circle diameters (ECD) of the grains with a grain boundary misorientation angle > 15° were obtained from the EBSD mappings using the MTEX toolbox. The equivalent diameter of a 2-dimensional grain is the diameter of a circle that contains the same area as the shape in question. Bulk chemical composition analysis was done using glow discharge optical emission spectroscopy (GDOES), GDA 750 Spectruma Analytik GMBH. The decarburization occurred during heat treatments to produce different ranges of grain sizes in Paper IV, was determined using the GDOES measurements.

200 kV scanning transmission electron microscopy (JEOL JEM-2200FS EFTEM/STEM) with an energy filter was used for the observation of precipitates in both transmission and scanning transmission (STEM) modes. STEM-EDS (Energy Dispersive X-ray Spectroscopy) was used to quantitatively measure chromium depletion profiles across the $M_{23}C_6$ carbide - austenite matrix interface. The quantification of these profiles was done using a thin film approximation method using Cliff-Lorimer *k*-factors. The *k*-factors can be determined either from the specimen or from the thin standards [104]. The samples for Paper IV were made by electropolishing. Initially, 0.1 mm thick wafers were made from which 3 mm diameter samples were punched. These were further ground to 0.08 mm and then electropolished at 25 V in an electrolyte consisting of perchloric acid, butyl cellosolve, ethanol, and distilled water. Sample preparation for STEM studies in Paper V were done using Field Ion Beam (FIB) milling. FEI Helios Dual Beam FIB system was used with an accelerating voltage of 30 kV and beam currents in the range 90 pA to 9 nA. The lamellae were then thinned and polished with an ion beam.

3.3 Modeling methods

3.3.1 Thermo-Calc

Thermo-Calc is a versatile tool for the thermodynamic calculations. It is based on a powerful Gibbs energy minimizer and is specially designed for complex heterogeneous interaction systems with strongly non-ideal phases and makes use

of many different thermodynamic databases like those developed by the SGTE organization (Scientific Group Thermodata Europe) and the CALPHAD community. In this work, Thermo-Calc is used for equilibrium calculations to predict possible equilibrium phases in the materials. The equilibrium calculation section in Fig. 7 depicts the functioning of Thermo-Calc.

3.3.2 DICTRA

DICTRA, **Di**ffusion **C**ontrolled Transformations, is a tool to simulate diffusion reactions in multicomponent systems with the aid of the Calphad technique. DICTRA makes use of the thermodynamic databases assessed by Calphad through ThermoCalc. The methods suggested by Andersson and Ågren [105] and other researchers [106]–[109] makes it possible to represent multicomponent diffusion data in terms of diffusion mobility parameters that are stored in databases. The atomic mobility of individual species in a multicomponent system is represented as a function of temperature, pressure and composition. In this work, DICTRA is used to solve moving phase boundary problems also called Stefan problems. It was assumed that thermodynamic equilibrium holds locally at all the phase interfaces and multicomponent diffusion equations are solved in various regions of a material [110]. The diffusion equations associated with phase transformations like precipitate growth or dissolution are solved as a part of the moving boundary problem. A planar boundary separates the two single phase regions and the phase boundary migration is controlled by the rate of diffusion to and from the interface. In the case of the growth of the grain boundary $M_{23}C_6$ responsible for chromium depletion adjacent to the grain boundaries, the precipitates are expected to form at certain nucleation sites on the grain boundaries and to grow with the help of both matrix and grain boundary diffusion into one or both the grains as shown in Fig. 10 [111], [112]. The grain boundaries can operate as collector plates for the substitutional atoms diffusing through the matrix to the grain boundaries [113] as the mobility of the substitutional alloying elements along the grain boundaries is much higher than that through the austenite matrix [114], [115]. Low concentration gradients are required in the boundary plane to transport the substitutional atomic flux arriving from the austenite matrix due to the high mobility along the grain boundaries. This makes it reasonable to assume that the concentration profile perpendicular to a grain boundary is constant along the boundary. It was assumed that the $M_{23}C_6$ carbide growth is diffusion controlled and the chromium concentration profile perpendicular to the grain boundary should be similar to that

encountered in the case of a $M_{23}C_6$ precipitate film covering the boundary as shown in Fig. 10(b). Therefore, the growth can be modelled one dimensionally and is the approach used in this work for estimating the chromium concentration profiles. Grain boundary diffusion of chromium should decrease the incubation time for $M_{23}C_6$ at higher temperatures and thus it is assumed that the grain boundary nucleation of $M_{23}C_6$ starts immediately after reaching the isothermal temperatures in Paper II, where DOS is measured at higher temperatures (700–820 °C). However, in Papers III and V, the heat treatments are done at lower temperatures like 550 °C and so incubation times are included before the growth of the carbides. The simulations were performed using the MOBFE2 mobility database and the TCFE7 thermodynamic database. Multicomponent effects of carbon, chromium, nickel, silicon and iron are considered in the simulations. The determination of the operating tie line is quite challenging as there are an infinite number of possible tie-lines governing the growth of the carbide.

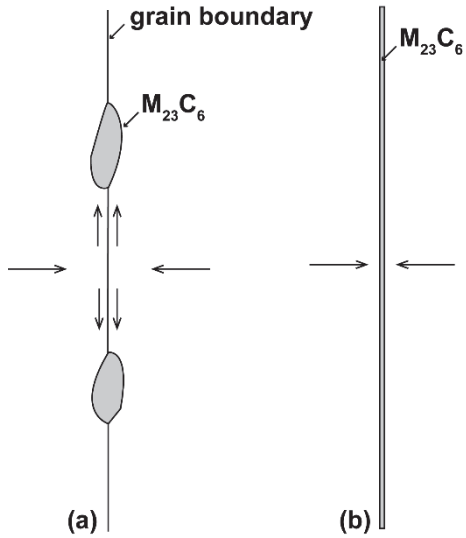

Fig. 10. (a) $M_{23}C_6$ precipitates on a grain boundary. The arrows show the diffusion flux of chromium towards and along the grain boundary (b) one dimensional representation of grain boundary precipitation assumed in the modelling (Reprinted by permission from Paper II © 2019 ISIJ).

The following iterative method is used to determine the composition on either side of the carbide - austenite interface. The interfacial velocity $v^{p/\gamma}$ (where p is the carbide precipitate and γ is the austenite phase), activities and the conditions of

local equilibrium at the interface are initially estimated. This gives the interfacial concentrations that can be used as boundary conditions. It is then checked if the flux balances at the interface are satisfied i.e. whether the rates of consumption of various elements k at the advancing interface are delivered to or removed from the interface by the diffusion flux. In other words, the flux balances are satisfied when

$$v^{p/\gamma}\left(c_p^k - c_k^\gamma\right) = J_k^p - J_k^\gamma, \tag{16}$$

where J_k^p, J_k^γ are the fluxes of component k at the $M_{23}C_6$ carbide - austenite interface during the current time step and c_p^k and c_k^γ are the concentrations of element k on either side of the interface in the austenite and $M_{23}C_6$ carbide respectively. New interfacial velocities and activities are tried when the flux balance equations are not satisfied until the conditions are met, i.e. the operative tie-line is found. This procedure is repeated for all the time steps [116]. It is necessary to take the effect of the soft impingement of the precipitates on different grain boundaries while defining the modelling conditions. Soft impingement is the overlap of the diffusion fields of different precipitates on each other and also on the grain boundaries during precipitate growth. In the one-dimensional model, this can be addressed by choosing an appropriate austenite width from which carbon can be withdrawn (d_a) as shown in Fig. 11 where d_p is the half-thickness of the $M_{23}C_6$ film.

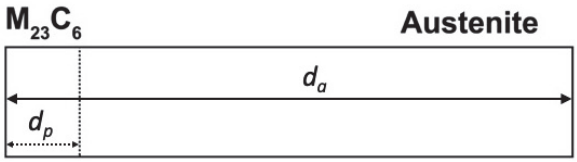

Fig. 11. Treatment of numerical simulation across the carbide-austenite interface (Under CC BY license from Paper IV © 2019 Authors).

Sourmail et al. [90] assumed d_a is one sixth of the grain size. This assumes that grains are simple cubes and that each of the six faces of the cube draws equal amount of carbon from the same grain. It is therefore appropriate to attribute a sixth of grain diameter to each one-dimensional calculation volume. In all the five papers in this thesis, one-sixth of the average grain size is considered to be d_a. The results of simulations made using different ratios between d_a and the grain size are given in the discussion section.

3.3.3 TC - Prisma

TC-Prisma is an add-on module to the Thermo-Calc software [117]. It is a computational tool for simulating the kinetics of concurrent nucleation, growth and coarsening and is based on the Langer-Schwartz theory that adopts the Kampmann-Wagner numerical method [118], [119]. In this work, TC-Prisma is used to estimate the nucleation times for the formation of grain boundary $M_{23}C_6$ carbides at different isothermal temperatures. Mobilities, driving forces and interfacial energies are the vital parameters that are needed for the simulation. The TCFE7 thermodynamic database and the MOBFE2 kinetic database are used for obtaining the required parameters for the simulations. For estimating the interfacial energies, a modified Becker's model is used [120]–[122]. It predicts the values to be around 0.1–0.2 J/m^2, which is in the range reported in the literature [123], [124]. The molar volumes required for the simulations are calculated based on the work by Qiu and Frisk [125], [126]. The time dependent nucleation rate $J(t)$ is obtained by the extension of classical nucleation theory (CNT) for modelling nucleation in multicomponent alloy systems [127]. The incubation time for precipitation (τ) for an isothermal reaction is given by [128]

$$\tau = \frac{1}{2Z^2\beta^*}, \tag{17}$$

where Z (Zeldovich factor) is a measure of the probability that super-critical nucleus dissolves in the matrix by crossing back over the free energy barrier, and is given by

$$Z = \frac{V_m^\beta}{2\pi N_A r^{*2}} \sqrt{\frac{\sigma}{kt}}. \tag{18}$$

β^* in Eq. (17) is the rate at which atoms or molecules are attached to the critical nucleus, and it is given by

$$\beta^* = \frac{4\pi r^{*2}}{a^4} \left[\sum_{i=1}^{k} \frac{\left(X_i^{\beta/\alpha} - X_i^{\alpha/\beta}\right)^2}{X_i^{\alpha/\beta} D_i} \right]^{-1}. \tag{19}$$

In Eqs. (18) and (19), a is the lattice parameter, N_A is the Avogadro number, k denotes the number of components, $X_i^{\beta/\alpha}$ and $X_i^{\alpha/\beta}$ are the mole fractions of element i at the interface in the precipitate and matrix respectively, D_i is the corresponding diffusion coefficient in the matrix. The critical nucleus radius r^* in Eq. (18) is given by

$$r^* = \frac{2\sigma V_m^\beta}{\Delta G_m^{\alpha\to\beta}} \ , \tag{20}$$

where V_m^β is the molar volume of the matrix phase and ΔG^* is the Gibbs energy of formation of the critical nucleus and is given by

$$\Delta G^* = \frac{16\pi\sigma^3}{3\left(\Delta G_m^{\alpha\to\beta}/V_m^\beta\right)^2} . \tag{21}$$

4 Results

4.1 Degree of sensitization

For the alloy EN 1.4310, the variation of experimentally measured DOS with peak temperature for different cooling rates can be seen in Fig. 12(a) (Paper I). For all the cooling rates (0.125 °C/s, 2 °C/s, 32 °C/s) the DOS first increases with increasing peak temperature up to 900 °C after which it starts decreasing. The slowest cooling rate of 0.125 °C/s induced the greatest sensitization due to the longer time spent in the sensitization temperature regime. The peak temperature of 900 °C produced the highest DOS values for all the cooling rates. The samples that are cooled at 32 °C/s from 800 and 900 °C are slightly sensitized and the samples that are cooled at 32 °C/s from 700 and 1000 °C unsensitized. The DOS values for the peak temperature of 1000 °C are obtained from the DL-EPR curves in Fig. 12(b).

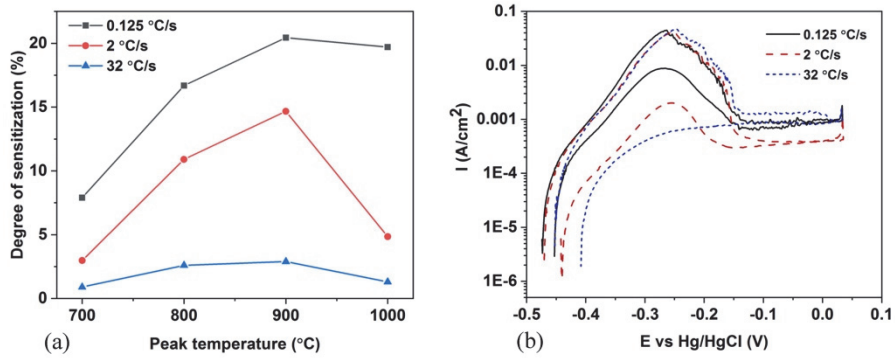

Fig. 12. (a) Variation of DOS with peak temperature for different cooling rates. (b) DL-EPR curves for different cooling rates from peak temperature of 1000 °C (Reprinted [adapted] by permission from Paper I © 2017 Associazione Italiana di Metallurgia).

For the isothermal studies (Paper II), Fig. 13(a) shows the values of DOS obtained from the DL-EPR tests that are plotted against time at various holding temperatures for the EN 1.4310 alloy. The data points are average values of three measurements, which differ from each other by less than 1% on the DOS scale. It is evident that for all the holding temperatures, the level of DOS rises at an ever-decreasing rate showing signs of saturations towards long heat treatment times. 760 °C is the temperature where the DOS is observed to be the highest. This implies that the precipitation kinetics of $M_{23}C_6$ and consequent chromium depletion are fastest at

760 °C, while at 700 °C, the kinetics are slower due to the lower diffusion and at 820 °C, due to a lower driving force.

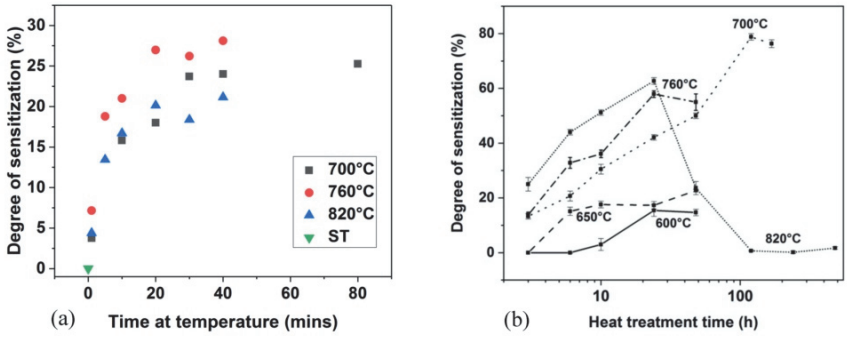

Fig. 13. Degree of sensitization values from DL-EPR tests for isothermal treatments to study (a) the development of sensitization at 700, 760 and 820 °C, (b) sensitization and self-healing at 600, 650, 700, 760 and 820 °C. In (a) ST means solution treated and quenched without subsequent heat treatment (DOS = 0) (Reprinted by permission from Paper II and III © 2019 ISIJ).

In Paper III, the isothermal heat treatments are extended to longer time periods and more temperatures. Fig. 13(b) shows the experimentally determined DOS values as a function of holding temperature and time. The tests were repeated three times and the observed standard deviations are shown as error bars. At all the temperatures, the DOS increased with an increase in holding time. At the high temperatures 700, 760 and 820 °C, within the studied time periods, the DOS starts to drop after reaching a peak owing to the start of self-healing. The self-healing began after 24 h at 760 and 820 °C while it started after 120 h at 700 °C. The maximum heating time employed in the study is not enough to observe the self-healing at 600 and 650 °C. It is clear, that the kinetics of sensitization and self-healing are faster at higher temperatures. These results were in very good agreement with the oxalic acid etching test results as can be seen from Fig. 14. The sample heat treated at 600 °C for 10 h shows step structure in Fig. 14(a) and 14(b) indicating the sample is almost free from intergranular corrosion susceptibility. Fig. 14(c) and 14(d) show a ditch structure for the sample heat treated at 700 °C for 120 h. In the case of the sample heat treated at 820 °C for 120 h, the carbides are etched along the grain boundaries. Despite the fact that the sample condition is self-healed as seen from

the DL-EPR test results, the carbides at the grain boundaries are etched noticeably due to the etching with oxalic acid.

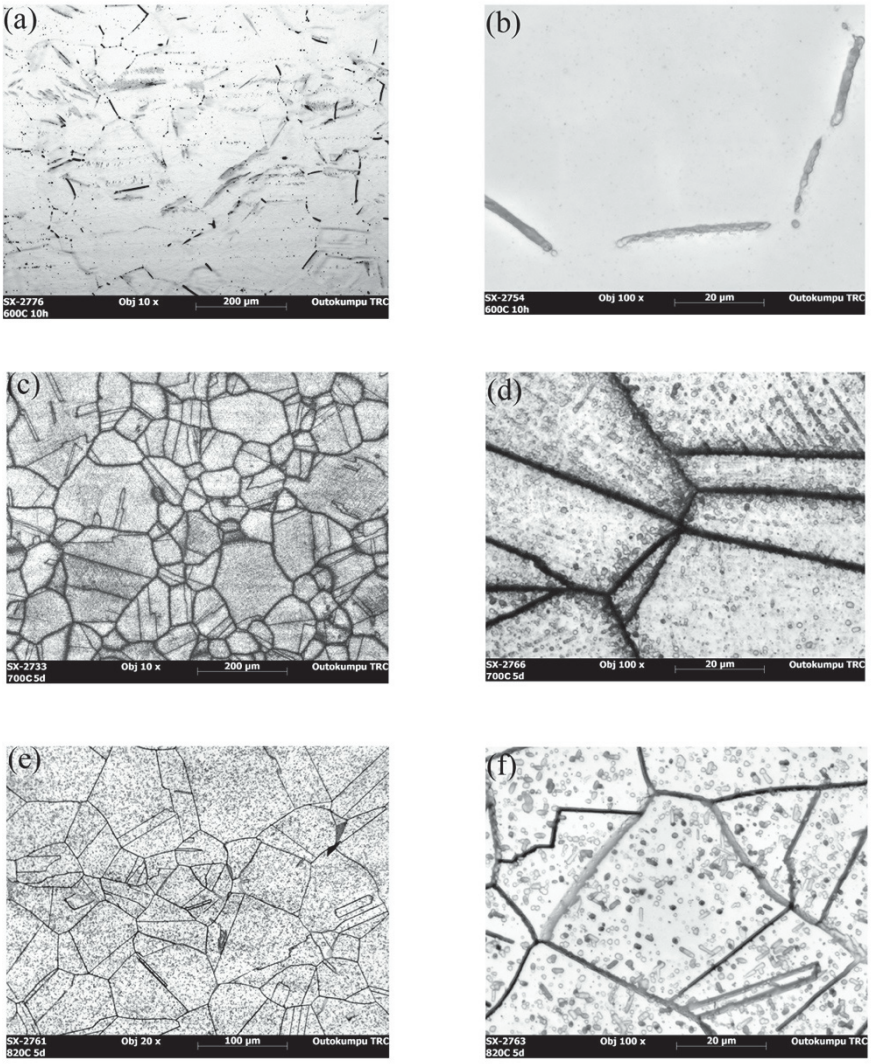

Fig. 14. Oxalic acid etching microstructures (a,b) for the samples heat treated at 600 °C for 10 h at 20 X & 100 X; (c,d) 700 °C for 120 h at 10 X & 100 X; (e,f) 820 °C for 120 h at 20 X & 100 X respectively (Reprinted by permission from Paper III © 2019 ISIJ).

The heat treatment conditions employed in Paper IV for generating different grain sizes resulted in decarburization the samples. The heat treatments employed, amount of that was realized using GDOES and the average ECD is shown in Table 6. The DOS is normalized with respect to the smallest grain size i.e., 72 µm and the NDOS of samples with different grain sizes after heat treatment at 820 °C can be seen in Fig. 15. An increase in grain size leads to a lower NDOS during the sensitization and self-healing phases. The sample with a grain size 72 µm was highly sensitized as is apparent from the peak NDOS achieved. Due to the partial decarburization that occurred during the long heat treatments at the high temperature needed to obtain the large grain sizes, the carbon content is lower in the large-grained samples and hence less carbon is available for $M_{23}C_6$ precipitation, giving rise to lower peak NDOS values. Another factor contributing to the lower NDOS of the large-grained samples is the drop in the nose temperature in temperature-time-sensitization diagram caused by a decrease in carbon content. The effect of grain size itself on the NDOS will be discussed later. The time to reach peak NDOS is reduced with an increase in grain size from 72 to 190 µm and a concomitant decrease in carbon content from 0.105 to 0.073% by wt.

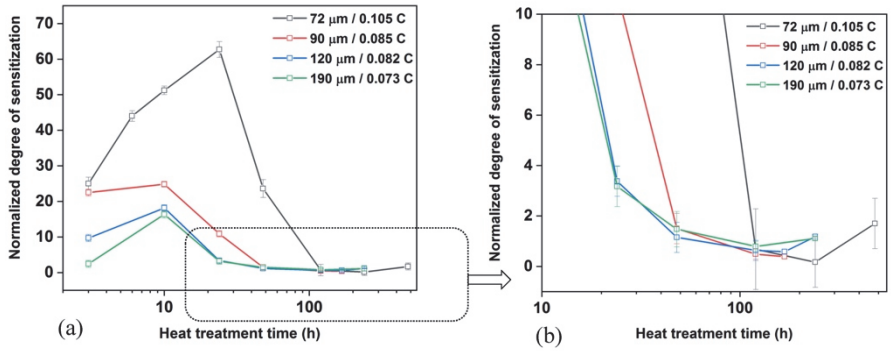

Fig. 15. Normalized degree of sensitization (NDOS) with heat treatment time at 820 °C. (a) all the results (b) results beyond 20 h on an expanded scale. Means and standard deviations are shown by points and error bars (Reprinted [adapted] under CC BY license from Paper IV © 2019 Authors).

The NDOS values for all the heat treatments and alloy grades considered and mentioned in Table 7 for Paper V are shown in Fig. 16. For the heat treatment conditions considered, the NDOS values are highest for grade 1.4310. The measured NDOS values are the lowest of all the grades studied in the case of grades

1.4307 and 1.4318 due to their low carbon contents: even after 20 days of heat treatment at 700 °C, no sensitization was observed. For the heat treatment times considered, both sensitization and self-healing was only observed in the case of grade 1.4310 at 820 °C. The suffixes HiC, HiCr and LC indicate high carbon, high chromium and low carbon contents respectively in the alloys.

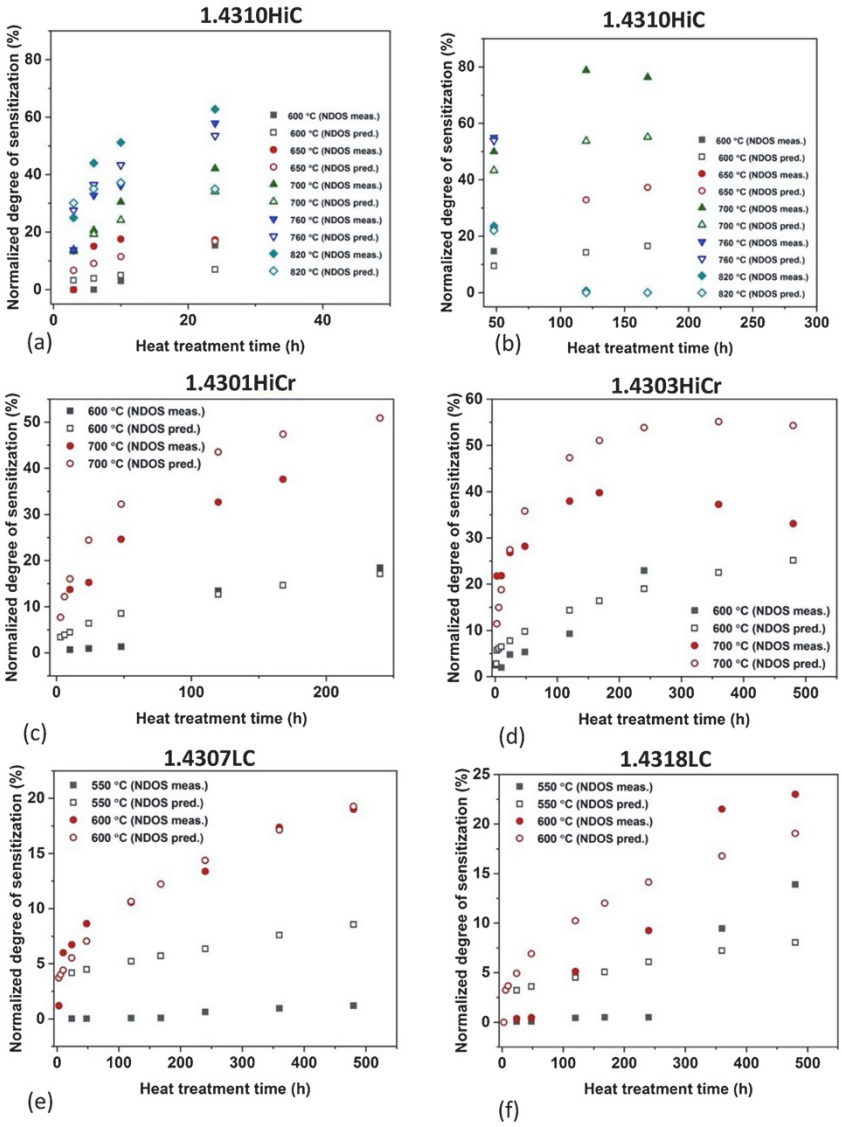

Fig. 16. NDOS values of all the sample conditions (measured from DL-EPR tests and predicted using the model discussed in later sections) Filled symbols are measured values and open symbols are predicted. Note scale changes between grades (Under CC BY-NC-ND license from Paper V © 2020 Authors).

4.2 Precipitation and chromium depletion

Fig. 17 shows STEM micrograph of precipitates on grain boundaries, corresponding EDS mappings, and elemental concentrations for the ST EN 1.4310 sample with an average grain size 72 μm that was heat treated at 700 °C for 120 h. EDS spot analyses and SAD pattern analysis confirmed that the precipitates are $M_{23}C_6$ carbides, see Fig. 18. In this heat-treated condition, $M_{23}C_6$ carbides were detected both on the grain boundaries and inside the grains. The DL-EPR measurements show that the sample condition is sensitized (NDOS = 76) and the chromium concentration profiles in Fig. 17(e) for the red line in Fig. 17(b) show that the chromium concentration adjacent to the interface has dropped below the critical level of 12% by wt. However, the Cr concentration did not fall below the critical level in the vicinity of the intragranular $M_{23}C_6$, see Fig. 17(f). The inclination of the carbide-austenite interface with respect to the electron beam does not allow for the measurement of the chromium concentration right at the interface.

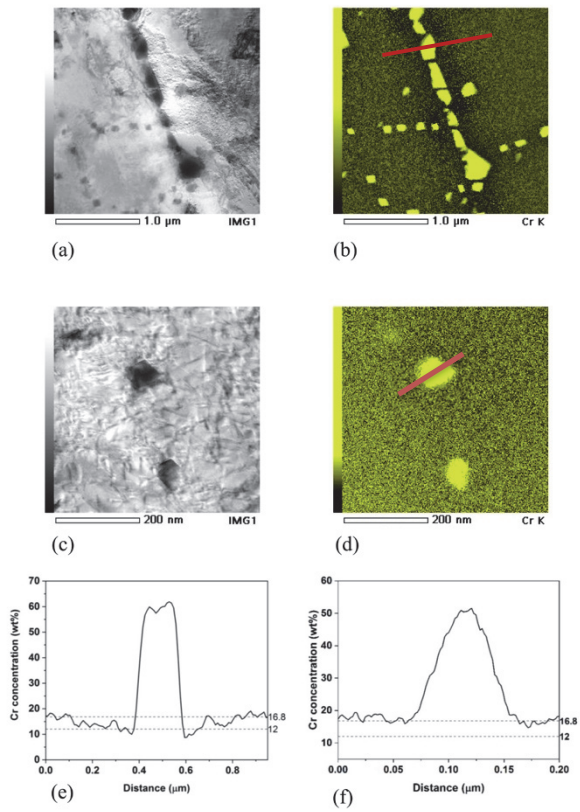

Fig. 17. Sample EN 1.4310, grain size 72 µm, heat treated at 700 °C for 120 h. Bright field transmission electron microscope (TEM) micrograph showing (a) grain boundary $M_{23}C_6$, (c) intragranular $M_{23}C_6$, (b,d) EDS mapping of Cr in (a,c) respectively, and (e,f) chromium concentration profiles along red lines in (b,d) respectively (Under CC BY-NC-ND license from Paper V © 2020 Authors).

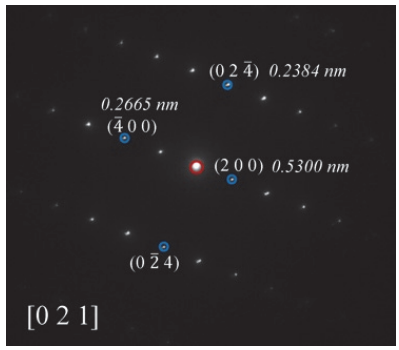

Fig. 18. SAD pattern of the precipitate in Fig. 17 confirming it to be $M_{23}C_6$.

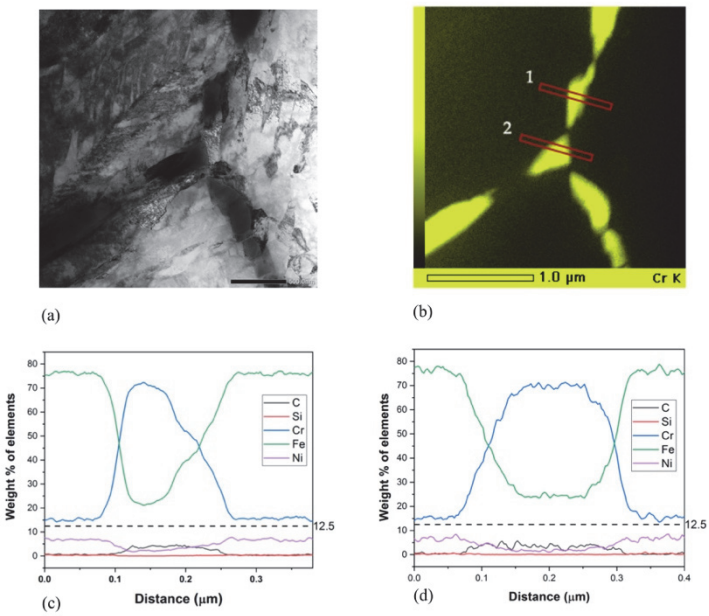

Fig. 19. Sample EN 1.4310, grain size 72 µm, heat treated at 820 °C for 120 h (a) Bright field transmission electron microscope (TEM) micrograph showing $M_{23}C_6$ carbides along a grain boundary (b) EDS mapping of Cr (c and d) chromium concentration profiles along lines 1 and 2 in the Cr EDS map (Reprinted [adapted] under CC BY license from Paper IV © 2019 Authors).

Fig. 19 shows details of the self-healed sample EN 1.4310 ST - 820 °C - 120 h having NDOS = 0.45, as seen with TEM. The EDS mappings of Cr indicate the

presence of grain boundary $M_{23}C_6$, and the Cr concentration profiles clearly indicate that the chromium concentration in the vicinity of the precipitates did not fall below the critical 12 % by wt. Similar observations were made for the sample conditions EN 1.4310 120 µm - 820 °C - 168 h and 190 µm - 820 °C - 240 h that were also self-healed: the results of TEM studies with EDS mappings and Cr concentration profiles are presented in Fig. 20.

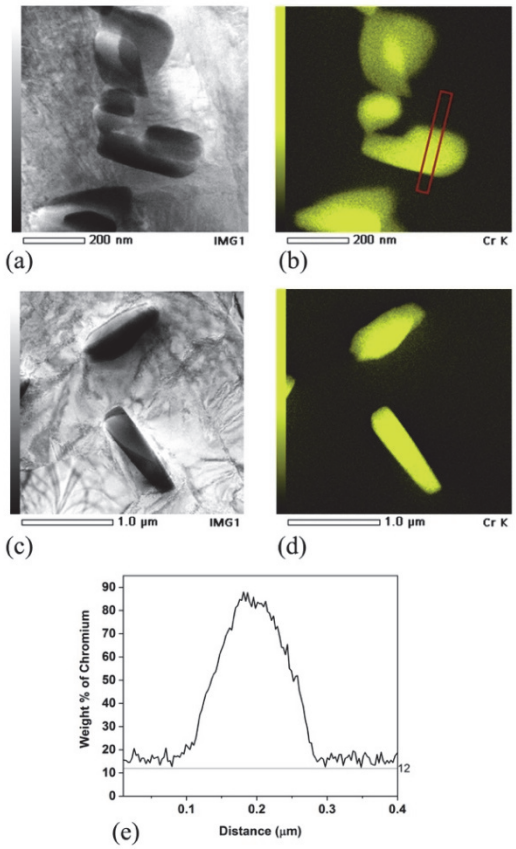

Fig. 20. (a,c) Bright field TEM micrograph of 120 µm - 820 °C-168 h and 190 µm - 820 °C-240 h respectively showing intragranular $M_{23}C_6$ carbides. (b,d) EDS mapping of Cr for the micrographs (a) (c) respectively, (e) Cr concentration profile along the red line shown in (b) (Reprinted [adapted] under CC BY license from Paper IV © 2019 Authors).

In the sample condition EN 1.4310 190 µm - 820 °C - 240 h, Cr_2N precipitates were observed, in Fig. 21. The SAD pattern observed in Fig. 21(b) confirmed the precipitate to be Cr_2N with hexagonal crystal structure. However, Cr_2N precipitate did not cause chromium depletion below the critical chromium value along the interface (Fig. 21(c)).

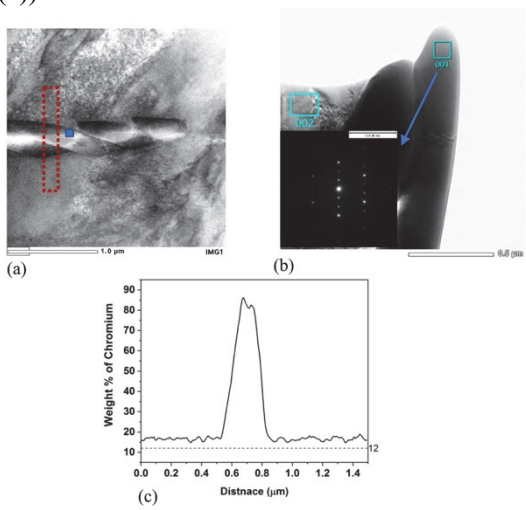

Fig. 21. Sample 190 µm - 820 °C-240 h (a) STEM micrograph, (b) SAD pattern showing the precipitate to be Cr_2N and (c) Cr concentration profile along the red line shown in (a) (Reprinted [adapted] under CC BY license from Paper IV © 2019 Authors).

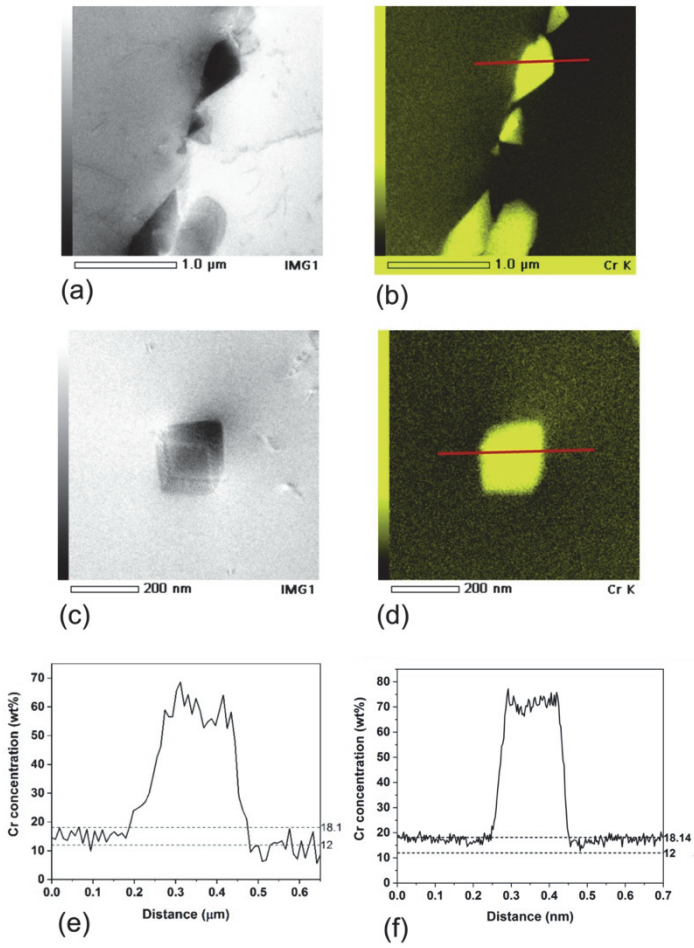

Fig. 22. (a,c) STEM micrographs (b,d) EDS mappings of Cr and (e,f) Cr concentration profiles along the red lines in (b,d) respectively for the sample condition 1.4303 - 700 °C - 360 h (Under CC BY-NC-ND license from Paper V © 2020 Authors).

In the grade 1.4303 that was heat treated at 700 °C for 360 h, both intergranular and intragranular $M_{23}C_6$ was found. Fig. 22(b) and 22(d) show EDS mappings of the respective carbides. Similarly to the previous observations, chromium was depleted below 12% by wt. in the vicinity of grain boundary carbides, while chromium was not depleted below the critical level in the vicinity of intragranular carbides, Fig. 22 (e) and 22(f) respectively.

4.3 Nucleation kinetics

Fig. 23(a) shows a phase diagram EN 1.4310 calculated using Thermo-Calc. In the sensitization regime, both $M_{23}C_6$ and Cr_2N carbides are predicted to be stable at equilibrium. The property diagram in Fig. 23(b) indicates the equilibrium number of moles of the precipitate phases in 100 g of alloy as a function of temperature. These equilibrium phases are observed in the STEM micrographs of specimens heat treated for long times as shown in Fig. 17–22.

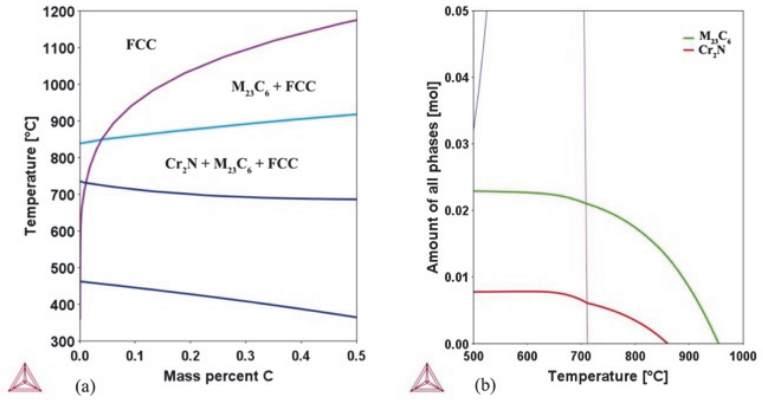

Fig. 23. (a) Phase diagram showing the equilibrium phases in the experimental composition Fe-16.80Cr-6.36Ni-(0 - 0.5) C-0.065N (in wt.%) (b) property diagram showing the number of mols of the phases in 100 g of alloy for the composition Fe-16.80Cr-6.36Ni-0.1C-0.065N (EN 1.4310) (Reprinted [adapted] under CC BY license from Paper IV © 2019 Authors).

The effect of chromium and nickel on the carbon solubility and thereby solvus line for the $M_{23}C_6$ can be seen in Fig. 24. It is apparent that an increase in either chromium or nickel content decreases the carbon solubility thus providing more driving force for the precipitation of chromium carbides.

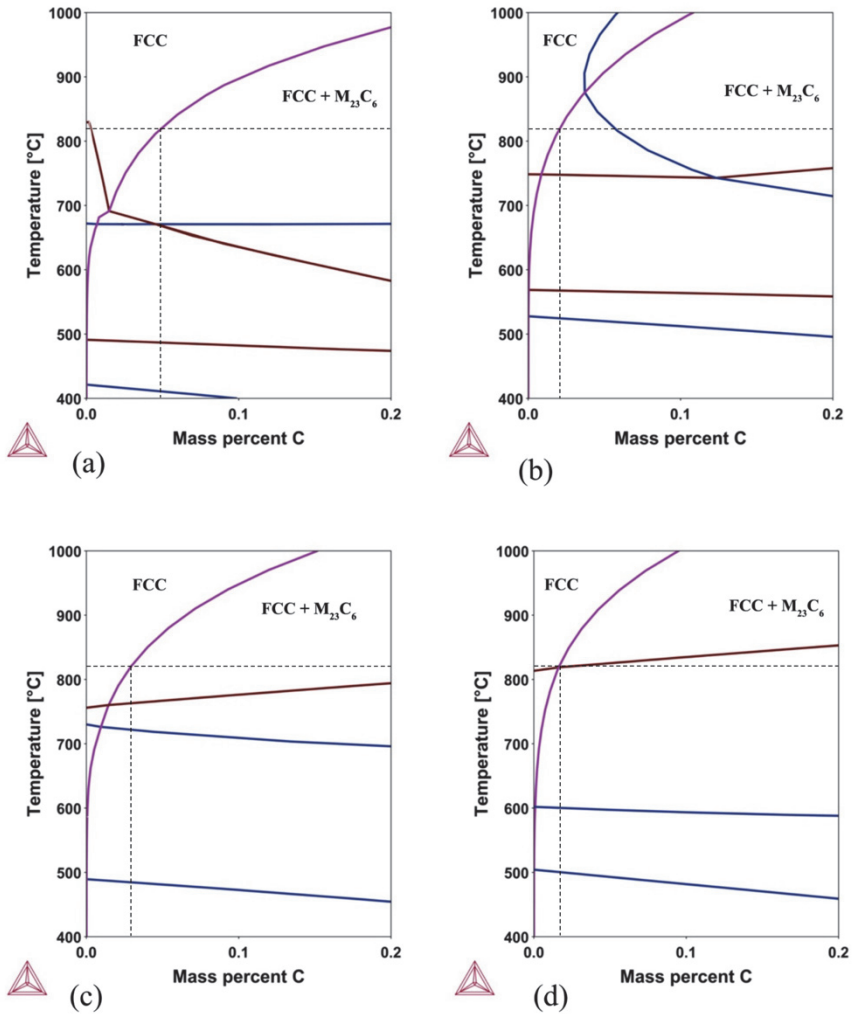

Fig. 24. Phase diagrams predicted by Thermo-Calc showing the effect of chromium and nickel on the solubility of carbon in austenite. Compositions in wt.%: (a) 12 Cr - 6.53 Ni - 0.95 Si, (b) 20 Cr - 6.53 Ni - 0.95 Si, (c) 16.80 Cr - 4 Ni - 0.95 Si (d) 16.80 Cr - 15 Ni - 0.95 Si. Comparing (a) and (b) shows the effect of Cr, while (c) and (d) show the effect of Ni. C, Cr and Ni vary around the composition of alloy 1.4310, i.e. 0.10 C - 16.80 Cr - 6.53 Ni - 0.95 Si (Under CC BY-NC-ND license from Paper V © 2020 Authors).

For the heat treatments of the 1.4310 alloy considered in Paper I, TC-Prisma simulations predicted that $M_{23}C_6$ is not nucleated along the grain boundaries during

the heating at 50 °C/s to the hold temperatures. The heating stage was thus ignored by starting the simulations after reaching the peak temperatures. However, $M_{23}C_6$ carbide was considered as an inactive phase at the start of simulation. Once a phase is predefined as an inactive phase, the driving force for the precipitation of the phase is continuously monitored and when it surpasses a predefined positive value, the phase automatically becomes active. It could be seen from the Thermo-Calc calculations that the $M_{23}C_6$ carbide is stable in the austenite matrix below 960 °C. The nucleation times were neglected in the simulations in Papers I and II but included in Papers III–V. Table 8 presents the times for nucleation as measured from the start of holding as calculated for the heat treatment conditions considered in Paper III.

Table 8. Nucleation times for the formation of $M_{23}C_6$ precipitates on grain boundaries in the 1.4310 alloy studied in Paper III (Reprinted by permission from Paper III © 2019 ISIJ).

Holding temperature (°C)	Incubation time (s)
600	4690
650	740
700	152
760	32
820	10

As expected, the nucleation times increase with decreasing temperature: nucleation is almost instantaneous at 820 °C but very slow at 600 °C. In a similar fashion, higher nucleation times for the grain boundary carbide precipitation (for different alloys considered in Paper V) were observed for lower temperatures, as presented in Table 9.

Table 9. Calculated nucleation times in seconds from the start of holding for the formation of grain boundary $M_{23}C_6$ in the alloys studied in Paper V (Under CC BY-NC-ND license from Paper V © 2020 Authors).

Alloy	% C (wt.)	Nucleation times (s)			
		550 °C	600 °C	700 °C	820 °C
1.4310HiC	0.10	-	4690	152	10
1.4301HiCr	0.04	-	4825	195	26
1.4303HiCr	0.04	-	3933	161	21
1.4307LC	0.02	58833	8418	556	0
1.4318LC	0.02	85108	13032	1305	0

4.4 Grain boundary precipitate growth and Cr depletion

The grain boundary chromium concentration profiles predicted using DICTRA for cooling from 1000 °C, as considered in Paper I, are shown in Fig. 25. In this work, depletion is characterised by the average weight percentage of chromium in the 25 nm thick layer (a_{25nm}) in the austenite adjacent to the interface. The measured a_{25nm} values are given in the Fig. 25 and is evident that the slow cooling rates caused higher chromium depletion indicated by low a_{25nm} values. The experimentally measured DOS values were used to determine how DOS depends on a_{25nm}. Calculated values of a_{25nm} were then used to construct the continuous cooling sensitization (CCS) diagram in Fig. 26. The approach served as a starting tool in predicting the CCS diagrams and identifying the cooling paths that are expected to deteriorate the microstructure and cause sensitization.

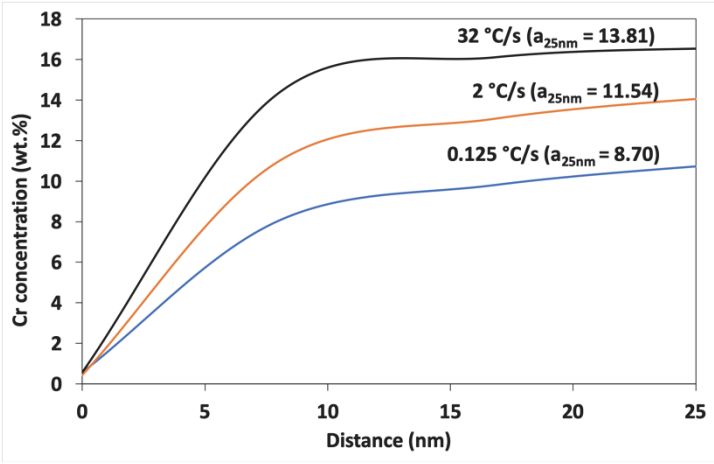

Fig. 25. DICTRA simulations for the EN 1.4310 composition showing Cr concentration profiles from the interface between $M_{23}C_6$ and austenite and into the austenite matrix after continuous cooling from 1000 °C to 400 °C with a cooling rate of (a) 0.125 °C/s (b) 2 °C/s (c) 32 °C/s. Total cell length (not shown) is 12 µm, which is one-sixth of the average grain size (Reprinted [adapted] by permission from Paper I © 2017 Associazione Italiana di Metallurgia).

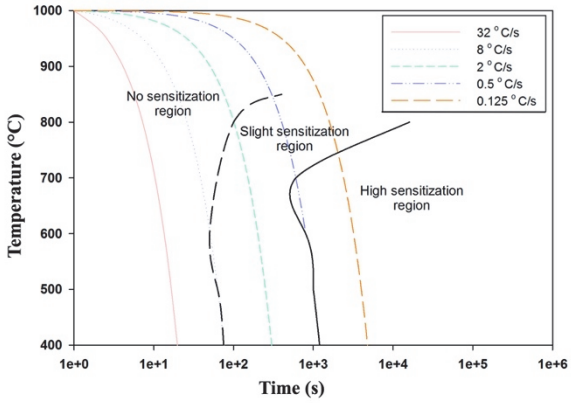

Fig. 26. Continuous cooling sensitization diagram obtained from DICTRA simulations for the EN 1.4310 composition (Reprinted by permission from Paper I © 2017 Associazione Italiana di Metallurgia).

The predicted chromium concentration profiles for the EN 1.4310 sample conditions treated in Paper II can be seen in Fig. 27. The corresponding concentration profiles for C, Ni, and Si are given in Fig. 28 - 30. In all cases, only the part of the one-dimensional cell close to the interface is shown, the total cell length being one sixth of the grain size, i.e. 12 µm.

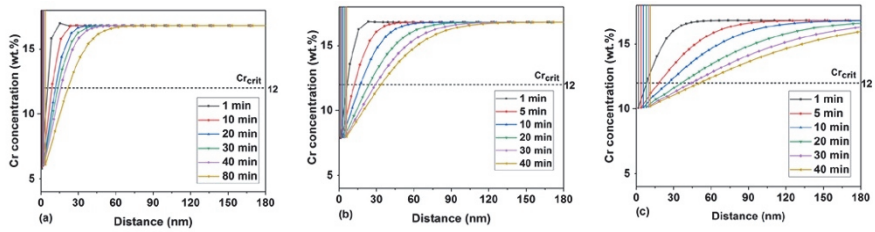

Fig. 27. Cr concentration profiles as a function of distance in the one-dimensional calculation cell and holding time at (a) 700 °C (b) 760 °C (c) 820 °C. Total cell length of 12 μm (Reprinted by permission from Paper II © 2019 ISIJ).

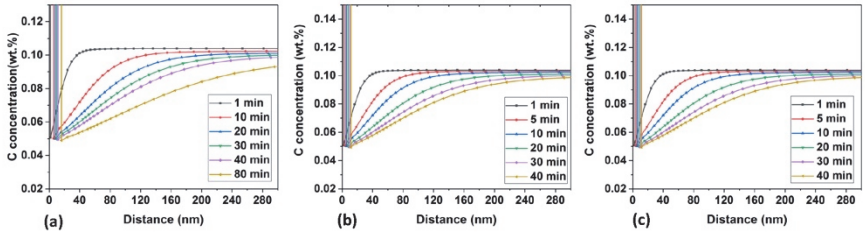

Fig. 28. C concentration profiles as a function of distance in the one-dimensional calculation cell and holding time at (a) 700 °C (b) 760 °C (c) 820 °C. Total cell length 12 μm. Note scale changes in comparison to Fig. 27 (Reprinted by permission from Paper II © 2019 ISIJ).

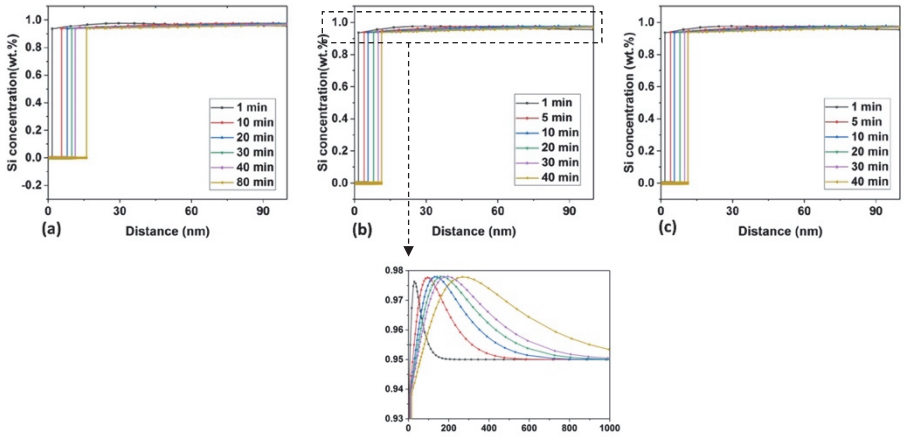

Fig. 29. Si concentration profiles as a function of distance in the one-dimensional calculation cell and holding time (a) 700 °C (b) 760 °C (c) 820 °C. Total cell length 12 μm. Note scale changes in comparison to Fig. 27 (Reprinted [adapted] by permission from Paper II © 2019 ISIJ).

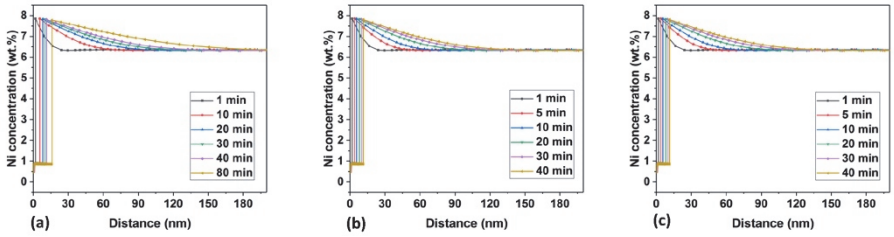

Fig. 30. Ni concentration profiles as a function of distance in the one-dimensional calculation cell and holding time at (a) 700 °C (b) 760 °C (c) 820 °C. Total cell length 12 μm. Scale same as in Fig. 27 (Reprinted by permission from Paper II © 2019 ISIJ).

In Paper II, it was assumed that the grain boundary precipitates nucleated and started growing from the beginning of the hold (time = 0). This ignoring of nucleation times and the error incurred due to it was shown in Paper III and will be discussed later. In Papers III and V, the time for nucleation was taken into account by starting the growth calculations after the calculated nucleation time for $M_{23}C_6$ precipitation. The nucleation times are given in Tables 8 and 9 and calculated chromium concentration profiles are presented in Fig. 31 (Paper III). Now that much longer times are involved than in Paper II, the variation of Cr_{int} and W_{crit} with time and temperature is more clearly visible.

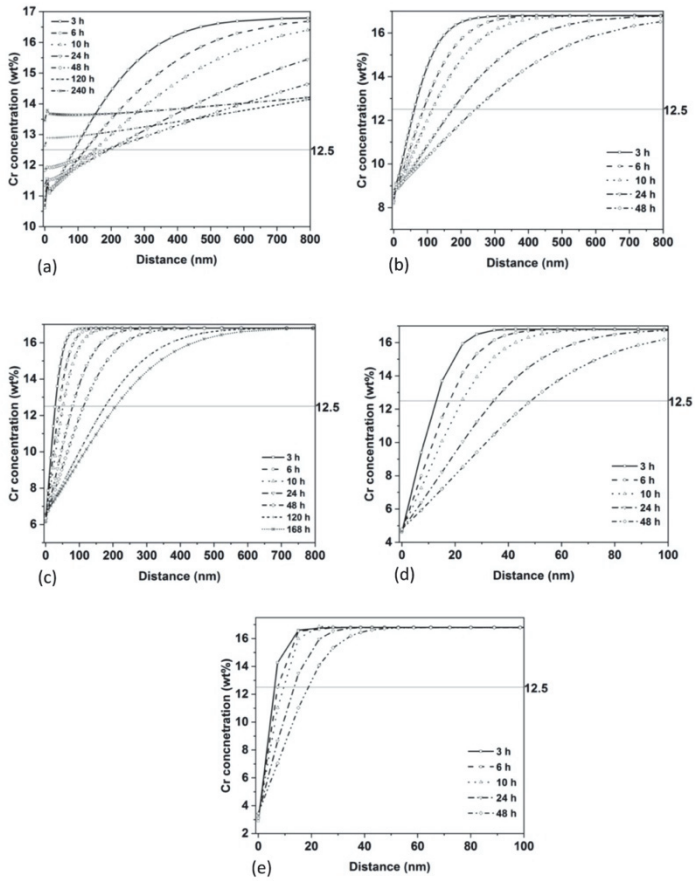

Fig. 31. Chromium concentration profiles as a function of distance from the $M_{23}C_6$ - austenite interface at (a) 820 °C (b) 760 °C (c) 700 °C (d) 650 °C and (e) 600 °C for the 1.4310 alloy considered in Paper III (Reprinted by permission from Paper III © 2019 ISIJ).

The diffusion simulations for the 1.4310 alloy with various grain sizes and carbon contents treated in Paper IV give the concentration profiles shown in Fig. 32. The considered critical chromium concentration, i.e. 12.5% by wt. is indicated in the figure.

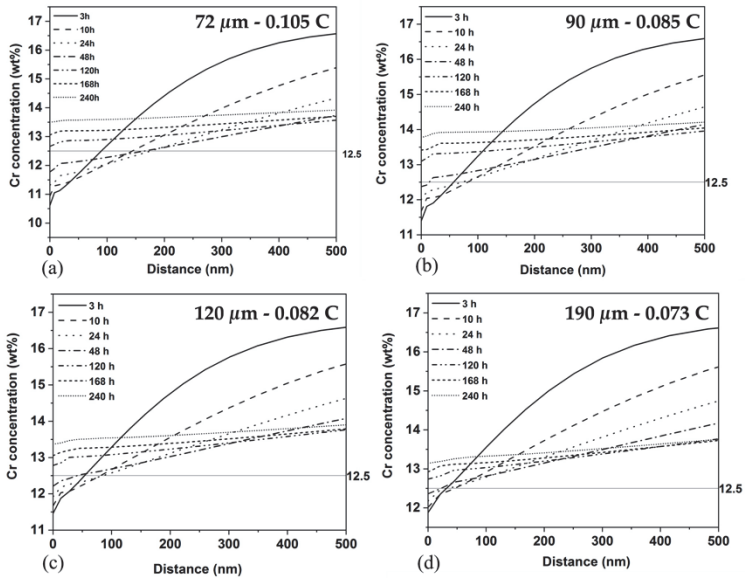

Fig. 32. Chromium concentration profiles in the austenite away from the $M_{23}C_6$ carbide - matrix interface as a function of sensitization time at 820 °C for the following grain sizes and overall carbon concentrations (a) 72 μm and 0.105 C (wt.%), (b) 90 μm and 0.085 C (wt.%), (c) 120 μm and 0.082 C (wt.%), and (d) 190 μm and 0.073 C (wt.%) (Reprinted [adapted] under CC BY license from Paper IV © 2019 Authors).

As mentioned in the above results, similar predicted chromium concentration profiles are shown in Fig. 33 for all the steel grades 1.4310, 1.4301, 1.4303, 1.4307 and 1.4318 subjected to different isothermal aging treatments. The chromium depletion regions are narrow in the grades 1.4307 and 1.4318 relative to the other grades.

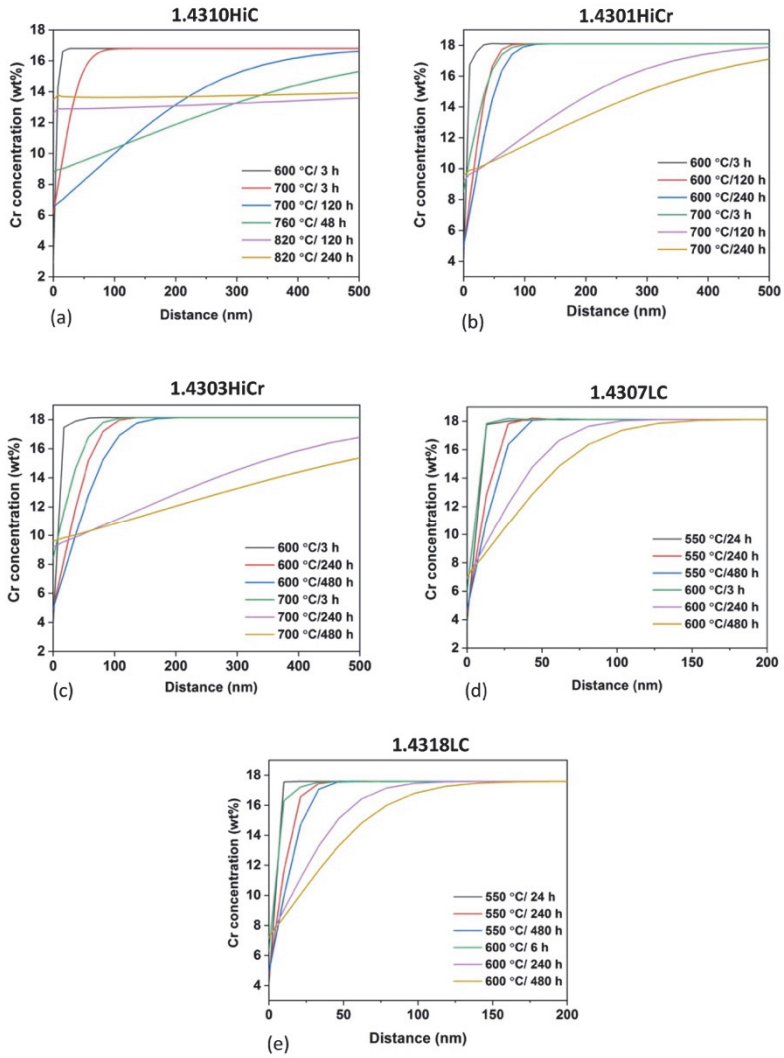

Fig. 33. Cr concentration profiles away from the grain boundary $M_{23}C_6$ - austenite matrix interface for the a) 1.4310, b) 1.4301, c) 1.4303, d) 1.4307 and e) 1.4318 alloy compositions studied. Note that distance scales vary (Under CC BY-NC-ND license from Paper V © 2020 Authors).

5 Discussion

5.1 Relationship between Cr depletion profile and degree of sensitization

The calculated Cr concentration profiles away from the $M_{23}C_6$ - austenite interface at the end of the isothermal treatments should be of the form shown schematically in Fig. 34. Following Yin et al. [129], Cr_{int} is the chromium concentration in the austenite at the interface, Cr_{crit} is the critical chromium concentration that determines the effective width (W_{crit}) of the chromium depleted zone at the grain boundary. This interfacial chromium concentration Cr_{int} value, is a result of the local equilibrium condition assumed to exist at the mobile model interface and depends on the isothermal holding temperature and changes with holding time as illustrated in Fig. 34(a).

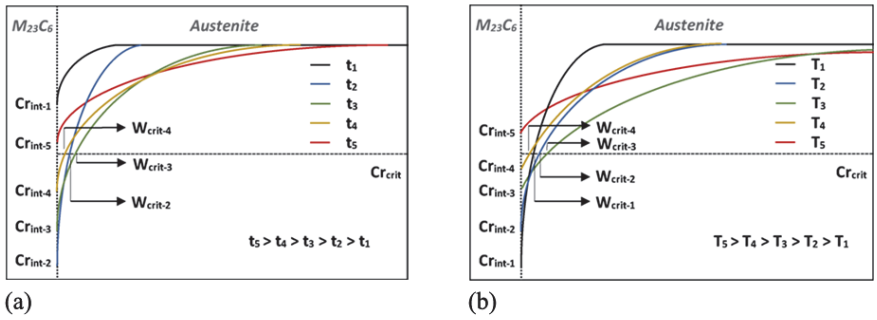

Fig. 34. Schematic of chromium concentration profiles in the austenite ahead of $M_{23}C_6$ boundary film at the end of isothermal holding for a) different holding times $t_5 > t_4 > t_3 > t_2 > t_1$, b) different holding temperatures $T_5 > T_4 > T_3 > T_2 > T_1$.

The approach served as a starting tool in predicting the CCS diagrams and thus identifying the cooling paths that deteriorate the microstructure through sensitization.

For isothermal heat treatment conditions, as is shown in Fig. 34(a), Cr_{int} initially decreases with time from Cr_{int-1} to Cr_{int-2} till it reaches the minimum value. With further increase in time, Cr_{int} rises through Cr_{int-3} to Cr_{int-4}. When Cr_{int} rises above Cr_{crit} (during the time period between Cr_{int-4} to Cr_{int-5}), the material should become completely self-healed. The critical width W_{crit} initially increases with

isothermal holding time and then decreases at longer times when the self-healing phase of sensitization becomes operative. For a given heat treatment time at different holding temperatures in the sensitization region, the variation of Cr_{int} and W_{crit} is shown in Fig. 34(b). Cr_{int} increases with higher temperatures from $Cr_{int\text{-}1}$ to $Cr_{int\text{-}5}$. W_{crit} increases with an increase in temperature until a certain value, from $W_{crit\text{-}1}$ to $W_{crit\text{-}3}$ and then decreases to $W_{crit\text{-}4}$ before disappearing altogether. It was suggested by Sahlaoui [46] that only W_{crit} is needed in explaining the depletion characteristics and thereby DOS. However, for reasons given in later sections, both Cr_{int} and W_{crit} are considered when characterising the Cr depletion and explaining DOS and NDOS in this work.

The calculated concentration profiles for chromium, carbon, silicon and nickel obtained using DICTRA for the isothermal holding temperatures and times used in the experimental determination of DOS can be seen in Fig. 27–30. These reveal the similar behaviour of Cr depletion region and the corresponding characteristics as mentioned in Fig. 34. From Fig. 27, it is evident that the predicted depth of the chromium depleted zone decreases (Cr_{int} increases) with increasing temperature. The depths also decrease with holding time, but not to any significant extent in the time periods considered. The regression analyses described below showed that the best choice of Cr_{crit} on which W_{crit} values depend was found to be 12 wt.% Cr and is marked in Fig. 27. It is also apparent from Fig. 27 that there is a significant rise in W_{crit} with time, increasingly so as the temperature rises. From the concentration profiles, it is clear that carbon is depleted from the austenite over larger distances than chromium, which is expected and is shown in Fig. 28. From Fig. 27 and 28 it is clear that Cr is depleted for around 70 nm while C is depleted more than 280 nm when heat treated at 700 °C for 80 mins. Fig. 29 shows that silicon is rejected from the growing carbide into the austenite. However, the shape of the *concentration* profile, at first sight, appears unusual - the concentration of Si first increases and then decreases with increasing distance from the interface instead of just decreasing from a high value at the interface. Actually, the *activity* of Si decreases with increasing distance away from the interface as is required if Si is to diffuse away from the interface. The chemical interactions of Si with Ni and Cr result in the Si concentration profile to taking the shape seen. The solubility of Si and Ni in the carbide is minute, and both Si and Ni are rejected from ahead of the advancing interface while Cr is absorbed. Although, both Cr and Ni reduce the activity of Si, the initial increase in Si concentration with increasing distance from the interface is instigated by the influence of Ni.

The variation of Cr_{int} and W_{crit} with isothermal temperature and holding time for alloy 1.4310 can be seen in Fig. 35(a). Neither Cr_{int} nor W_{crit} alone correlates with the experimentally measured DOS values given in Fig. 13 (a), as shown in Fig. 35 (b) and (c). Bruemmer [75] in his work showed that the DOS will depend not only on the width of the chromium depleted zone as defined by some critical chromium concentration, but also on the depth of the depletion profile. Generally speaking, the depth of the depletion profile could be defined as Cr_{int} or (Cr_{crit} - Cr_{int}), for example. It is possible to visualize various depletion parameters that combine the terms W_{crit}, Cr_{crit} and Cr_{int}. Three such depletion parameters are (Cr_{crit} - Cr_{int})·W_{crit}, (Cr_{crit}/Cr_{int})·W_{crit} and W_{crit}/Cr_{int}. From the statistical analyses of the correlations between the experimentally measured DOS values and these potential depletion parameters based on a variety of definitions of Cr_{crit}, it was found that the best correlation is obtained with the following definition of a depletion parameter:

$$\mathrm{DP} = (12 - Cr_{int}) \cdot W_{crit} \tag{22}$$

in which W_{crit} is defined by Cr_{crit} = 12 wt.%. Fig. 35 (d) shows the non-linear correlation between this parameter and the experimental DOS values. It is clearly much better than the correlation between DOS and W_{crit} in Fig. 35 (c).

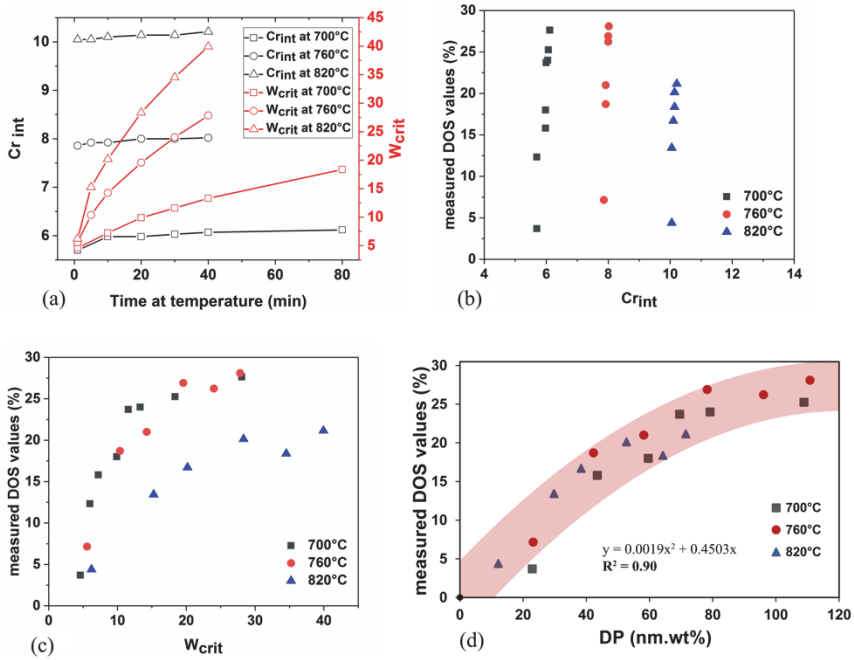

Fig. 35. Variation of (a) Cr_{int} and W_{crit} at 12 wt.% Cr with time at various isothermal temperatures for alloy 1.4310. (b,c,d) Variation of measured DOS as a function of Cr_{int}, W_{crit} and DP respectively (Reprinted by permission from Paper II © 2019 ISIJ).

Except the data point at DP = 22.3 nm.wt%, the data points of DOS lie in a scatter band that is +/- 4 DOS percentage points. The non-linear relation between DOS and DP is expected as long heat treatment times eventually lead to a decrease in DOS i.e. self-healing. By assuming that precipitate growth starts immediately without any incubation time, the precipitation process and development of Cr depleted zones can be reasonably modelled for the heat treatment conditions considered. However, it would be more reasonable to consider the nucleation times for low temperature heat treatments and might also reduce the scatter observed in the DOS - DP correlation. Any effects of C, Ni or Si concentration gradients on the electrochemical properties of the Cr depleted zones and thereby DOS have been ignored.

The same approach to modeling the DOS in terms of DP was carried out in Paper III, for the same alloy EN 1.4310 but heat treated for much longer times that caused self-healing in some cases. Also, a wider range of temperatures extending

to lower temperatures were included. Fig. 13 (b) shows that, for the temperatures and times studied, only the sample heat treated at the highest temperature, i.e. 820 °C, was able to achieve full self-healing as a result of its faster precipitation and diffusion kinetics. As low-temperature heat treatments were now included, it was necessary to account for the time taken to nucleate grain boundary $M_{23}C_6$, as given in Table 9, to give the starting point for the DICTRA calculations of Cr concentration profiles.

As in Paper II, the three same depletion parameters were again considered, i.e. $(Cr_{crit} - Cr_{int})\cdot W_{crit}$, $(Cr_{crit}/Cr_{int})\cdot W_{crit}$ and W_{crit}/Cr_{int}, but additionally the possibility of modifying the definition of Cr_{crit} was explored. Statistical analyses of the correlations between the experimentally measured DOS values and potential depletion parameters based on a variety of definitions of Cr_{crit} led to the best correlation being obtained with the following depletion parameter (DP)

$$\mathrm{DP} = \begin{cases} (12.5 - Cr_{int}) \cdot W_{crit} & Cr_{int} > 10.0 \\ (12.5 - 10.0) \cdot W_{crit} & Cr_{int} < 10.0 \end{cases}, \qquad (23)$$

where W_{crit} values are defined by Cr_{crit} = 12.5 wt.% but taking the minimum effective value of Cr_{int} to be 10 wt.%. In other words, it is assumed that chromium contents below 10 wt.% in the depleted zone have no extra effect on the tendency to intergranular corrosion and the DOS. In the above equation DP has the units wt.%.nm. Fig. 36(a) shows the variation of DP according to Eq. (23) as a function of time. At all the temperatures, DP increases with time and at 820 °C, DP starts to decrease after reaching a peak value which can be attributed to the self-healing behavior in a similar way to DOS as in Fig. 13(b). From this it is evident that the current approach is successful in able to produce sensitization and self-healing behavior very well. Although the considered 12% Cr as the Cr_{crit} in Paper II could able to identify the occurrence of sensitization, it could not able to predict the self-healing behavior. The choice of Cr_{crit} to be 12.5% Cr could able to predict both sensitization and self-healing.

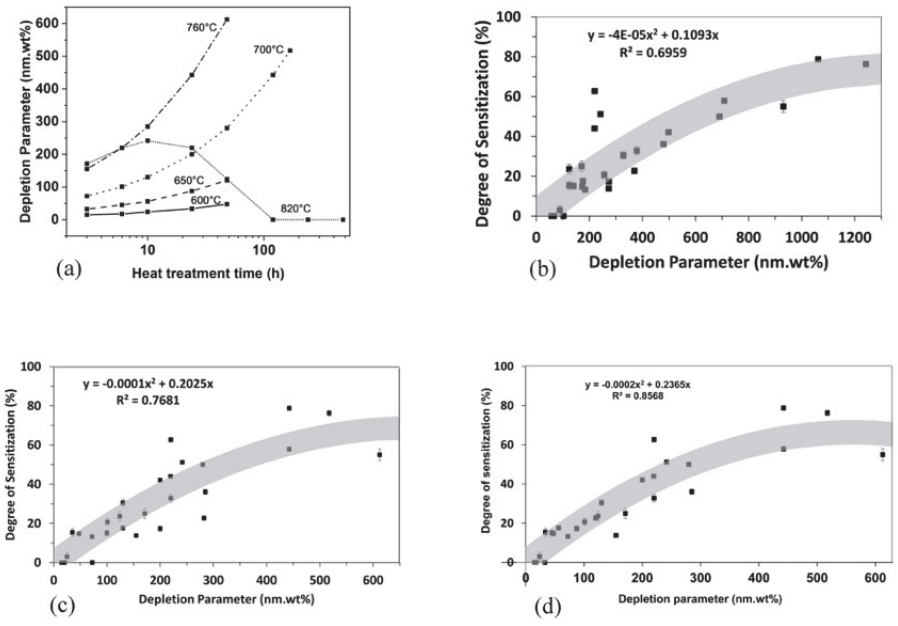

Fig. 36. Variation of (a) DP with heat treatment time, (b) measured DOS as a function of DP when 10 % Cr cut-off is not considered, (c) measured DOS as a function of DP when incubation time is ignored, and (d) measured DOS as a function of DP as defined by Eq. (23) (Reprinted by permission from Paper III © 2019 ISIJ).

A very poor correlation was observed between DOS and DP ignoring the 10 % Cr cut-off in the depletion parameter calculations, as can be seen from Fig. 36(b), which shows an R^2 value of only 0.69. When the cut-off is included as in Eq. (23), R^2 rises to 0.85 as shown in Fig. 36(d) and $DOS_{predcited}$ is given by

$$DOS_{predcited} = (0.2365 \times DP) - (0.0002 \times DP^2). \quad (24)$$

The importance of including nucleation times for $M_{23}C_6$ given in Table 8 can be seen by comparing Fig. 36(c) and Fig. 36(d): ignoring the nucleation time causes R^2 to drop from 0.85 to 0.76. It should be noted that the mentioned polynomial equation does not imply a correct functional description, but simply been applied to calculate R^2 values.

As in the case of Papers I–III, the same 1.4310 alloy was chosen for the study of grain size effects on sensitization in Paper IV. The heat treatments employed to produce different ranges of grain sizes also resulted in de-carburization giving

samples with both different grain sizes and carbon contents as was shown in Table 6. Only one sensitization temperature, 820 °C was chosen and the measured NDOS values for the corresponding heat treatments are shown in Fig. 15.

The calculated depletion characteristics are plotted as a function of heat treatment time at 820 °C in Fig. 37. Cr_{int} is lower and W_{crit} is higher in the 72 µm sample than in the 190 µm sample after 3 h of heat treatment at 820 °C. This can be attributed to the lower carbon content in the 190 µm sample that leads to a thinner grain boundary $M_{23}C_6$ film as shown in Fig. 37(d). The sample condition is considered to be completely self-healed when Cr_{int} reaches above 12.5% Cr as shown in Fig. 37(b).

The depletion parameter was calculated from the grain boundary chromium concentration profiles according to Eq. (23) i.e. by means of W_{crit} values defined by Cr_{crit} = 12.5%. As concluded in Paper III, chromium contents below 10.0 wt.% in the depleted zone have no extra effect on the propensity to intergranular corrosion and thereby the DOS values.

A regression analysis of the calculated values of DP based on Eq. (23) and the measured NDOS values from what experiments resulted in the following linear relation

$$\mathrm{NDOS} = 0.23 \times \mathrm{DP}\,, \tag{25}$$

where NDOS has percentage units and DP has the units wt.%.nm. The R^2 value for Eq. (25) is 0.85. This is quite good bearing in mind the simplicity of the model, which disregards, for example, the intragranular precipitation effects. The DP and thereby the predicted NDOS is controlled by the change in Cr_{int} and W_{crit}. The variation of measured NDOS values with computed DP values can be seen in the Fig. 38(a).

The chromium profiles will be affected by the presence of intragranular $M_{23}C_6$ and Cr_2N precipitates that are formed after long heat treatment times. Yet, these effects are ignored from the simple model that has been considered. That could be one reason for the inability of the model to predict the small rise in DOS after 168 h in all the sample conditions. Still, the trends of the measured NDOS values were very well predicted with the model.

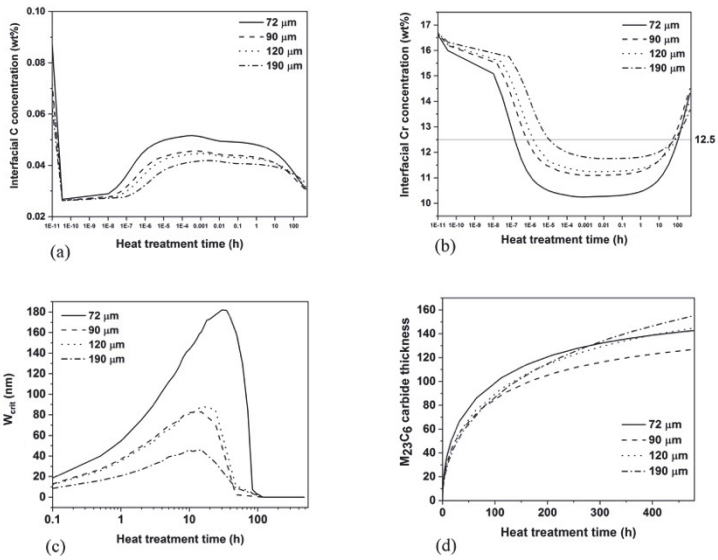

Fig. 37. Variation with heat treatment time of (a) interfacial carbon, (b) interfacial chromium at $M_{23}C_6$ carbide - austenite interface, (c) width of chromium concentration profile at Cr_{crit}, and (d) $M_{23}C_6$ thickness (Reprinted [adapted] under CC BY license from Paper IV © 2019 Authors).

The predicted NDOS values at 820 °C are plotted against time in Fig. 38(b). It can be seen that they follow the same trend as the experimentally measured NDOS values in Fig. 15. The predicted and measured times to peak NDOS are in accordance. The highest predicted peak NDOS is observed in the specimen with a grain size of 72 μm. As will be shown below, this is due to the fact that this specimen has the highest C content as well as the smallest grain size.

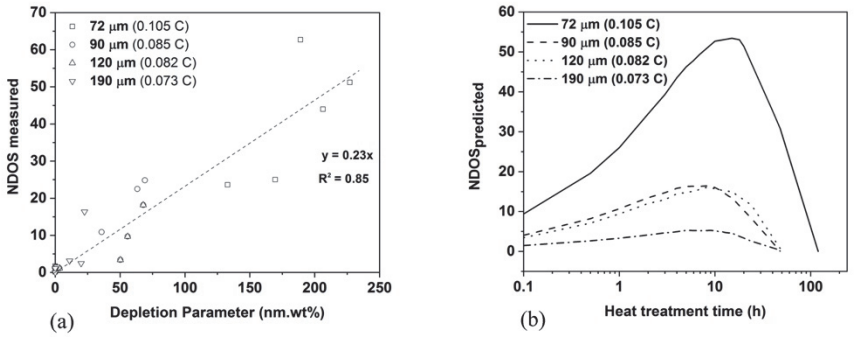

Fig. 38. (a) Measured NDOS vs. DP as calculated using Eq. (23). (b) Predicted NDOS with time at 820 °C for the samples with different grain sizes and carbon contents (Reprinted [adapted] under CC BY license from Paper IV © 2019 Authors).

It should be noted that a good correlation between DP and measured NDOS values was only found when taking d_a to be 1/6th of the average grain equivalent circle diameter; good correlations were not observed when d_a was taken to be one half of or the full average grain ECD, thus supporting the earlier assumption made by Sourmail [90] and the work by Kolli et al. [Paper II], [Paper III]. However, it is clear from this work that the proposed DP in Eq. (23) can be utilized in predicting the NDOS in samples with various grain sizes and carbon contents. The model can thus be extended to predict the NDOS for the samples of different grain sizes.

Similar approach used in Paper II, III and IV for characterizing the chromium depletion profiles was used to study and predict the effects of composition on sensitization and self-healing in the alloy compositions mentioned in Table 2. The same DP described in Eq. (23) was used for statistical correlations with the experimentally measured NDOS which resulted in the following equation

$$\mathrm{NDOS}_{\mathrm{predicted}} = (0.21 \times \mathrm{DP}) - (0.0002 \times \mathrm{DP}^2) \qquad (26)$$

with an R^2 value of 0.90. The predicted NDOS ($\mathrm{NDOS}_{\mathrm{predicted}}$) and the measured NDOS ($\mathrm{NDOS}_{\mathrm{measured}}$) are plotted in Fig. 39, show a very good correspondence. The $\mathrm{NDOS}_{\mathrm{predicted}}$ were plotted together with $\mathrm{NDOS}_{\mathrm{measured}}$ in Fig. 16 to get a better comparison between the two values. When the bulk chromium, Cr^* and Cr^{eff} were included in the prediction of NDOS, it did not promote the relationship. The reason could be the consideration of multicomponent diffusion in the calculation of DP and thereby $\mathrm{NDOS}_{\mathrm{predicted}}$. At low temperatures (550 °C), the model over-predicted the NDOS values, Fig. 16(e) and 16(f). The effect of the narrow chromium

depletion widths in these conditions might not have any significant effect on the sensitization susceptibility predicted by the model.

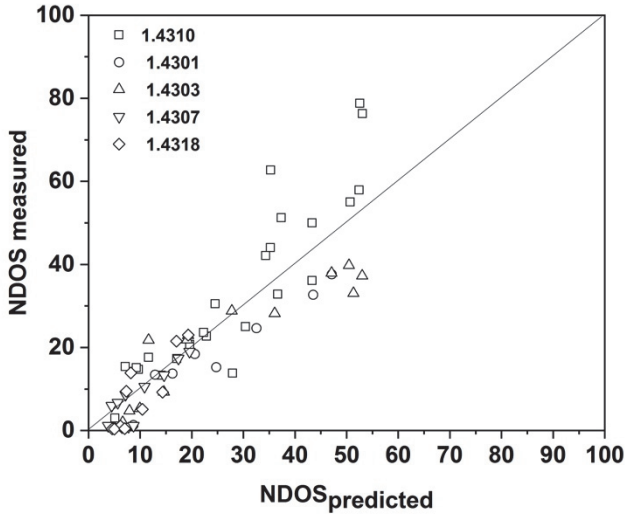

Fig. 39. Variation of measured NDOS and NDOS predicted using Eq. (26) (Under CC BY-NC-ND license from Paper V © 2020 Authors).

The relationships between measured and predicted NDOS given in Eq. (25) and Eq. (26) are similar except that in generation of Eq. (25), the DP^2 term was not included. The analysis of all the measured NDOS and simulated NDOS from Papers III–V, resulted in the same Eq. (26). The effect of grain size and composition based on the use of Eq. (26) for the prediction of NDOS will be explored in the next section.

5.2 The separate effects of grain size and composition

The effect of grain size alone on the $NDOS_{predicted}$ can be obtained by using PRISMA and DICTRA to calculate DP for various grain sizes, i.e. cell sizes d_a, and applying the relationship between NDOS and DP given by Eq. (26). The results are shown in Fig. 40. An increase in grain size at constant chemical composition (Fig. 40(a)) results in a rise in $NDOS_{predcited}$. The time to reach peak NDOS also shifted to longer times with increasing grain size. According to Li et al [12] and Taiwade et al. [32] an increase in grain size causes DOS to decrease. However, their

measurements did not take into consideration the geometrical effects i.e. the normalization of sensitization values with grain size and the variation of grain size alone.

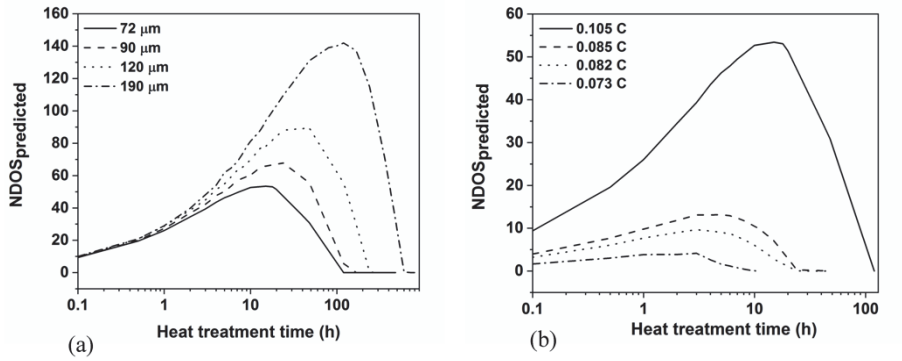

Fig. 40. NDOS predicted as a function of time at 820 °C from predicted values of DP combined with the relationship in Eq. (26): (a) for various grain sizes and the chemical composition Fe-16.80Cr-6.36Ni-0.95Si-0.10C, and (b) various carbon contents but otherwise the same chemical composition and a grain size of 72 μm (Under CC BY-NC-ND license from Paper V © 2020 Authors).

Stawström and Hillert [42] proposed expressions for calculating the heat treatment time periods that cause sensitization and desensitization in the material. However, the expressions were proposed only for 18-8 stainless steels with variation in carbon content.

Carbon and chromium are the key compositional variables that control the sensitization behavior; however, sensitization kinetics are affected by the other alloying elements too, through their impact on carbon and chromium activities.

The PRISMA + DICTRA calculations of depletion can be combined with the relationship in Eq. (26) to study the effect of individual alloying elements by keeping all the other alloying elements constant. Fig. 41 shows the results of such calculations for the separate effects of carbon, chromium and nickel content on the sensitization and self-healing behavior of the base composition Fe-16.80Cr-6.36Ni-0.95Si-0.10C isothermally heat treated at 820 °C. For example, the time to reach sufficient chromium depletion to give NDOS = 10% decreases with increasing carbon content, as can be seen in Fig. 41(a). Of course, low carbon content implies low carbon activity at the carbide-austenite interface, resulting in higher chromium activity. Also, according to the observation from the DICTRA simulations, the

mobility of chromium is slightly lowered with decrease in carbon content in austenite. With an increase in carbon from 0.07 to 0.12 wt.%, the peak NDOS increases, but it remains unchanged with further increases in carbon to 0.20 wt.%. Also, with an increase in carbon up to 0.12 wt.%, longer times are required to reach the predicted peak NDOS. However, the time required to reach peak NDOS is lowered with a further increase in the carbon content to 0.20 wt.%. The time to reach peak NDOS is the same as the start of self-healing. The temperature and carbon solubility control the amount of $M_{23}C_6$ precipitation and thereby the time to reach the predicted peak NDOS. Hence, the trends that are observed in the prediction of NDOS vary at different temperatures and will be different from the ones predicted here at 820 °C. The trends in time to reach peak NDOS are clarified by the combined effects of the 'C' type behaviour of the TTP curve and the effect of carbon on chromium diffusivity. Formation of $M_{23}C_6$ is the controlling step when the carbon content is less than 0.09 wt.%, while chromium diffusivity is the limiting step when the carbon content is above 0.09 wt.%.

The chromium content in the austenite matrix strongly affects the passivation characteristics in stainless steels. From Fig. 41(b) it is clear that the time to reach 10 % NDOS increases with an increase in chromium content. The driving force for $M_{23}C_6$ precipitation increases with higher chromium content; however, a high chromium in the austenite slows the depletion of chromium near the interface to below the critical level of 12 wt.%, in spite of relatively high degree of precipitation. Also, a higher chromium concentration results in higher chromium activity at the carbide-austenite interface. Together these effects result in combinations of Cr_{int} and W_{crit} that lead to a decrease in DP and NDOS with increasing Cr concentration. The predicted peak NDOS is relatively constant for 14–16 wt.% chromium, but it falls with further increases up to 20 wt.%. This can be attributed to increased chromium back diffusion into the depleted region from the austenite matrix far from the grain boundary as chromium increases from 16 to 20 wt.%. This back diffusion of chromium is less prominent in the case of 14–16 wt.% chromium, resulting in higher predicted NDOS values.

In austenitic stainless steels, in general, nickel is increased with increases in chromium content in order to stabilize the austenite. The influence of nickel on the solubility of carbon is shown in the Fig. 24(c) and 24(d). The increase in driving force for the $M_{23}C_6$ carbide precipitation is the reason for the increased predicted NDOS at any given time with nickel content as shown in Fig. 41(c), which in turn is due to the decreased carbon solubility in the austenite. From the standpoint of depletion characteristics, with an increase in nickel content, carbon activity

increases and chromium activity decreases at the $M_{23}C_6$ - austenite interface. This results in lower Cr_{int} values and W_{crit} values that rises with time. It is evident from Fig. 41(c) that the peak NDOS increases with nickel content as it increases the chromium and carbon mobilities in the austenite matrix along with the driving forces for carbide precipitation. The beginning of self-healing, which is the time to reach peak NDOS, is rather insensitive to the amount of nickel in the austenite in the range 5 to 10%. However, this start of self-healing shifted to shorter times as the nickel concentration increases from 10 to 14% due to an increase in chromium mobility that results from higher nickel contents. It is clear from the discussion that, for the ranges of alloying elements studied, carbon has the greatest effect on the predicted NDOS values.

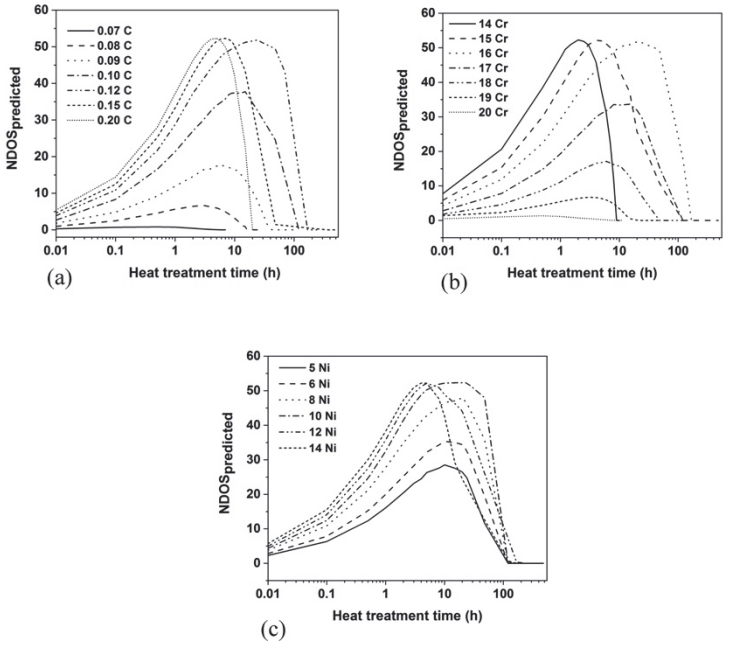

Fig. 41. NDOS predicted from the model extension with changes in (a) carbon, (b) chromium, (c) nickel contents when the material is heat treated at 820 °C. In each case, the composition is Fe-16.80Cr-6.26Ni-0.95Si-0.10C apart from the element that is varied (Under CC BY-NC-ND license from Paper V © 2020 Authors).

5.3 Importance of multicomponent effects

As the importance of multicomponent effects on $M_{23}C_6$ nucleation and growth has been stressed in this thesis, a comparative study has been done to estimate the magnitude of such effects. For the alloy 1.4310 that was isothermally heat treated at 600, 700 and 820 °C, the nucleation was simulated using TC-Prisma and the nucleation times for the $M_{23}C_6$ carbide precipitation on grain boundaries are presented in the Table 10. Only Fe, C and Cr are included in the simulations without considering multicomponent effects while all the elements are entered in the simulations considering multicomponent effects. The calculations with the Fe-0.10C-16.80Cr composition were made by forcing the Prisma and DICTRA software to only consider metastable equilibrium between austenite and $M_{23}C_6$, excluding the possibility of the ferrite phase. Therefore, the calculations only show the effect of the absence of Ni from austenite on precipitate nucleation and Cr diffusion.

Table 10. Nucleation times in alloy 1.4310 calculated using TC-Prisma with and without considering multicomponent effects.

Heat treatment temperatures (°C)	Nucleation time (s)	
	with multi. comp. effects	without multi. comp. effects
	Fe-0.10C-16.8Cr-6.36Ni-0.95Si	Fe-0.10C-16.80Cr
600	4690	9160
700	152	311
820	10	27

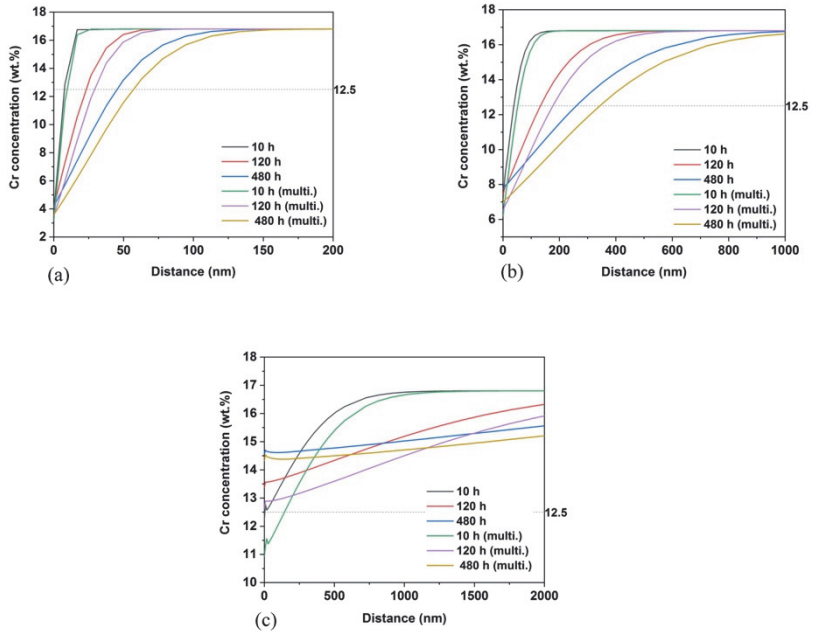

Fig. 42. Chromium concentration profiles calculated using TC-Prisma + DICTRA for the composition 0.10C-16.80Cr, i.e. without multicomponent effects, and the 1.4310 composition 0.10C-16.8Cr-6.36Ni-0.95Si, i.e. including multicomponent effects. (a) 600 °C, (b) 700 °C and (c) 820 °C.

The nucleation times are longer when multicomponent effects are ignored and the difference in nucleation times is appreciable at 600 °C. The growth is simulated after the nucleation times using DICTRA and the calculated chromium concentration profiles are given in Fig. 42. The concentration profiles that were calculated considering multicomponent effects are shown as 'multi.' in the legend of the Fig. 42. It is evident that at longer heat treatment times, the difference in W_{crit} is very significant. Along with W_{crit}, the interfacial chromium concentration Cr_{int} varies quite considerably at 820 °C. These calculations clearly show the importance of considering the multicomponent effects in modelling the $M_{23}C_6$ carbide precipitation and growth, as it significantly affects the chromium depletion characteristics that control the final NDOS prediction.

5.4 Importance of interfacial energies

The predicted nucleation times for the precipitation of grain boundary $M_{23}C_6$ strongly depend on the assumed interfacial energies between the carbide and austenite matrix. Deviations between assumed and actual interfacial energies will thus have a strong effect on the calculated nucleation times and thereby the growth simulations and the NDOS predictions. Although the calculated interfacial energies (using Becker's model) are in the range reported in the literature, the determination of these energies for the tested alloy would result in better NDOS predictions. The calculated interfacial energies with temperatures for the alloys 1.4310 and 1.4301 can be seen in Fig. 43. For instance, the nucleation times according to TC-Prisma when the interfacial energies are halved is shown in Table 11.

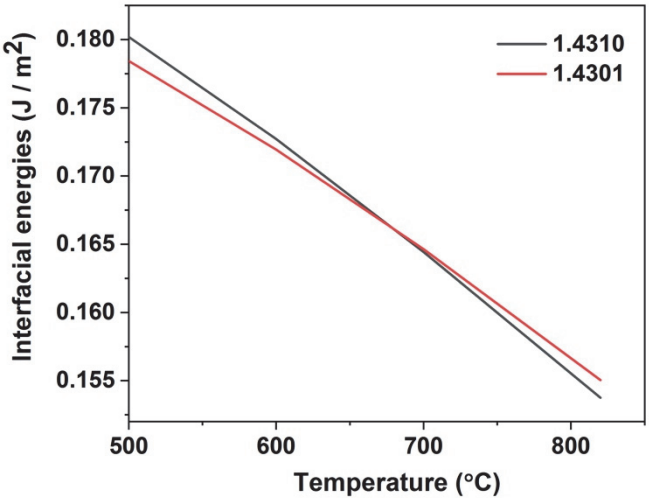

Fig. 43. Variation of interfacial energies at the grain boundary $M_{23}C_6$ - austenite matrix with temperature for the alloy grades 1.4310 and 1.4301 calculated using Becker's model in TC-Prisma.

Table 11. Calculated nucleation times in seconds from the start of holding for the formation of grain boundary $M_{23}C_6$ in the alloys studied when interfacial energies are considered to be half that of those calculated using Becker's model.

Alloy	% C (wt.)	550 °C	600 °C	700 °C	820 °C
1.4310	0.10	18381	2178	70	4
1.4301	0.04	18422	2324	90	10
1.4303	0.04	14793	1880	74	8
1.4307	0.02	28259	3978	240	0
1.4318	0.02	41174	6177	538	0

These times are considerably different than the nucleation times shown in Table 9. The effect is significant, specially at lower temperatures, here, 550 °C. When interfacial energy from Becker's model is used, carbides are predicted not to form at 550 °C in the alloys 1.4310, 1.4301 and 1.4303, while they are formed when the assumed interfacial energy is halved, after 20 days of heat treatment. This shows the sensitivity of calculated nucleation times to variation in interfacial energy and thereby the final NDOS predictions.

6 Summary and conclusions

The following grades of austenitic stainless steels: 1.4310, 1.4301, 1.4303, 1.4307 and 1.4318, have been tested for sensitization using the DL-EPR test and oxalic acid etching. Both sensitized and self-healed microstructures were identified and characterized using oxalic acid etching and STEM. The aim of the study was to predict experimentally measured DOS values with the help of models for precipitation and diffusion and thereby create a basis for avoiding heat treatments that cause sensitization.

In order to model the sensitization, CALPHAD techniques were used to calculate the chromium concentration profiles in the vicinity of grain boundary carbides. The main results and conclusions from this work can be summarized as follows.

- Sensitization kinetics are fastest at temperatures that that provide a balance of driving force for chromium carbide precipitation and mobility of chromium. The NDOS initially increased with an increase in heat treatment time and later decreased after reaching a peak NDOS that can be attributed to the start of self-healing. Of all the alloying elements, on a weight percentage basis, carbon has the greatest effect on the measured NDOS values: increasing carbon content leads to higher measured NDOS values.
- Oxalic acid etching and STEM analyses indicated the presence of $M_{23}C_6$ chromium carbides in both the sensitized and in self-healed samples.
- STEM measurements of chromium concentration profiles across the grain boundary $M_{23}C_6$ carbide - austenite matrix interface revealed chromium depletion, which was characterized by chromium concentrations in the vicinity of the precipitates falling below the critical concentration of 12% by wt. in sensitized specimens. The chromium concentration did not fall below this critical level in the samples that were not sensitized or that were self-healed.
- The precipitation module in Thermo-Calc, TC-Prisma was employed to calculate the nucleation times and TTP diagrams for $M_{23}C_6$ precipitation using interfacial energy values from Becker's model
- A one-dimensional model was used for the growth of grain boundary $M_{23}C_6$, assuming growth is diffusion controlled and that the grain boundaries operate as collector plates for the substitutional atoms diffusing through the austenite matrix to and from the precipitates.

- DICTRA together with the databases TCFE7 and MOBFE2 was employed to predict the chromium concentration profiles across the interface between $M_{23}C_6$ and the austenite matrix.
- A depletion parameter (DP) was defined based on the predicted chromium depletion profiles as given in Eq. (23).
- It has been shown that for a variety of grain sizes, compositions and thermal histories NDOS can be predicted from calculated values of DP using the formula given in Eq. (26).
- It was re-established that one sixth of average grain size can be considered as the cell size for the diffusion simulations using a 1D-model.
- According to the proposed model, an increase in grain size leads to an increase in the NDOS and the time to reach peak NDOS, i.e. the time to the start of self-healing.
- Increases in both carbon and nickel contents lead to increased sensitization kinetics. This can be attributed to the increased driving force for $M_{23}C_6$ precipitation and the rise in the carbon activity at the carbide matrix - interface. Chromium above 16 wt.% resulted in increased chromium activity at the carbide - austenite interface and increased mobility of chromium in the austenite matrix, and thereby to slower sensitization kinetics.

7 Novel features

To the best knowledge of the author, the following findings are original to this work:

- The extensive experimental investigation of sensitization in austenitic stainless steels with varied composition, grain size and thermal history followed with comprehensive microstructural investigations identifying the sensitized and self-healed conditions based on the chromium depletion regions in the vicinity of grain boundary carbides.
- Extensive use of the thermodynamic and kinetic databases and the associated CALPHAD based Thermo-Calc software for the prediction of equilibrium phase fractions and the solution of the moving phase boundary problem considering multicomponent effects and without the need of assuming a uniform activity of carbon. Also, the consideration of nucleation times in modelling the growth of $M_{23}C_6$ carbides.
- The successful prediction of chromium depleted regions and their characterization using a novel depletion parameter that was able to explain the experimentally observed sensitization behaviour.
- The development of a one-dimensional model for sensitization and self-healing behaviour in austenitic stainless steels, by combining the diffusion model in Thermo-Calc and with experimentally measured DOS values.
- The study of the effect of individual elemental concentrations, thermal history and grain size on the sensitization development and self-healing in austenitic stainless steels by extending the proposed one-dimensional model.

8 Recommendations for further research

On the basis of DL-EPR experiments together with Thermo-Calc, TC-Prisma and DICTRA simulations, this thesis identifies methods to characterize the grain boundary chromium depletion in austenitic stainless steels responsible for sensitization. In this work, rather a limited range of chemical compositions has been used and in order to more extensively validate the proposed model, a wider range of chemistries should be explored. Literature data alone is insufficient as the amount of data based on the use of the DL-EPR test method is rather limited. Also, the proposed model also needs to be validated for varying grain sizes by keeping all the other variables constant for different ranges of compositions.

The simple 1-D diffusion model does not consider the intragranular precipitation of $M_{23}C_6$ that can occur after long heat treatment times but its inclusion could be important in estimating chromium concentration profiles at the grain boundaries. The intragranular carbides decrease the amount of chromium available for grain boundary $M_{23}C_6$ carbides and thereby affect the chromium depletion, especially at long heat treatment times.

Both thermodynamic and kinetic databases available in Thermo-Calc are highly useful in interpreting the material properties and making full use of them is possible with the help of TC-Python software development kit. The numerical packages NumPy and SciPy can be used and thus making it a tool for integrated computational materials engineering. Using the above-mentioned kit, one can custom build or write a code to solve the diffusion equations that include the intragranular carbide precipitation, by decreasing the available elemental concentration for grain boundary precipitation at each time step. This would also help in exclusively calculating the NDOS for any sample composition and thermal history.

The studies concerning non-isothermal heat treatments presented in Paper I need to be extended. However, the challenges in choosing the interfacial energies at $M_{23}C_6$ - austenite matrix for estimating nucleation during non-isothermal heat treatments need to be addressed.

The influence of grain boundary misorientation on the nucleation of chromium carbides could be done using EBSD thereby providing a better understanding of the effect of grain boundary misorientation on sensitization. A larger set of data from more extensive EDS measurements regarding the chromium concentration at the carbide - austenite interface would help in acquiring statistically significant data to compare with the simulations.

The above-mentioned work, if performed, provides more comprehensive view and estimation of sensitization in unstabilized austenitic stainless steels that can be further extended to stabilised austenitic and ferritic grades.

List of references

[1] R. A. Lula, *Stainless Steel*. American Society for Metals, 1986.

[2] G. George and H. Shaikh, "Introduction to austenitic stainless steels", in *Corrosion of Austenitic stainless steels - mechanisms, mitigation and monitoring*, edited by H. S. Khatak and B. Raj, Narosa publications, 2002, ch. 1, pp. 1–3.

[3] L. Karlsson, *Stainless steels past, present and future*. ESAD AB, Gothenburg, 2004, pp. 1–6.

[4] A. J. Sedriks, *Corrosion of stainless steels.*, 2nd ed., 1979.

[5] S. M. Bruemmer, "Quantitative measurement and modeling of sensitization development in stainless steels," *Corrosion*, vol. 46, no. 9, pp. 556–562, 1990.

[6] M. Cortie, "Ferritic stainless steels," in *Encyclopedia of Materials: Science and Technology*, Elsevier Science Ltd., 2013, pp. 3037–3039.

[7] P. Lambert, "Sustainability of metals and alloys in construction", in *Sustainability of Conctruction Materials*, 2nd ed., Elsevier Ltd., 2016, pp. 105–128.

[8] *Design Guidelines for Selection and Use of Stainless Steel - A Designers' Handbook Series No 9014*, AISI and SSINA (Distributed by Nickel Develop. Inst.), 2011. [Online]. Available: https://www.nickelinstitute.org/media/4664/ni_aisi_9014_selectionuse.pdf

[9] P. Lacombe, B. Baroux, and G. Beranger, *Stainless steels*. Les Ulis: Les Éditions de Physique, 1993.

[10] P. Smith, "Metallic Materials for Piping Components," in *The Fundamentals of Piping Design*, Elsevier, 2007, pp. 115–136.

[11] G. S. Frankel, "Pitting corrosion of metals a review of the critical factors," *Journal of The Electrochemical Society,* vol. 145, no. 6, pp. 2186–2198, 1998.

[12] V. S. Raja and T. Shoji, *Stress Corrosion Cracking: Theory And Practice*. Woodhead Publishing, 2011.

[13] P. Andresen et al., "Expert Panel Report on Proactive Materials Degradation Assessment", Brookhaven National Laboratory, U. S. Nuclear Regulatory Commission Office of Nuclear Regulatory Research, Washington DC, CR-923, 2007.

[14] J. Föhl, "Aging and life extension of major light water reactor components," *Nucl. Eng. Des.*, vol. 150, no. 1, p. 193, Sep. 1994.

[15] S. H. Bush and R. L. Dillon, "Stress Corrosion in Nuclear Systems," Pacific Northwest laboratories, a division of Battelle Memorial Institute, Battelle Boulevard Richland, Washington 99352, 1973.

[16] M. O. Speidel, "Stress corrosion cracking and corrosion fatigue fracture mechanics," in *Corrosion in power genrating equipment*, Proceedings of 8th Int. Brown Boveri Symposium, Plenum, New York, USA, 1984, pp. 85–132.

[17] H. Kokawa, M. Shimada, and Y. S. Sato, "Grain-boundary structure and precipitation in sensitized austenitic stainless steel," *JOM*, vol. 52, no. 7, pp. 34–37, Jul. 2000.

[18] M. Shimada, H. Kokawa, Z. Wang, Y. Sato, and I. Karibe, "Optimization of grain

boundary character distribution for intergranular corrosion resistant 304 stainless steel by twin-induced grain boundary engineering," *Acta Mater.*, vol. 50, no. 9, pp. 2331–2341, May 2002.

[19] H. Kokawa, T. Koyanagawa, M. Shimada, Y. S. Sato, and T. Kuwana, "Dependence of Carbide Precipitation on Grain Boundary Structure in Sensitized Austenitic Stainless Steel," in *Properties of Complex Inorganic Solids 2*, no. I, Boston, MA: Springer US, 2000, pp. 17–26.

[20] Y. Zhou, K. . Aust, U. Erb, and G. Palumbo, "Effects of grain boundary structure on carbide precipitation in 304L stainless steel," *Scr. Mater.*, vol. 45, no. 1, pp. 49–54, Jul. 2001.

[21] G. Palumbo, "Thermomechanical processing of metallic materials," US Patent No. 5817193, 1998.

[22] P. Lin, G. Palumbo, U. Erb, and K. T. Aust, "Influence of grain boundary character distribution on sensitization and intergranular corrosion of alloy 600," *Scr. Metall. Mater.*, vol. 33, no. 9, pp. 1387–1392, Nov. 1995.

[23] T. Watanabe, "Grain Boundary Architecture for High Performance Materials in Boundaries and Interfaces in Materials", in *The Minerals, Metals and Materials Society*, Warrendale, PA, 1998, pp. 19–28.

[24] K. Sugimoto and Y. Sawada, "The role of molybdenum additions to austenitic stainless steels in the inhibition of pitting in acid chloride solutions," *Corros. Sci.*, vol. 17, no. 5, pp. 425–445, 1977.

[25] T. Massoud, V. Maurice, L. H. Klein, A. Seyeux, and P. Marcus, "Nanostructure and local properties of oxide layers grown on stainless steel in simulated pressurized water reactor environment," *Corros. Sci.*, vol. 84, pp. 198–203, 2014.

[26] I. Olefjord and B. O. Elfstrom, "Composition of the surface during passivation of stainless steels.," *Corrosion*, vol. 38, no. 1, pp. 46–52, 1982.

[27] N. E. Hakiki, "Semiconducting properties of passive films formed on stainless steels," *J. Electrochem. Soc.*, vol. 145, no. 11, p. 3821, 1998.

[28] E. De Vito and P. Marcus, "XPS study of passive films formed on molybdenum-implanted austenitic stainless steels," *Surf. Interface Anal.*, vol. 19, no. 1–12, pp. 403–408, Jun. 1992.

[29] W. Yang, R.-C. Ni, H.-Z. Hua, and A. Pourbaix, "The behavior of chromium and molybdenum in the propagation process of localized corrosion of steels," *Corros. Sci.*, vol. 24, no. 8, pp. 691–707, Jan. 1984.

[30] T. Bellezze, G. Giuliani, and G. Roventi, "Study of stainless steels corrosion in a strong acid mixture . Part 1 : cyclic potentiodynamic polarization curves examined by means of an analytical method," *Corros. Sci.*, vol. 130, no. October 2017, pp. 113–125, 2018.

[31] E. E. Stansbury and R. A. Buchanan, *The Fundamentals of Electrochemical Corrosion*, ASM International, 2000.

[32] G. S. Frankel, "Pitting corrosion of metals - A review of the critical factors," *J. Electrochem. Soc.*, vol. 145, no. 6, pp. 2186–2198, 1998.

[33] M. G. Fontana, *Corrosion Engineering*. McGraw-Hill Book Company, 1986.

[34] Briant C.L, Mulford R.A, and Hall E.L, "Sensitization of austenitic stainless steels I controlled purity alloys," *Corrosion*, vol. 38, pp. 468–477, 1982.

[35] K. T. Aust, J. H. Armijo, E. F. Koch, and J. H. Westbrook, "Intergranular corrosion and mechanical properties of austenitic stainless steels," *Trans. Quart ASM*, vol. 60, pp. 360, 1967.

[36] D. A. Vermilyea and C. S. Tedmon, "Discussion of 'intergranular corrosion of austenitic stainless steels,'" *Metall. Trans.*, vol. 1, no. 4, p. 1076, 1970.

[37] R. L. Cowan and C. S. Tedmon, "Intergranular Corrosion of Iron-Nickel-Chromium Alloys," in *Advances in Corrosion Science and Technology*, M. G. Fontana and R. W. Staehle, Eds. Boston, MA: Springer US, 1973, pp. 293–400.

[38] J. S. Armijo, "Impurity adsorption and intergranular corrosion of austenitic stainless steel in boiling HNO_3-$K_2Cr_2O_7$ solutions," *Corrosion*, vol. 7, pp. 147–150, 1967.

[39] R. Stickler and A. Vinckier, "Morphology of grain-boundary carbides and its influence on intergranular corrosion of 304 stainless steel," *Trans ASM*, vol. 54, pp. 362–380, 1961.

[40] E. C. Bain, R. H. Aborn, and J. B. Rutherford, "The nature and prevention of intergranular corrosion in austenitic stainless steels," *Trans. Am. Soc. Steel Treat*, vol. 21, p. 481, 1933.

[41] F. G. Wilson, "Mechanism of intergranular corrosion of austenitic stainless steels—literature review," *Br. Corros. J.*, vol. 6, no. 3, pp. 100–108, May 1971.

[42] C. Stawstrom and M. Hillert, "An improved depleted-zone theory of intergranular corrosion of 18-8 stainless steel ," *J.Iron.Steel.I*, vol. 207, pp. 77–85, 1969.

[43] S. K. Mannan, R. K. Dayal, M. Vijayalakshmi, and N. Parvathavarthini, "Influence of deformation on sensitization kinetics and its microstructural correlation in a nuclear grade 316 stainless steel," *J. Nucl. Mater.*, vol. 126, no. 1, pp. 1–8, 1984.

[44] N. Parvathavarthini, R. K. Dayal, S. K. Seshadri, and J. B. Gnanamoorthy, "Continuous cooling and low temperature sensitization of AISI Types 316 SS and 304 SS With different degrees of cold work," *J. Nucl. Mater.*, vol. 168, no. 1–2, pp. 83–96, 1989.

[45] C. S. Pande, M. Suenaga, B. Vyas, H. S. Isaacs, and D. F. Harling, "Direct evidence of chromium depletion near the grain boundaries in sensitized stainless steels," *Scr. Metall.*, vol. 11, no. 8, pp. 681–684, 1977.

[46] H. Sahlaoui, K. Makhlouf, H. Sidhom, and J. Philibert, "Effects of ageing conditions on the precipitates evolution, chromium depletion and intergranular corrosion susceptibility of AISI 316L: Experimental and modeling results," *Mater. Sci. Eng. A*, vol. 372, no. 1–2, pp. 98–108, 2004.

[47] E. A. Trillo *et al.*, "Combined effects of deformation (strain and strain state), grain size, and carbon content on carbide precipitation and corrosion sensitization in 304 stainless steel," *Mater. Charact.*, vol. 35, no. 2, pp. 99–112, 1995.

[48] H. S. Betrabet, K. Nishimoto, B. E. Wilde, and W. A. T. Clark, "Electrochemical and microstructural investigation of grain boundary precipitation in AISI 304 stainless steels containing nitrogen," *Corrosion*, vol. 43, no. 2, pp. 77–84, 1987.

[49] T. Thorvaldsson and G. L. Dunlop, "Grain boundary Cr-depleted zones in Ti and

Nb stabilized austenitic stainless steels," *J. Mater. Sci.*, vol. 18, no. 3, pp. 793–803, Mar. 1983.

[50] S. M. Bruemmer and L. A. Charlot, "Development of grain boundary chromium depletion in type 304 and 316 stainless steels," *Scr. Metall.*, vol. 20, no. 7, pp. 1019–1024, Jul. 1986.

[51] E. Folkhard, "Welding Metallurgy of Austenitic Stainless Steels," in *Welding Metallurgy of Stainless Steels*, Vienna: Springer Vienna, 1988, pp. 197–222.

[52] V. Cihal, "Intergranular corrosion of Cr-Ni stainless steel" *Prot. Mater.*, vol. 4, p. 563, 1968.

[53] T. M. Devine, "Influence of carbon content and ferrite morphology on the sensitization of duplex stainless steel," *MTA* 11, pp. 791–800, 1980

[54] G. L. Edgemon, P. F. Tortorelli, and G. E. C. Bell, "Effects of compositional modifications on the sensitization behavior of FeCrMn steels," *J. Nucl. Mater.*, vol. 191–194, pp. 997–1001, Sep. 1992.

[55] G. E. C. Bell, P. F. Tortorelli, E. A. Kenik, and R. L. Klueh, "An investigation of the sensitization behavior of Fe-Mn-Cr austenitic steels," *J. Nucl. Mater.*, vol. 179–181, pp. 615–618, Mar. 1991.

[56] R. F. A. Jargelius-Pettersson, "High nitrogen steels. sensitization behaviour and corrosion resistance of austenitic stainless steels alloyed with nitrogen and manganese," *ISIJ Int.*, vol. 36, no. 7, pp. 818–824, 1996.

[57] A. Joshi and D. F. Stein, "Chemistry of grain boundaries and its relation to intergranular corrosion of austenitic stainless steel," *Corrosion*, vol. 28, no. 9, pp. 321–330, Sep. 1972.

[58] T. A. Mozhi, W. A. T. Clark, K. Nishimoto, W. B. Johnson, and D. D. Macdonald, "The effect of nitrogen on the sensitization of aisi 304 stainless steel," *Corrosion*, vol. 41, no. 10, pp. 555–559, Oct. 1985.

[59] R. Beltran, J. G. Maldonado, L. E. Murr, and W. W. Fisher, "Effects of strain and grain size on carbide precipitation and corrosion sensitization behavior in 304 stainless steel," *Acta Mater.*, vol. 45, no. 10, pp. 4351–4360, Oct. 1997.

[60] R. Beltran, E. A. Trillo, R. J. Romero, L. E. Murr, A. H. Advani, and W. W. Fisher, "Combined effects of strain and grain size on carbide precipitation and sensitization in 304 stainless steel," *Scr. Metall. Mater.*, vol. 30, no. 8, pp. 1021–1025, Apr. 1994.

[61] R. Pascali, A. Benvenuti, and D. Wenger, "Carbon content and grain size effects on the sensitization of AISI type 304 stainless steels," *Corrosion*, vol. 40, no. 1, pp. 21–32, 1984.

[62] X. Yu, S. Chen, Y. Liu, and F. Ren, "A study of intergranular corrosion of austenitic stainless steel by electrochemical potentiodynamic reactivation, electron back-scattering diffraction and cellular automaton," *Corros. Sci.*, vol. 52, no. 6, pp. 1939–1947, 2010.

[63] S. X. Li, Y. N. He, S. R. Yu, and P. Y. Zhang, "Evaluation of the effect of grain size on chromium carbide precipitation and intergranular corrosion of 316L stainless steel," *Corros. Sci.*, vol. 66, pp. 211–216, 2013.

[64] *Standard Test Method for Electrochemical Reactivation (EPR) for Detecting*

Sensitization of AISI Type 304 and 304L Stainless Steels, ASTM G108-94, Annu. B. ASTM Stand., vol. 94, no. Reapproved 2010, pp. 1–9, 2010.

[65] H. Shaikh *et al.*, "Use of eddy current testing method in detection and evaluation of sensitisation and intergranular corrosion in austenitic stainless steels," *Corros. Sci.*, vol. 48, no. 6, pp. 1462–1482, 2006.

[66] S. Pednekar and S. Smialowska, "Effect of prior cold work on the degree of sensitization in type 304 stainless steel," *Corrosion*, vol. 36, no. 10, pp. 565–577, Oct. 1980.

[67] N. Parvathavarthini and U. K. Mudali, "Electrochemical techniques for estimating the degree of sensitization in austenitic stainless steels," *Corros. Rev.*, vol. 32, no. 5–6, Jan. 2014.

[68] K. Osozawa, K. Bohnenkamp, and H.-J. Engell, "Potentiostatic study on the intergranular corrosion of an austenitic chromium-nickel stainless steel," *Corros. Sci.*, vol. 6, no. 9, pp. 421–433, Jan. 1966.

[69] J. H. Payer and R. W. Staehle, "The dissolution behavior of cr23c6 and tic related to the stainless steels in which they occur," *Corrosion*, vol. 31, no. 1, pp. 30–38, Jan. 1975.

[70] T. M. Devine, "The mechanism of sensitization of austenitic stainless steel," *Corros. Sci.*, vol. 30, no. 2–3, pp. 135–151, 1990.

[71] P. Chung and S. Szklarska-Smialowska, "The effect of heat treatment on the degree of sensitization of type 304 stainless steel," *Corrosion*, vol. 37, no. 1, pp. 39–50, Jan. 1981.

[72] P. Aaltonen, I. Aho-Mantila, and H. Hänninen, "Electrochemical methods for testing the intergranular corrosion susceptibility of stainless steels," *Corros. Sci.*, vol. 23, no. 4, pp. 431–440, Jan. 1983.

[73] V. Cihal, J. Furijchova, and J. Kubelka, "Electrochemical method to study the intercrystalline corrosion susceptibility of stainless steels," *Werkst Korros*, 27, pp. 782–788, 1976.

[74] H. Hanninen, "Intergranular Stress Corrosion Cracking, Final Report of the NKA Project MAT530," Graphic Systems AB, Malmö, September. 1989.

[75] J. C. Charbonnier and T. Jossic, "An electrochemical study of intergranular corrosion related to the chromium depletion mechanism in the case of 18-10 austenitic stainless steels," *Corros. Sci.*, vol. 23, no. 11, pp. 1191–1206, Jan. 1983.

[76] *Corrosion of metals and alloys - Electrochemical potentiokinetic reactivation measurement using the double loop method (based on Cihal's method) (ISO 12732:2006),* EN ISO 12732:2008, Finnish Stand. Assoc. SFS, pp. 14, 2008.

[77] S. Rahimi, D. L. Engelberg, and T. J. Marrow, "Characterisation of grain boundary cluster compactness in austenitic stainless steel," *Mater. Sci. Technol.*, vol. 26, no. 6, pp. 670–675, 2010.

[78] C. Zener, "Theory of growth of spherical precipitates from solid solution," *J. Appl. Phys.*, vol. 20, no. 10, pp. 950–953, 1949.

[79] E. L. Hall and C. L. Briant, "Chromium depletion in the vicinity of carbides in sensitized austenitic stainless steels," *Metall. Trans. A, Phys. Metall. Mater. Sci.*,

vol. 15 A, no. 5, pp. 793–811, 1984.
[80] K. Natesan and T. F. Kassner, “Thermodynamics of carbon in nickel, iron-nickel and iron-chromium-nickel alloys,” *Metall. Trans.*, vol. 4, no. 11, pp. 2557–2566, Nov. 1973.
[81] C. Zener, “Theory of growth of spherical precipitates from solid solution,” *J. Appl. Phys.*, vol. 20, no. 10, pp. 950–953, Oct. 1949.
[82] F. C. Frank, “Radially symmetric phase growth controlled by diffusion,” *Proc. R. Soc. London. Ser. A. Math. Phys. Sci.*, vol. 201, no. 1067, pp. 586–599, May 1950.
[83] F. S. Ham, “Shape-preserving solutions of the time-dependent diffusion equation,” *Q. Appl. Math.*, vol. 17, no. 2, pp. 137–145, Jul. 1959.
[84] G. S. Was and R. M. Kruger, “A thermodynamic and kinetic basis for understanding chromium depletion in Ni-Cr-Fe alloys,” *Acta Metall.*, vol. 33, no. 5, pp. 841–854, 1985.
[85] F. Kohler, “Zur berechnung der thermodynamischen daten eines ternären systems aus den zugehörigen binären systemen - kurze mitteilung,” *Monatshefte für Chemie*, vol. 91, no. 4, pp. 738–740, 1960.
[86] R. L. Fullman, “A thermodynamic model of the effects of composition on the susceptibility of austenitic stainless steels to intergranular stress corrosion cracking,” *Acta Metall.*, vol. 30, no. 7, pp. 1407–1415, Jul. 1982.
[87] W. E. Mayo, “Predicting IGSCC/IGA susceptibility of Ni-Cr-Fe alloys by modeling of grain boundary chromium depletion,” *Mater. Sci. Eng. A*, vol. 232, no. 1–2, pp. 129–139, Jul. 1997.
[88] H. Sahlaoui, H. Sidhom, and J. Philibert, “Prediction of chromium depleted-zone evolution during aging of Ni-Cr-Fe alloys,” *Acta Mater.*, vol. 50, no. 6, pp. 1383–1392, 2002.
[89] D. E. Coates, “Diffusion-controlled precipitate growth in ternary systems I,” *Metall. Trans.*, vol. 3, no. 5, pp. 1203–1212, May 1972.
[90] D. E. Coates, “Diffusional growth limitation and hardenability,” *Metall. Trans.*, vol. 4, no. 10, pp. 2313–2325, Oct. 1973.
[91] T. Sourmail, C. H. Too, and H. K. D. H. Bhadeshia, “Sensitisation and evolution of chromium-depleted zones in Fe-Cr-Ni-C systems,” *ISIJ Int.*, vol. 43, no. 11, pp. 1814–1820, 2003.
[92] L. Kaufman and H. Bernstein, *Computer Calculations of Phase Diagrams*. New York: Academic Press, 1970.
[93] H. L. Lukas, S. G. Fries, and B. Sundman, *Computational thermodynamics: The Calphad method*, Cambridge: Cambridge University Press, 2007.
[94] J. J. van Laar, “Die schmelz- oder erstarrungskurven bei binären systemen, wenn die feste phase ein gemisch (amorphe feste lösung oder mischkristalle) der beiden komponenten ist,” *Zeitschrift für Phys. Chemie*, vol. 63U, no. 1, Jan. 1908.
[95] L. Kaufman and H. Bernstein, “Computer calculation of phase diagrams with special reference to refractory metals,” *Refract. Mater.*, no. 4, pp. XI, 334 S., 1970.
[96] A. Dinsdale, “SGTE Unary Database, Version 5.0.” Scientific Group Thermodata Europe, Teddington, U. K., 2001.

[97] L. Kaufman, “The lattice stability of metals—I. Titanium and zirconium,” *Acta Metall.*, vol. 7, no. 8, pp. 575–587, Aug. 1959.

[98] M. Hillert, “The compound energy formalism,” *J. Alloys Compd.*, vol. 320, no. 2, pp. 161–176, May 2001.

[99] M. Paul. The application of CALPHAD based tools to the materials genome Initiative and ICME. Available: http://icmed.engin.umich.edu/wp-content/uploads/sites/176/2019/06/Thermo-Calc-Lecture_2019.pdf

[100] N. Parvathavarthini and R. K. Dayal, “Influence of chemical composition, prior deformation and prolonged thermal aging on the sensitization characteristics of austenitic stainless steels,” *J. Nucl. Mater.*, vol. 305, no. 2–3, pp. 209–219, 2002.

[101] N. Parvathavarthini and U. K. Mudali, “Electrochemical techniques for estimating the degree of sensitization in austenitic stainless steels,” *Corros. Rev.*, vol. 32, no. 5–6, pp. 183–225, 2014.

[102] N. Parvathavarthini, *Sensitization and Testing for Intergranular Corrosion*. Alpha Science International Ltd, 2002.

[103] F. Bachmann, R. Hielscher, and H. Schaeben, “Grain detection from 2d and 3d EBSD data-Specification of the MTEX algorithm,” *Ultramicroscopy*, vol. 111, no. 12, pp. 1720–1733, 2011.

[104] G. Cliff and G. W. Lorimer, “The quantitative analysis of thin specimens,” *J. Microsc.*, vol. 103, no. 2, pp. 203–207, Mar. 1975.

[105] J. O. Andersson and J. Ågren, “Models for numerical treatment of multicomponent diffusion in simple phases,” *J. Appl. Phys.*, vol. 72, no. 4, pp. 1350–1355, 1992.

[106] B. Jönsson, “Ferromagnetic ordering and diffusion of carbon and nitrogen in bcc Cr-Fe-Ni alloys,” *Zeitschrift für Met.*, vol. 85, no. 7, pp. 498–501, 1994.

[107] B. Jönsson, “Assessment of the mobility of carbon in fcc C-Cr-Fe-Ni alloys,” *Zeitschrift für Met.*, vol. 85, no. 7, pp. 502–509, 1994.

[108] B. Jönsson, “Assessment of the mobilities of cr, fe and ni in bcc cr-fe-ni alloys,” *ISIJ Int.*, vol. 35, no. 11, pp. 1415–1421, 1995.

[109] A. Engström and J. Ågren, “Assessment of diffusional mobilities in face-centered cubic Ni-Cr-Al alloys,” *Zeitschrift fuer Met. Res. Adv. Tech.*, vol. 87, no. 2, pp. 92–97, 1996.

[110] A. Borgenstam, L. Höglund, J. Ågren, and A. Engström, “DICTRA, a tool for simulation of diffusional transformations in alloys,” *J. Phase Equilibria*, vol. 21, no. 3, pp. 269–280, 2000.

[111] M. . Lewis and B. Hattersley, “Precipitation of M23C6 in austenitic steels,” *Acta Metall.*, vol. 13, no. 11, pp. 1159–1168, 1965.

[112] F. R. Beckitt and B. R. Clark, “The shape and mechanism of formation of M23C6 carbide in austenite,” *Acta Metall.*, vol. 15, no. 1, pp. 113–129, 1967.

[113] H. B. Aaron and H. I. Aaronson, “Growth of grain boundary precipitates in Al-4% Cu by interfacial diffusion,” *Acta Metall.*, vol. 16, no. 6, pp. 789–798, Jun. 1968.

[114] R. E. Hoffman and D. Turnbull, “Lattice and grain boundary self-diffusion in cadmium,” *J. Appl. Phys.*, vol. 22, no. 5, pp. 634–639, 1951.

[115] A. Atkinson, “Grain boundary diffusion - structural effects and mechanisms,” *J.*

Phys. Colloq., vol. 46 (C4), pp. 379-391, 1985.

[116] H. Larsson and R. C. Reed, "On the numerical simulation of diffusion-controlled reactions under local equilibrium conditions," *Acta Mater.*, vol. 56, no. 15, pp. 3754–3760, 2008.

[117] Q. Chen, K. Wu, G. Sterner, and P. Mason, "Modeling precipitation kinetics during heat treatment with calphad-based tools," *J. Mater. Eng. Perform.*, vol. 23, no. 12, pp. 4193–4196, 2014.

[118] R. Kampmann and R. Wagner, "Kinetics of precipitation in metastable binary alloys—theory and application to Cu-1.9 at.% Ti and Ni-14 at.% Al," in *Decomposition of alloys: the early stages*, Pergamon Press, Oxford, 1984, pp. 91–103.

[119] J. S. Langer and A. J. Schwartz, "Kinetics of nucleation in near-critical fluids," *Phys. Rev. A*, vol. 21, no. 3, pp. 948–958, Mar. 1980.

[120] Y. W. Lee and H. I. Aaronson, "Anisotropy of coherent interphase boundary energy," *Acta Metall.*, vol. 28, no. 4, pp. 539–548, 1980.

[121] Z. Hou, P. Hedström, Q. Chen, Y. Xu, D. Wu, and J. Odqvist, "Quantitative modeling and experimental verification of carbide precipitation in a martensitic Fe-0.16 wt%C-4.0 wt%Cr alloy," *Calphad Comput. Coupling Phase Diagrams Thermochem.*, vol. 53, pp. 39–48, 2016.

[122] R. Becker, "Die Keimbildung bei der Ausscheidung in metallischen Mischkristallen," *Ann. Phys.*, vol. 424, no. 1–2, pp. 128–140, 1938.

[123] O. Prat, J. Garcia, D. Rojas, C. Carrasco, and A. R. Kaysser-Pyzalla, "Investigations on coarsening of MX and M23C6 precipitates in 12% Cr creep resistant steels assisted by computational thermodynamics," *Mater. Sci. Eng. A*, vol. 527, no. 21–22, pp. 5976–5983, 2010.

[124] W. Xu, D. San Martin, P. E. J. Rivera Díaz del Castillo, and S. van der Zwaag, "Modelling and characterization of chi-phase grain boundary precipitation during aging of Fe-Cr-Ni-Mo stainless steel," *Mater. Sci. Eng. A*, vol. 467, no. 1–2, pp. 24–32, 2007.

[125] K. Frisk, "Solubility of N in Cr-Fe-Mo-Ni alloys," *Metall. Trans. A*, vol. 23, no. 4, pp. 1271–1278, 1992.

[126] C. C. Qui, "Thermodynamic analysis and evaluation of the Fe-Cr-Mn-N system," *Metall. Trans. A*, vol. 24, pp. 2393–2409, 1993.

[127] D. Kashchiev, *Nucleation Basic Theory With Applications*, Butterworth Heinemann, Oxford, 2000.

[128] J. Feder, K. C. Russell, J. Lothe, and G. M. Pound, "Homogeneous nucleation and growth of droplets in vapours," *Adv. Phys.*, vol. 15, no. 57, pp. 111–178, Jan. 1966.

[129] Y. F. Yin and R. G. Faulkner, "Model predictions of grain boundary chromium depletion in Inconel 690," *Corros. Sci.*, vol. 49, no. 5, pp. 2177–2197, 2007.

Original publications

I Kolli, S., Ohligschläger, T., & Porter, D. (2017). Continuous cooling sensitization and its evaluation in austenitic stainless steels EN 1.4310. In *Proceedings of 9th European Stainless Steel Conference - Science & Market and the 5th European Duplex Stainless Steel Conference & Exhibition.* Bergamo, Italy: Associazione Italiana di Metallurgia.

II Kolli, S., Ohligschläger, T., & Porter, D. (2019). Quantitative prediction of sensitization in austenitic stainless steel accounting for multicomponent thermodynamic and mass balance effects. *ISIJ International,* 59*(*7), 1330-1336.

III Kolli, S., Ohligschläger, T., Kömi, J., & Porter, D. (2019). Sensitization and self-healing in austenitic stainless steel: Quantitative prediction considering carbide nucleation and growth. *ISIJ International, 59(11),* 2090-2097.

IV Kolli, S., Javaheri, V., Kömi, J., & Porter, D. (2019). On the role of grain size and carbon content on the sensitization and desensitization behavior of 301 austenitic stainless steel. *Metals, 9*(11), 1193.

V Kolli, S., Javaheri, V., Ohligschläger, T., Kömi, J., & Porter, D. (2020). The importance of steel chemistry and thermal history on the sensitization behavior in austenitic stainless steels: Experimental and modeling assessment. *Materials Today Communications*, *24*, 101088.

Reprinted with permissions from Associazione Italiana di Metallurgia (Paper I), ISIJ (Papers II and III), and under CC BY (Paper IV) and CC BY-NC-ND (Paper V) license from Authors.

Original publications are not included in the electronic version of the dissertation.

738. Wijewardhana, Uditha (2020) Sparse recovery algorithms for streaming and multidimensional signals

739. Li, Panpan (2020) Deep eutectic solvents in the production of wood-based nanomaterials

740. Nuortimo, Kalle (2020) Public acceptance in energy technology development and deployment : opinion mining case study

741. Juuti, Timo (2020) The precipitation of Laves phase and its contribution to mechanical properties in novel high-Cr ferritic stainless steels

742. Myllymäki, Pekka (2020) Chemical precipitation in the simultaneous removal of NH_4−N and PO_4−P from wastewaters using industrial waste materials

743. Alcaraz López, Onel Luis (2020) Resource allocation for machine-type communication : from massive connectivity to ultra-reliable low-latency

744. Frondelius, Tero (2020) Development of methods in engine design process

746. Särestöniemi, Mariella (2020) UWB in-body propagation and radio channel characteristics for wireless body area network applications

747. Ashraf, Faisal Bin (2020) River regimes and energy demand interactions in Nordic rivers

748. Kuula, Seppo (2020) Continuous co-creation of knowledge-intensive business services

749. Mustonen, Erno (2020) Vertical productisation over product lifecycle : co-marketing through a joint commercial product portfolio

750. Halttula, Heikki (2020) Enhancing data utilisation in the construction project lifecycle through early involvement and integration

751. Nguyen, Hoang (2020) Ettringite-based binder from ladle slag : from hydration to its fiber-reinforced composites

752. Jahromi, Sahba S. (2020) Single photon avalanche detector devices and circuits for miniaturized 3D imagers

753. Xu, Yingyue (2020) Computational modeling for visual attention analysis

754. Saarela, Martti (2020) Growth management of eHealth service start-ups

Book orders:
Virtual book store
http://verkkokauppa.juvenesprint.fi

UNIVERSITY OF OULU P.O. Box 8000 FI-90014 UNIVERSITY OF OULU FINLAND

ACTA UNIVERSITATIS OULUENSIS

SERIES EDITORS

A
SCIENTIAE RERUM NATURALIUM
University Lecturer Tuomo Glumoff

B
HUMANIORA
University Lecturer Santeri Palviainen

C
TECHNICA
Postdoctoral researcher Jani Peräntie

D
MEDICA
University Lecturer Anne Tuomisto

E
SCIENTIAE RERUM SOCIALIUM
University Lecturer Veli-Matti Ulvinen

F
SCRIPTA ACADEMICA
Planning Director Pertti Tikkanen

G
OECONOMICA
Professor Jari Juga

H
ARCHITECTONICA
University Lecturer Anu Soikkeli

EDITOR IN CHIEF
University Lecturer Santeri Palviainen

PUBLICATIONS EDITOR
Publications Editor Kirsti Nurkkala

ISBN 978-952-62-2660-6 (Paperback)
ISBN 978-952-62-2661-3 (PDF)
ISSN 0355-3213 (Print)
ISSN 1796-2226 (Online)

UNIVERSITY OF OULU